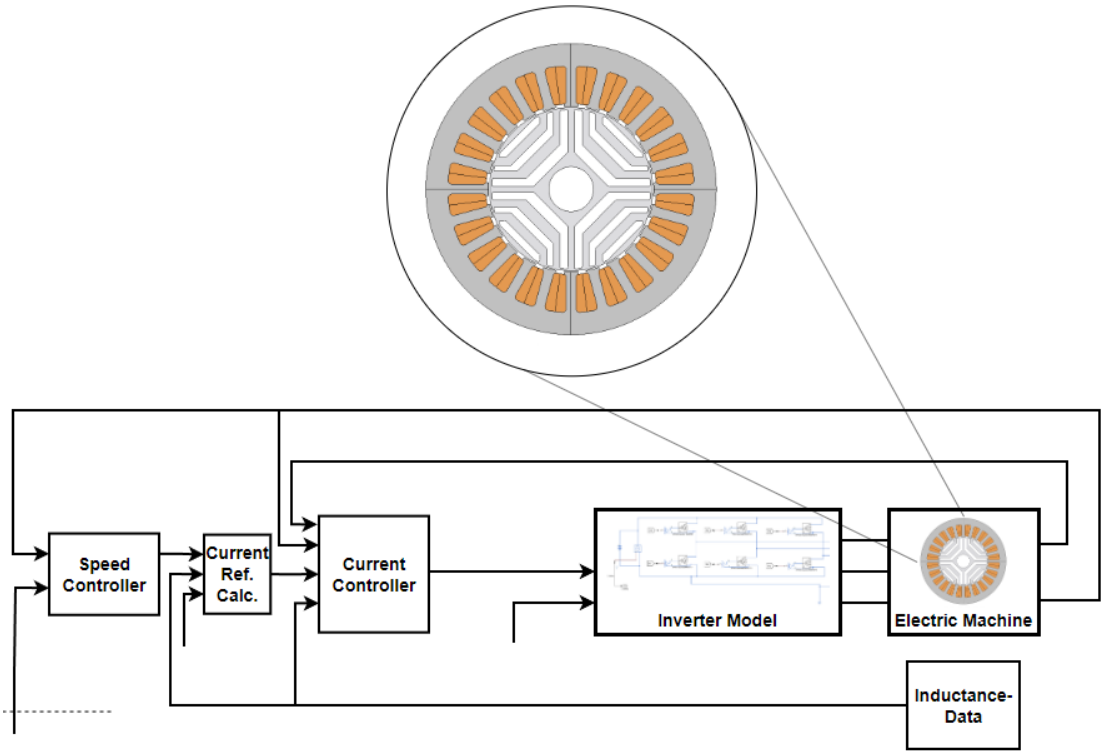

Synchronous Reluctance Motor and Drive System Design for Handheld Applications

A design work utilizing Co-simulations

Master's thesis in Electric Power Engineering

Axel Gunnarson
Ludvig Johansson

DEPARTMENT OF ELECTRICAL ENGINEERING
CHALMERS UNIVERSITY OF TECHNOLOGY
Gothenburg, Sweden 2022
www.chalmers.se

Master's thesis 2022

Design of Synchronous Reluctance Motor and Drive System for Handheld Applications

A design work utilizing Co-simulations

Axel Gunnarson, Ludvig Johansson

CHALMERS
UNIVERSITY OF TECHNOLOGY

Department of Electrical Engineering
Division of Electric Power Engineering
Chalmers University of Technology
Gothenburg, Sweden 2022

Design of Synchronous Reluctance Motor and Drive System for Handheld Applications
A design work utilizing Co-simulations
Axel Gunnarson, Ludvig Johansson

Supervisor: Tobias Stalfors, Husqvarna AB
Examiner: prof. Torbjörn Thiringer, Department of Electrical Engineering, Chalmers

Master's Thesis 2022
Department of Electrical Engineering
Division of Electric Power Engineering
Chalmers University of Technology
SE-412 96 Gothenburg
Telephone +46 31 772 1000

Cover: An illustration of a motor drive system with a synchronous reluctance motor in focus.

Typeset in LaTeX
Printed by Chalmers Reproservice
Gothenburg, Sweden 2022

Design of Synchronous Reluctance Motor and Drive System for Handheld Applications
A design work utilizing Co-simulations
Axel Gunnarson, Ludvig Johansson
Department of Electrical Engineering
Division of Electric Power Engineering
Chalmers University of Technology

Abstract

Today the Permanent Magnet Synchronous Machine (PMSM) is widely used for high performance applications and for different handheld products. The use of rare earth metals in the machines permanent magnets, such as in the NdFeB, do however introduce drawbacks. The magnets are expensive and have a big environmental impact, they also give health issues to the workers. Due to these problems, it is of interest to look into machines that are free from rare earth magnets, such as Synchronous Reluctance Motors (SynRM).

In this thesis work, a SynRM is designed along with a connected drive system with the goal to achieve the same mechanical performance as a PMSM used in handheld applications today. The performance increase by adding ferrite magnets to the rotor structure in the SynRM is also studied. The motors are compared in performance, size, cost, and efficiency. The efficiency is analyzed both for the motor and the drive systems inverter.

The final SynRM design achieves the same mechanical performance as the reference PMSM with a reduction in manufacturing costs of 56%. However, the motor is 65% heavier and 52% longer than the PMSM motor. The lower power factor of the SynRM result in that a higher voltage and more current is needed to achieve the same mechanical performance. The power factor and power density is improved with the addition of ferrite magnets in the rotor. The losses are also higher in both the SynRM and in the inverter that drives it. To achieve a good control of the motor, estimated inductance values are used to frequently update the motor control based on the operating point of the SynRM.

Keywords: Synchronous Reluctance Motor, Handheld Application, Drive System, Voltage Source Inverter, Performance Comparison, Cost Comparison, Mechanical Strength, Power Factor.

Acknowledgements

We would like to express our gratitude to our examiner Prof. Torbjörn Thiringer for his feedback and support throughout the project. Our supervisors at Husqvarna AB, Tobias Stalfors and Cristofaro Pompermaier have been actively involved and shown a great interest in what we are doing and for this, we are very grateful. Thanks should also go out to Edvin Alfredsson a friend and an employee at Husqvarna AB who has been a great support throughout the project.

Axel Gunnarson, Ludvig Johansson, Gothenburg, June 2022

List of Acronyms

Below is the list of acronyms that have been used throughout this thesis listed in alphabetical order:

ALA	Axially laminated anisotropic
dq	Direct-Quadrature
IM	Induction Machine
IPF	Internal Power Factor
IPM	Internal Permanent Magnet
IMC	Internal Model Control
MMF	Motor Magnetic Force
MTPA	Maximum Torque Per Ampere
PF	Power Factor
PM	Permanent Magnet
PMaSynRM	Permanent Magnet assisted Synchronous Reluctance Machine
PMSM	Permanent Magnet Synchronous Machine
PWM	Pulse Width Modulation
RMS	Root Mean Square
SynRM	Synchronous Reluctance Machine
THD	Total Harmonic Distortion
TLA	Transversally Anistropic Laminated

Nomenclature

Φ	Magnetic flux
δ	Load angle
N	Number of turns
L	Inductance
R	Reluctance
R_d	Reluctance in d-axis
R_q	Reluctance in q-axis
L_d	Inductance in d-axis
L_q	Inductance in q-axis
N_d	Number of equivalent turns in the d-axis
N_q	Number of equivalent turns in the q-axis
n_p	Polepairs
$N_{parallel}$	Number of parallel branches
k_w	Windning factor
q	Number of slots per pole per phase
r	Number of layers
R_s	Phase stator resistance
R_c	Equivalent core resistance for a given load
V_s	Applied stator voltage
I_s	Stator current
V_e	Stator electromotive voltage
Ψ	Vector Flux linkage
U_d	Voltage in the d-axis
U_q	Voltage in the q-axis
i_d	Current in the d-axis
i_q	Current in the q-axis
ψ_d	Flux linkage in the d-axis

ψ_q	Flux linkage in the q-axis
ω_r	Rotor electrical angular velocity
T_e	Electromagnetic torque
T_L	Load torque
T_{ext}	External mechanical load at the shaft
T_{fric}	Torque due to friction
J	Inertia constant
D	Friction coefficient
Ω_r	Mechanical rotational velocity
ξ	Saliency ratio
β_c	Current angle
β	Torque angle
φ_i	Internal phase angle
φ	Phase angle
P_e	Active electric power
S	Apparent electric power
I_{mag}	Current magnitude

B_r	Remanence
H_c	Coercitivity
B	Flux density
H	Magntetizing field
μ_0	Permeability constant
ψ_{pm}	Magnetic flux linkage
$P_{winding}$	Winding losses
I_{rms}	Phase current in RMS
p_{fe}	Iron losses per kilogram
k_h	Hysteresis loss coefficient
k_e	Excess loss coefficient
B_m	Magnetic flux density magnitude
σ_{cond}	Conductivity of core material
f	Frequency
d	Lamination thickness

R_a	Active damping, current controller
K_{pcx}	Proportional gain, current controller
K_{icx}	Integral gain, current controller
α_c	Current control system bandwidth
$\hat{L}_x$	Estimated inductance value for current controller
$\hat{R}_x$	Estimated stator resistance value for current controller
ff	Feed forward term
D_a	Active damping, speed controller
$K_{p\omega}$	Proportional gain, speed controller
$K_{i\omega}$	Integral gain, speed controller
α_ω	Speed control system bandwidth
$\hat{J}$	Estimated inertia value for speed controller
$\hat{D}$	Estimated friction coefficient value for speed controller

s_a, s_b, s_c	Switching states
u_a, u_b, u_c	Phase voltage
s_x^+	Positive switching state
s_x^-	Negative switching state
U_{batt}	Battery voltage
U_{tri}	Triangel wave voltage
f_{PWM}	PWM frequency
f_{tri}	Triangle wave frequency
d_a, d_b, d_c	Duty cycles
$U_{x,ref}$	Reference voltage, phase x
m_a	Amplitude modulation ratio
i_s	Phase current

$P_{l,inv}$	Power losses in the inverter
P_{con}	Conduction losses in the inverter
P_{sw}	Switching losses in the inverter

R_{DSon}	MOSFET resistance when fully conducting
I_{Drms}	Averaged operating source -drain current
U_{GS}	Gate source voltage
U_{DS}	Drain source voltage
U_{DD}	Supply voltage
I_{Don}	Drain current
f_{sw}	Switching frequency
E_{on}	Total energy loss during turn on
E_{off}	Total energy loss during turn off

h	Number of flux barriers
n_r	Number of rotor slots per pole
n_s	Number of stator slots per pole
θ_i	Position angle of each barrier
α_m	Rotor slot pitch angle
β_s	Rotor slot displacement angle
K_{wd}	Insulation ratio along the d-axis
K_{wq}	Insulation ratio along the q-axis
$W_{d,i}$	Width of flux barriers in the d-axis
$W_{q,i}$	Width of flux barriers in the q-axis
$S_{q,i}$	Width of flux paths in the q-axis
A	Center point of circular flux barriers
R_{rotor}	Rotor radius
R_{shaft}	Shaft radius
$f_{d,i}$	Average MMF d-axis
$f_{q,i}$	Average MMF q-axis
F_c	Centripetal force
T_b	Braking torque
r	Radius
m	Mass
a_Ω	Angular acceleration
$w_{t,i}$	Tangential ribs
$w_{r,i}$	Radial ribs

σ	Stress
σ_v	Von Mises stress
σ_y	Yield strength
sf	Safety factor
$I_{max,peak}$	Maximum peak current
$I_{max,rms}$	Maximum RMS current
V_{dc}	DC-link voltage
ω_n	Base speed
ω_{max}	Max speed
Q	Stator slots
y	Coil pitch
θ	Electrical rotor position
Θ	Mechanical rotor position
U_{lim}	Limited voltage
e	Regulator error
H	Anti windup gain
$U_{x,ref}$	Reference phase voltage
z_0	Zero sequence shift
R_{load}	RL circuit equivalent resistance
L_{load}	RL circuit equivalent inductance
P_{batt}	Power from the battery
P_{inv}	Power from the inverter
$P_{l,inv,sim}$	Simulated power loss in the inverter
$\eta_{inv,sim}$	Simulated efficiency of an inverter

Contents

1
Introduction

Today's increase of electrified products urges an increase in production volumes for electric machines. This change highlights the importance of an optimized machine design. In general, an optimized design can entail improved machine performance, lower costs in production, and a decrease in the environmental impact. More specifically, the commonly used Permanent Magnet Synchronous Machine (PMSM) use permanent magnets in the rotor as a part of creating the torque. Those magnets constitute a majority of the machine's part of the environmental impact. The magnets also entail further costs and supply risks to the motor manufacturing [1]. This calls for alternative machine designs, using less or no permanent magnets in the rotor. Such an alternative, having no rotor magnets, could be a Synchronous Reluctance Machine (SynRM). The SynRM will be in focus for this master thesis. The motor design also connects to the design of the electric drive system, here meaning the design of the inverter and the motor control.

1.1 Background

Husqvarna AB develops and sells different handheld, gardening, and foresting machines. Such machines are currently driven by a combustion engine. But there is today an increased interest in electrifying those machines. The development requires further research and design of electric machines, and different motor designs need to be reviewed.

The permanent magnets in a PMSM are typically NdFeB magnets due to their high magnetic performance. Besides the light rare earth metal neodymium, a fraction of the heavy earth metal dysprosium is added for the alloy to withstand higher temperatures. In some applications, SmCo magnets are used due to their higher stability at higher temperatures [2]. The extraction methods for rare earth metals often have a big environmental impact. This issue follows the entire process from the extraction to the complete product of a permanent magnet. Ore minerals containing rare earth metals are typically found on all continents and the global resources are known to be relatively large, at $1.2 \cdot 10^8$ metric ton. Compared to copper with known reserves of $8.3 \cdot 10^8$ metric ton [1]. The rare earth metals are however historically indicated as rare due to the difficulties in extracting the metals from the minerals [3]. The industry of rare earth metals leads to various pollution and it is also reported as toxic, giving health issues to the workers [4].

Even though rare earth metals are widespread globally, 80% of the rare earth metals are mined in China [2]. China also possesses a majority of the industry and supply chain to produce permanent magnets [3]. One reason behind the dominance of production in

China is the differences in standards and regulations of environmental and social aspects compared to other nations, and compared to what existed in nations that previously had a bigger role in the mining of rare earth metals [3].

Effects are emerging from the fact that the production of permanent magnets is bound to a single country. It affects the market and can lead to potential shortages [3]. Different approaches are suggested to avoid such market issues. One suggested area is research and development in motor technologies. The importance of such development is addressed by e.q the automotive industry and by the market of wind turbines [5], [6]. Further development of the SynRM would contribute to the suggested research area. Furthermore, replacing PMSMs with a SynRM would completely avoid all issues connected to the rare earth metals and the permanent magnets made from these. Which motivates the design and development of a SynRM and the use of SynRMs in handheld applications.

1.2 Purpose

The overall purpose is to evaluate the potential of using a SynRM for driving Husqvarna handheld machines. This assessment should create a basis of performance data that are relevant for the application. The evaluation will also embody the actual design of a SynRM and inverter circuit, with a related control system connected. The design work should be based on models where relevant features are parameterized. The drive system should then be simulated with dynamic models to analyze the complete system performance. The purpose is also to compare the SynRM with a PMSM. During the project, a cost analysis will be performed based on the SynRM design compared to an already existing PMSM at Husqvarna. This is done to support a bigger purpose and to do a more general evaluation of the SynRM. For the same reason, the project will also reflect on the environmental and ethical aspects of using SynRM instead of a PMSM.

1.3 Scope

In this project, no physical implementation of a motor design or drive system will be made. The time will not be there to design a motor system and to later build it. Another aspect of the motor and the drive design that will not be considered is a thermal analysis. A cooling system will also not be developed. However, some aspects of thermal analysis will be taken into account to design a motor that can be realistically cooled. This includes accounting for the current density in the winding design and fill factor so as to not create a machine that cannot be realistically cooled. Similar applies to the inverter design where the power dissipated will be analyzed to not damage the selected components. The drive system design will involve the implementation of an inverter design where switching components can be validated. Since the purpose is to evaluate the drive system performance, only the vital components of the low voltage system will be considered.

1.4 Social, environmental and ethical aspects

An important aspect of developing a new product is to evaluate the ethics around the product itself and the process of how the product is developed and manufactured. The ideal case is to make a product that is profitable and solves a problem, while still being ethically sound. A goal of this project is as mentioned previously, to evaluate a solution to the ethical problems with rare earth magnets. The social, environmental and ethical aspects will be discussed from three key aspects. Aspects that are part of the reason why the project is of interest, problems related to the work process and what effects the result of the project could have.

1.4.1 Reasons for the project

Increased know-how is a key part of addressing several social, environmental, and ethical issues. This project aims to gain know-how in a technical solution that avoids permanent magnets and thus relieves the problematic extraction and market issues of permanent magnets. Consequently, it reduces the impacts of such extraction and production.

1.4.2 During the work

Since no physical models will be made and the project is done completely in simulation software there will not be any relevant ethical aspects or sustainability problems during the work process itself.

1.4.3 Aspects of the results

If a SynRM could replace a PMSM it would reduce the environmental and social issues related to permanent magnets as was discussed previously. This is one of the most important reasons for designing electrical machines without rare earth magnets. Another reason why PMSMs are widely used is because of their high energy efficiency [7]. From an environmental aspect, this is important since far from all electricity production is from renewable or low carbon emission sources. In the European Union alone, which is one of the world's largest electricity producers, only 54.4% of electricity produced in 2019 came from renewables or nuclear power [8]. The combustion sources produce greenhouse gases which are not ecologically sustainable. With the results in hand, it is therefore interesting to compare the efficiency with existing PMSMs. If the efficiency is significantly lower, the absence of magnets must be weighed against the loss in efficiency.

2
Theory

In this chapter relevant theory to understand the work and the result will be presented. The concept of torque production due to reluctance difference is explained along with the governing equations for a SynRM and a PMaSynRM. The theory behind controlling a SynRM is also presented.

2.1 Basic reluctance concept

A magnetically conductive material always wants to align with a magnetic field so that the total reluctance is minimized. This is why a compass always points towards magnetic north. The path of least reluctance is here defined as the d-axis, and consequently, this axis wants to align with the magnetic field. The q-axis is instead defined as the direction of most reluctance and the ideal alignment is orthogonal to the flux path to achieve the least reluctance [9].

The two objects in figure 2.1 are both in steel. This steel has a much lower reluctance than the surrounding air. Since object 1 is symmetric, the magnetic flux lines, represented by Φ experience the same reluctance in all directions. The rectangular shape of object 2 results in more steel in one direction, naturally, labeled as the d-axis, and less in the other, that is the q-axis. If the object is not aligned with the magnetic field, a torque will be produced to align the d-axis with the field to make the total reluctance as small as possible. The size of this torque depends on the load angle δ, with more torque for a higher angle. It is this phenomenon that is utilized to produce torque and rotation in a SynRM.

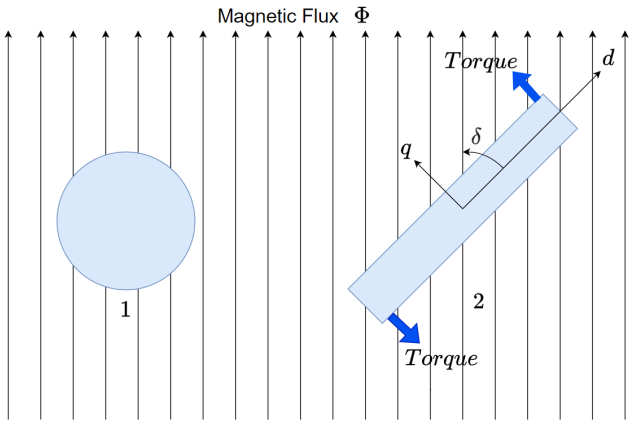

Figure 2.1: Basic reluctance concept

In the SynRM the stator windings produce the magnetic field. The AC 3-phase currents create a sinusoidal field that rotates with a synchronous speed ω_r. The rotor rotates to always align the path of least reluctance (d-axis) with the field. Whenever the $\delta \neq 0$ a torque is produced by the machine. The torque leads to electrical energy being converted into mechanical energy [9].

2.2 Reluctance and inductance

When designing a SynRM the reluctance is maximized in q-axis and minimized in d-axis. The relation between inductance and reluctance is described in the equation

$$L = \frac{N^2}{R} \tag{2.1}$$

where L is inductance, N is the number of turns and R is the reluctance. To produce torque in a SynRM there must be a difference in the inductance in d-axis (L_d) and the inductance in the q-axis (L_q). L_d and L_q are changed by changing the amount of reluctance in d- and q-axis respectively. This is the core principle of the rotor design for a SynRM. L_d and L_q can be calculated with the relations,

$$L_d = \frac{N_d^2}{R_d} \cdot \frac{n_p}{N_{parallel}} \tag{2.2}$$

$$L_q = \frac{N_q^2}{R_q} \cdot \frac{n_p}{N_{parallel}} \tag{2.3}$$

where N_d and N_q are the equivalent number of turns in the d- and q axis, R_d and R_q are the reluctances in the d and q axis, n_p is the number of pole pairs and $N_{parallel}$ is the number of parallel branches in the stator windings. N_d and N_q can be calculated as,

$$N_d = N_q = N_{turn} k_w q r \tag{2.4}$$

where N_{turn} is the number of turns per coil, q is the number of slots per pole per phase, k_w is the winding factor and r is the number of layers. The reluctance can be modeled using mathematical expression, this is however quite inaccurate and a FEM program should be used. Also, the reluctance in both axes is dependent on the level of saturation in the magnetic circuit.

2.3 Electrical and mechanical equations

Here the electrical equations of the SynRM will be presented along with the governing equations relation to the IPF and the performance of a SynRM motor. The relation between the load torque and electrical torque is also presented.

2.3.1 SynRM motor circuit

A SynRM can be described in the time-frame, the $\alpha\beta-$frame and in the dq-frame. In the dq-vector space, the electrical circuit is shown in figure 2.2 and the voltage equations becomes

$$V_s = V_e + R_s I_s \tag{2.5}$$

$$V_e = \frac{d\Psi}{dt} + \omega_r \Psi \tag{2.6}$$

where R_s is stator resistance, R_c is the equivalent core resistance for a given load, V_s is the voltage applied to the stator, V_e is the stator electromotive voltage or internal voltage of the stator windings after the voltage drop due to losses. I_s is the stator current, Ψ is the flux linkage and ω_r is the rotor electrical angular velocity.

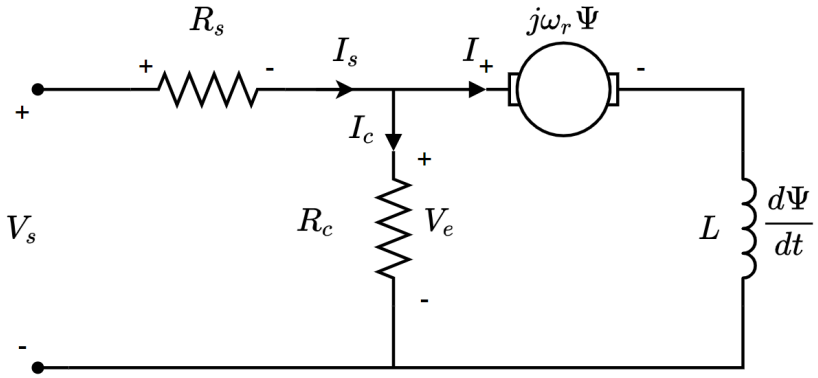

Figure 2.2: dq-vector circuit

When the dq-vector is split into its individual components, namely the d- and q-axis, the governing stator voltage equations becomes,

$$U_d = R_s i_d + \frac{d\psi_d}{dt} - \omega_r \psi_d \tag{2.7}$$

$$U_q = R_s i_q + \frac{d\psi_q}{dt} + \omega_r \psi_q \tag{2.8}$$

where U_d and U_q is the stator voltage in the d- and q-axis respectively, ψ_d and ψ_q is the flux linkage in the d- and q-axis respectively, and i_d and i_q is the current in the d- and q-axis respectively. The voltage equations can be rewritten by using the relationship between inductance and flux linkage,

$$\Psi = LI \tag{2.9}$$

or in the dq-frame,

$$\psi_d = \psi_d(i_d, i_q) = L_d(i_d, i_q) i_d \tag{2.10}$$

$$\psi_q = \psi_q(i_d, i_q) = L_q(i_d, i_q) i_q \tag{2.11}$$

so that U_d and U_q can be calculated as

$$U_d = R_s i_d + L_d \frac{di_d}{dt} - \omega_r L_q i_q \tag{2.12}$$

$$U_q = R_s i_q + L_q \frac{di_q}{dt} + \omega_r L_d i_d \tag{2.13}$$

The resulting dq-circuits can be seen in figure 2.3.

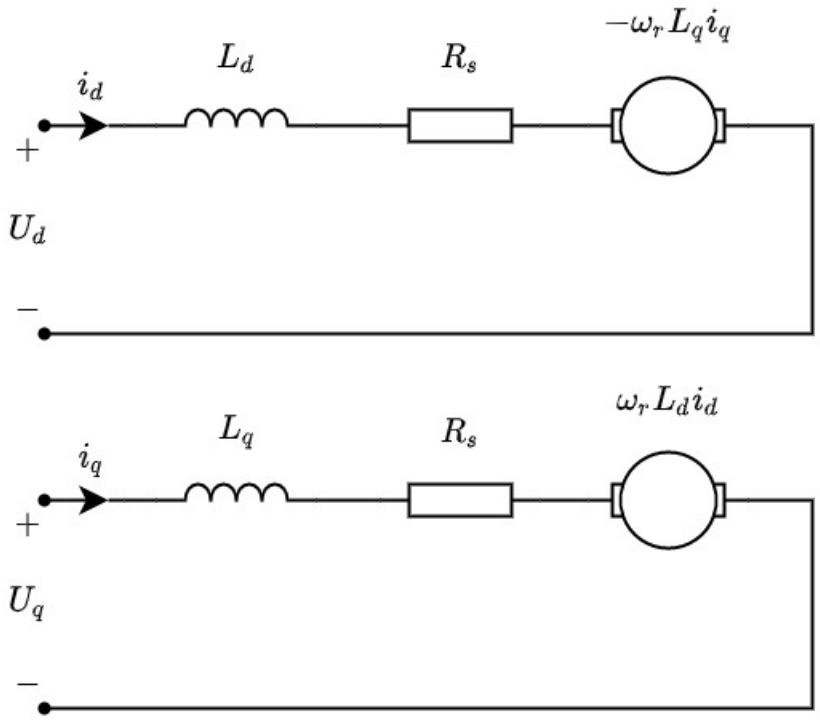

Figure 2.3: SynRM circuit in dq-frame

ψ_d and ψ_q and by relation L_d and L_q are dependent on the operating point as well as cross-coupling effects between the axes. Meaning that the inductances vary with the current level. Cross saturation occurs between the d- and q-axis as well. This is due to that when there is a current in the d-axis this will also induce flux in the q-axis and vice versa. This effect also leads to iron saturation which in turn affects the inductance in the other axis even more [9].

Electromagnetic torque is produced by the product of flux linkage and the current that flows through the coil,

$$T_e = \Psi i \tag{2.14}$$

where T_e is the electromagnetic torque. With the relations in (2.10) and (2.11) the torque for the SynRM is as follows

$$T_e = \frac{3n_p}{2}(L_d - L_q)i_d i_q \tag{2.15}$$

where n_p is the number of pole pairs in the machine. The governing equations for the SynRM consists of two parts. Aside from the electrical part there is also the mechanical part. The relation between the T_e and the load torque T_L can be described as

$$\frac{J}{n_p}\frac{d\omega_r}{dt} = T_e - T_L \tag{2.16}$$

where J is the moment inertia coefficient. T_L can consist of several different torques, but is usually modeled as one part external load (T_{ext}) and one part speed dependent load due to friction (T_{fric}) [10]. The friction load is calculated as

$$T_{fric} = D\Omega_r \tag{2.17}$$

where D is the friction coefficient and Ω_r is the mechanical angular velocity of the SynRM. The definition of T_L is then

$$T_L = T_{ext} + T_{fric} \tag{2.18}$$

2.3.2 Saliency ratio and performance

Saliency ratio (ξ) is commonly used to judge the performance of a SynRM. It is defined as

$$\xi = \frac{L_d}{L_q} \tag{2.19}$$

The saliency becomes important when discussing the internal power factor of a SynRM. In figure 2.4 the phasor diagram of the SynRM can be seen that corresponds to the SynRM circuit shown earlier in figure 2.2.

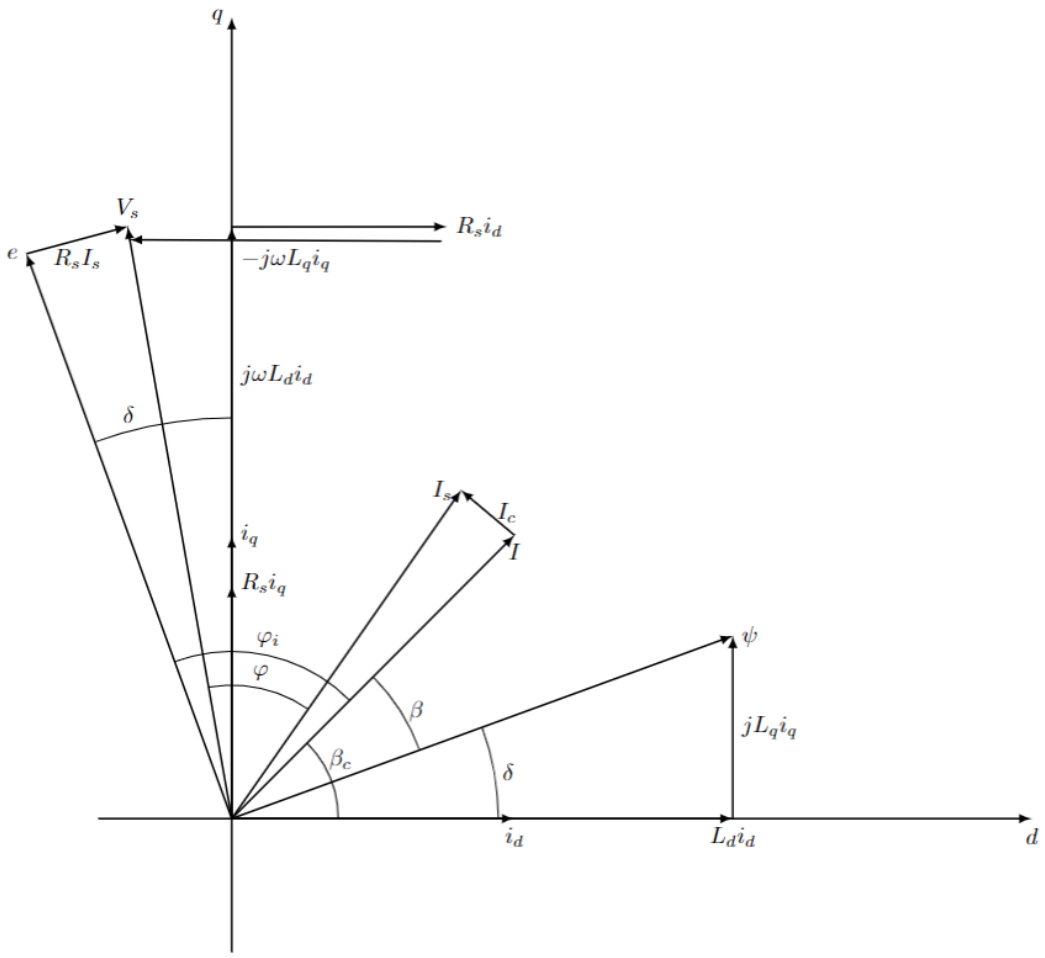

Figure 2.4: Phasor diagram SynRM

For the angles in figure 2.4 the following holds [11]

$$\beta_c = \beta + \delta \tag{2.20}$$

$$\frac{\pi}{2} + \delta = \varphi_i + \beta_c \tag{2.21}$$

where φ_i is the internal phase angle, φ is the phase angle, β_c current angle, δ is the load angle and β the torque angle. From this relation the internal power factor (IPF) of the SynRM can be calculated as

$$IPF = \cos\varphi_i = \cos(\frac{\pi}{2} + \delta - \beta_c) = -\cos\left(\beta_c + \arctan\left(\xi \cot\left(\beta_c\right)\right)\right) \tag{2.22}$$

When studying the phase diagram in figure 2.4 it becomes clear that the IPF and the power factor (PF) are closely related, the PF is calculated as,

$$PF = \cos\varphi = \frac{P_e}{S} \tag{2.23}$$

where P_e is the active electrical power produced in the SynRM and S is the apparent power. A high value for IPF will mean a high value for PF since the difference comes down to the effects of R_s and R_c on the stator voltage of the machine. From (2.22) it is clear that it exists an optimal current angle β_c that yields a maximum IPF. It can be shown that this occurs when $\beta_c = \sqrt{\xi}$ [11] and the IPF becomes

$$IPF = \frac{\xi - 1}{\xi + 1} \tag{2.24}$$

The torque equation (2.15) can be rewritten as

$$T_e = \frac{3n_p}{2}(L_d - L_q)I_{mag}^2 \frac{\sin\left(2\beta_c\right)}{2} \tag{2.25}$$

where I_{mag} is the magnitude of the current and if the internal power factor is plotted against β_c for different values of saliency it is clear when comparing figure 2.5 and the torque equation (2.25) that the maximum torque angle at 45° for the equation does not coincide with the optimal angle for IPF. The operating point of 45° is also known as the maximum torque per ampere (MTPA) operating point. The motor is therefore not operating at ideal IPF when working at maximum torque.

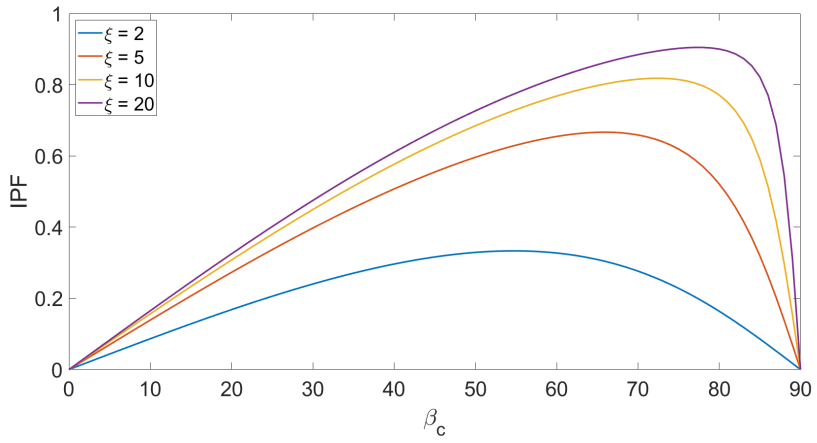

Figure 2.5: IPF vs current angle for given saliency ratios

The torque is determined by the difference in inductance while the IPF is determined by the saliency ratio. However, when looking at (2.10) and (2.11) it is clear that L_d and L_q are dependent on the size of the individual currents i_d and i_q meaning that the maximum torque angle is not necessarily at 45°. Especially the angle can become larger when the steel is saturated and there is cross saturation between the two axes [12]. In this project, the torque is studied at the maximum torque angle determined by using FEM simulations and the PF and torque is calculated at this specific operating point.

2.3.3 Core material

Steel is considered to be a soft magnetic material. Meaning that it has a high permeability. A soft magnetic material is what is used when manufacturing motor cores since it creates paths of low reluctance and low loss. The grade of the steel mainly affects the iron losses of the machine. A higher grade leads to more losses and vice versa. However for steels that are not alloyed with rare earth elements, the losses are quite similar [12]. The steel in the rotor also has another important property to consider which is its yield strength. In a SynRM, the flux barriers are sources of structural instability [13]. But, the addition of structural supports can cause leakage flux paths that will decrease the reluctance difference between the d- and q-axis. So a higher strength steel in the rotor can improve the performance of a SynRM, by the rotor not requiring extra or larger supports that can lead to leakage flux paths.

2.3.4 Magnets

A magnet material is defined by its BH-curve, such as the one in figure 2.6. Magnetic materials that are used for permanent magnets are called hard magnetic materials, meaning that the BH curve around the origo is wide compared to other magnetic materials and are hard to demagnetize. Hard magnetic materials will keep their residual magnetic flux even after an external field has been removed and this is where the name of Permanent Magnet (PM) comes from. This residual magnetic flux is called remanence (B_r). Another defining property of the material is the magnetic materials coercivity (H_c) or coercive force. This describes the external magnetic field intensity needed to bring the magnetization of the material down to zero. The magnetization (M) of the material relates to the flux density as

$$B = \mu_0(H + M) \tag{2.26}$$

where $\mu_0 = 4\pi \cdot 10^{-7}$ is the permeability constant, H is the magnetizing field and B the magnetic flux density.

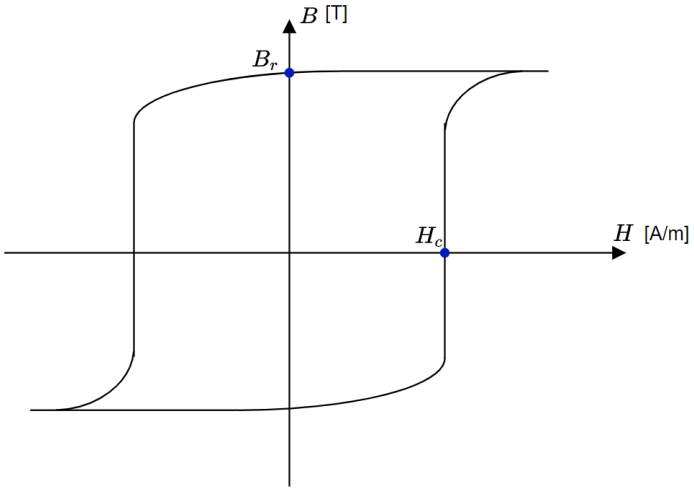

Figure 2.6: Typical BH curve of a permanent magnet material

2.3.5 PMaSynRM motor circuit

To reach a power factor of more then 0.9 for a SynRM the saliency ratio would have to be larger then 20, which is not feasible [11]. The power factor in a SynRM can however be improved by the addition of magnets, thus making a SynRM into a Permanent Magnet assisted Synchronous Reluctance Machine (PMaSynRM). By adding magnets the characteristics of the machine is slightly altered. In a PMaSynRM magnets are placed in the direction of the q-axis flux. This means that the q-axis flux linkage is given an extra component [14]. The d-axis flux linkage equation, (2.10), remains the same, but the q-axis becomes

$$\psi_q = \psi_q(i_d, i_q) = L_q(i_d, i_q)i_q - \psi_{pm} \tag{2.27}$$

where ψ_{pm} is the permanent magnet flux linkage. The magnet essentially counteracts the flux already in the q-axis, making the ψ_q even smaller which leads to a higher torque. The flux from the magnets also help to saturate the steel in the q-axis which in turn leads to a lower value for L_q increasing the torque even further. The stator voltage equations becomes

$$U_d = R_s i_d + L_d \frac{di_d}{dt} - \omega_r L_q i_q + \psi_{pm}\omega_r \tag{2.28}$$

$$U_q = R_s i_q + L_q \frac{di_q}{dt} + \omega_r L_d i_d \tag{2.29}$$

and the circuit diagram changes with an added voltage component from the magnet, shown in figure 2.7.

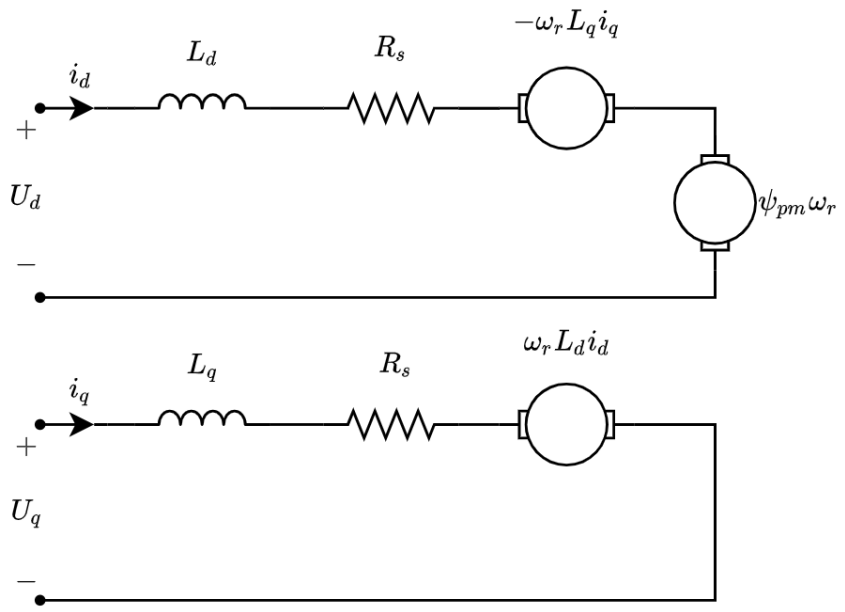

Figure 2.7: PMaSynRM circuit in dq-frame

The resulting torque becomes

$$T_e = \frac{3n_p}{2}(\psi_{pm} i_d + (L_d - L_q) i_d i_q) \tag{2.30}$$

or if written with current magnitude and current angle

$$T_e = \frac{3n_p}{2}(\psi_{pm} I_{mag} \cos\beta_c + (L_d - L_q) I_{mag}^2 \frac{\sin(2\beta_c)}{2}) \tag{2.31}$$

From (2.31) it can be shown that the MTPA angle will still be in the first quadrant($0-90°$), but that the MTPA angle will no longer be 45°. Even before saturation is taken into account the maximum torque angle will slightly decrease. The relation between T_e and T_L is the same for the PMaSynRM as for the SynRM and follows (2.16) and (2.17).

2.4 Motor losses

The losses in any electrical motor consist mainly of two parts. The core losses in the rotor- and stator material, and the losses in the winding due to the resistivity of the conductors in the stator.

2.4.1 Winding losses

Winding losses, also known as copper losses or Joule losses, are the losses caused by the resistance in the windings in the motor stator. When current flows through this resistance a voltage drop occurs. The winding losses can be calculated as,

$$P_{Winding} = 3I_{rms}^2 R_s \tag{2.32}$$

where $P_{Winding}$ is the total joules losses, I_{rms} is the RMS phase current.

2.4.2 Core losses

The core losses in an electric machine consist of several different losses. The two main parts are the hysteresis losses and the eddy current losses. The hysteresis losses are caused by changing polarization in the material due to the change of magnetic field when the field is rotating. Hysteresis losses are affected by the microstructure of the material and its properties. Eddy current losses are the losses caused by the flux alternating in the magnetic material. This induces currents in the lamination known as eddy currents. The thickness of the lamination along with the conductivity of the core material affects the size of these losses. Aside from Hysteresis and Eddy current losses, there are also excess losses that are a collection of all other losses in the core material. Excess losses depend on that their will be nonuniform distribution of the flux density in the lamination. This is caused by nonlinear diffusion of the flux density and skin effect[15]. Hysteresis-, eddy current- and excess losses can be calculated for electric sheet per kilogram as

$$p_{fe} = k_h B_m^2 f + \frac{\pi^2 \sigma_{cond} d^2}{6}(B_m f)^2 + 8.67 k_e (B_m f)^{1.5} \tag{2.33}$$

where p_{fe} is losses per kilogram, k_h is the hysteresis losses coefficient, k_e is the excess loss coefficient, B_m is the magnetic flux density magnitude, σ_{cond} is the conductivity of the core material, d is the thickness of one electrical sheet and f is the frequency. Equation (2.33) is useful to describe what affects the core losses. However, the losses are most easily determined with aid of FEM software since it is difficult to find the exact values analytically.

2.5 Drive system

A drive system for the electric machines consists of a control system, often implemented on a microcontroller, and the voltage source inverter. The principal theory behind the inverter and the control system are explained in this section.

2.5.1 Control theory

To design the control system for the SynRM, the motor circuit described in section 2.3.1 is regarded as two coupled process models in the laplace domain, labeled as $G_d(s)$, $G_q(s)$, for the d-voltage and q-voltage respectively [10],

$$G_d(s) = \frac{1}{R_s + sL_d} \tag{2.34}$$

$$G_q(s) = \frac{1}{R_s + sL_q} \tag{2.35}$$

a current input system for the SynRM then yields the expressions

$$i_d = G_d(s)(U_d + \omega_r L_q i_q) \tag{2.36}$$

$$i_q = G_q(s)(U_q - \omega_r L_d i_d) \tag{2.37}$$

G_x will be used when G_d and G_q are referred to in common. The process $G_x(s)$ is modified to $G'_x(s)$. $G'_x(s)$ utilizes a decoupling term to compensate for the coupled back-emf term, $\omega_r L_x i_x$. $G'_x(s)$ also includes active dampening to reduce the impact of disturbances.

The process is identified to be a first order system and the control design can then be accomplished by a standard internal model control (IMC) setup, shortly described by

$$G_{cl} = \frac{i}{i_{ref}} = \frac{F_c(s)G'_x(s)}{1 + F_c(s)G'_x(s)} = \frac{\alpha_c}{\alpha_c + s} \tag{2.38}$$

where F_c is designed to be a PI controller,

$$F_c(s) = k_p + \frac{k_i}{s} \tag{2.39}$$

and G_{cl} indicates the current control closed loop system. α_c is the control system bandwidth. Designing the current controller then yields,

$$F_c(s) = \frac{\alpha_c}{s} G'^{-1}_x(s) \tag{2.40}$$

Finally, the active dampening R_{ax}, followed by the control parameters k_{pcx} and k_{icx} can be derived as

$$R_{ax} = \alpha_c \hat{L}_x - \hat{R}_s \tag{2.41}$$

$$K_{pcx} = \alpha_c \hat{L}_x \tag{2.42}$$

$$K_{icx} = \alpha_c (\hat{R}_s + R_{ax}) \tag{2.43}$$

The control loop is illustrated in figure 2.8. The decoupling term is described by the feed forward (ff) term.

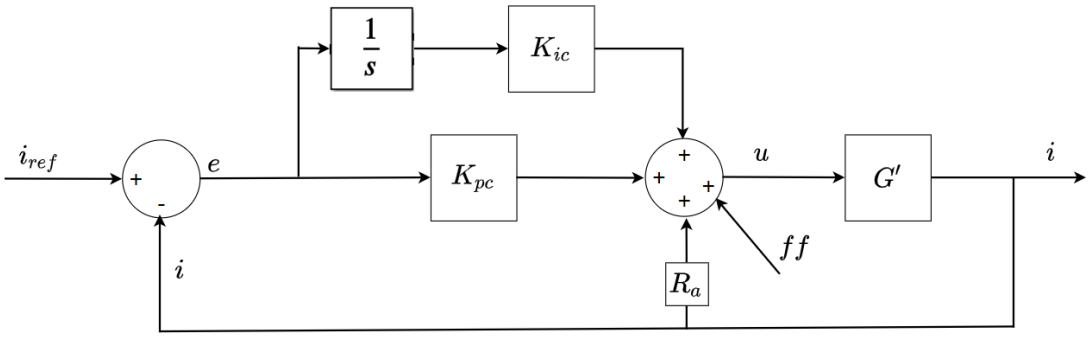

Figure 2.8: Current controller with a PI-regulator

A speed controller for the motor can be implemented in a similar way to the current controller. The controller is also a PI-controller as in equation (2.39). The proportional speed gain ($K_{p\omega}$) and the integral speed gain ($K_{i\omega}$) are determined by the inertia and friction of the motor. The bandwidth of the speed controller (α_ω) should be 10 times less than that of the current controller since the current dynamics should be much faster then that of the speed controller [10]. With this in mind the current controller can be seen as ideal and the gain becomes 1, see figure 2.9. Just as with the current controller active

dampening (D_a) is used to prevent overshoots of the speed. The active damping and the gain coefficients are calculated as

$$D_a = \alpha_\omega \hat{J} + \hat{D} \tag{2.44}$$

$$K_{p\omega} = \alpha_\omega \hat{J} \tag{2.45}$$

$$K_{i\omega} = \alpha_\omega^2 \hat{J} \tag{2.46}$$

The full control loop can be seen in figure 2.9

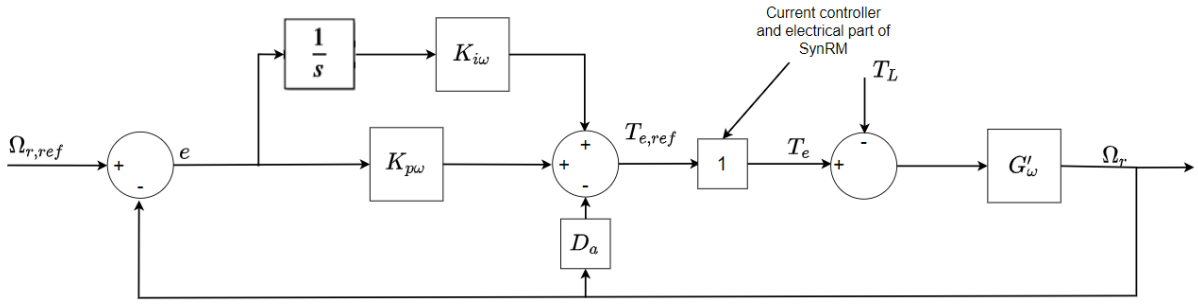

Figure 2.9: Speed control loop

2.5.2 Operation modes

The motor model of the SynRM, described in the d- and q-frame by (2.12) & (2.13) can in combination with the system limits be used to describe the operation areas in terms of torque and speed. Algorithms can be used to maximize the operation towards a higher torque or a higher speed.

In the constant torque operation, a MTPA-algorithm can be used to operate the motor as described in section 2.3.2. The torque is then maximized for all speeds up to the base speed of the motor.

With increasing speeds, the back emf voltage also increases. The speed can only increase up to the point where the back emf voltage is equal to the magnitude of the inverter voltage. At this maximum point, the motor operates at the base speed, ω_n. If a bigger portion of the maximum inverter voltage, U_{max}, is donated to the q-axis voltage, the motor can operate at higher speeds, up to ω_{max}. When going from operation in speeds up to ω_n to ω_{max}, the motor leaves the constant torque operation and field weakening is obtained. One way to illustrate the operation modes is by the voltage ellipse and the current circle, both plotted in the current plane, see figure 2.10.

More specifically, the system limits are described by the maximum current $I_{max,peak}$ and the maximum inverter voltage U_{max}, where

$$I_{max,peak}^2 = i_d^2 + i_q^2 \tag{2.47}$$

$$U_{max}^2 = U_d^2 + U_q^2 \tag{2.48}$$

Then using (2.12) & (2.13), at steady state the derivate terms are zero and since the resistive drops are small compared to the back EMF the stator resistances are also neglected [16]. The voltage limit can be written as

$$U_{max}^2 = (\omega_r L_d i_d)^2 + (\omega_r L_q i_q)^2 \tag{2.49}$$

To describe the voltage ellipse, (2.49) is derived to form

$$\frac{i_d^2}{a^2} + \frac{i_q^2}{b^2} = 1 \tag{2.50}$$

where

$$a = \frac{U_{max}}{\omega_r L_d} \tag{2.51}$$

$$b = \frac{U_{max}}{\omega_r L_q} \tag{2.52}$$

What then happens with increasing ω_r is that the voltage ellipse shrinks. The blue dotted line in fig 2.10 represents the motor voltage at ω_n and the black dotted line represents the motor voltage at ω_{max}. The red circle represents the maximum allowable current.

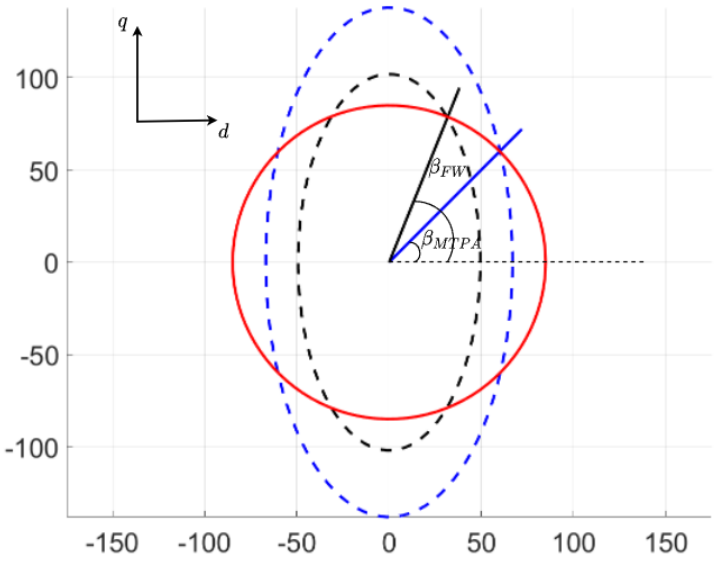

Figure 2.10: Operation modes for the SynRM, illustrating the current circle and the two voltage ellipses at different electrical speeds

The motor will operate at a point where the voltage intersects with the current. When the blue dotted line intersects with the maximum current the motor operates at ω_n and maximum torque. When the speed increases the point of intersection will have to be shifted to a point at a bigger β_c-angle. This is then the operation in field weakening and the generalized angle for this operation is β_{FW}. Using (2.49) in combination with trigonometric identities, β_{FW} can be calculated as

$$\beta_{FW} = acos\sqrt{\frac{U_{max}^2 - \omega_r^2 L_q^2 I^2}{\omega_r^2 I(L_d^2 - L_q^2)}} \tag{2.53}$$

2.5.3 Inverter model

By the principles of a half-bridge converter, a variable sinusoidal voltage can be constructed from a DC voltage . Combining three such converter legs realizes the topology of the commonly used three-phase voltage source inverter for drive applications [17]. As desired for a drive application, the output voltage is adjustable in frequency and magnitude, which is realized by a switching scheme and the switching states s_a, s_b, s_c, driving the six switching devices. The topology is illustrated in figure 2.11, where the three output phase voltages are labeled u_a, u_b and u_c and the constant input DC voltage is represented by a battery voltage, U_{batt}.

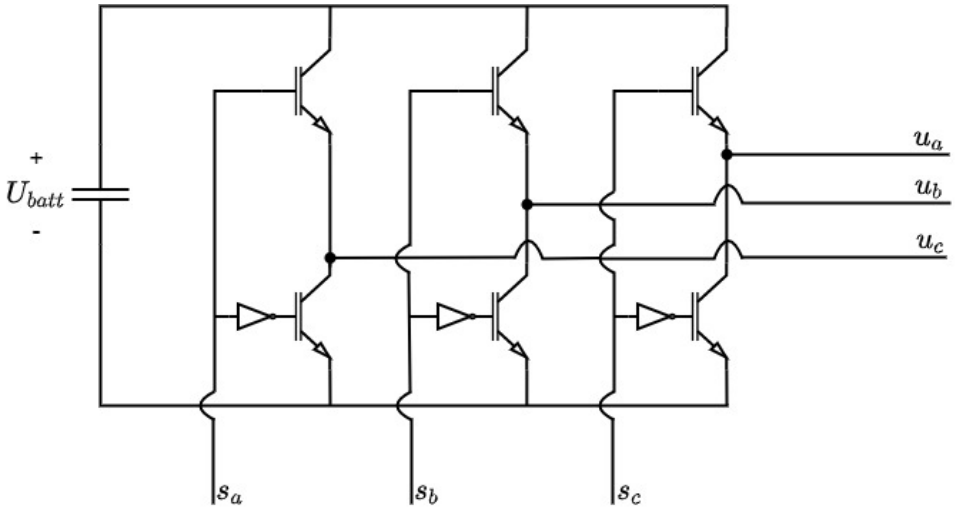

Figure 2.11: The topology of a three phase inverter

The six switching devices are in figure 2.11 illustrated by n-type MOSFETs. But also other types of transistors can be used in a hardware implementation. The lower switches have an inverter gate (NOT-gate) at their gate port to illustrate that the switching state is at this point inverted compared to at the gate at the top switches. Thus, the definitions of the states can be expanded to s_x^+ and s_x^- for the positive and negative (inverted) signal respectively.

The output voltage is sinusoidal in the sense that the output value approximates a sinusoidal voltage. A time-instant value will be $\pm U_{batt}/2$, controlled by a pulse width modulation (PWM) signal. The PWM frequency, f_{PWM} is governed by a triangle wave defined by a amplitude U_{tri} and a frequency f_{tri}, where $f_{PWM} = f_{tri}$. The amplitude of the approximated phase voltage u_x is governed by the duty cycle, d_x. Where d_x is defined by a reference voltage $U_{x,ref}$ calculated by the relation,

$$d_x = \frac{U_{x,ref}}{U_{batt}} + 0.5 \tag{2.54}$$

The duty cycle is then compared with the triangle wave to set the pulse width of the switching states, this is illustrated in fig 2.12. A useful definition when discussing the

switching scheme is the amplitude modulation ratio, m_a, defined as

$$m_a = \frac{U_{x,ref}}{U_{tri}} \tag{2.55}$$

The phase voltage from the inverter with a inductive load form an sinusoidal phase current i_s, with a frequency f. The current is typically not a pure sinusoidal signal. The signal will typically be distorted and in addition to the fundamental component i_{s1} (with $f_1 = f$) it will also contain harmonic components i_{sn} with the n order of harmonic frequencies, f_n, where $f_n = nf_1$. The total amount of distortion of a current or a voltage can be quantified by the total harmonic distortion (THD). For the current it is defined as [17]

$$\%THD_i = 100\sqrt{\sum_{n\neq 1}\left(\frac{i_{sn}}{i_{s1}}\right)^2} \tag{2.56}$$

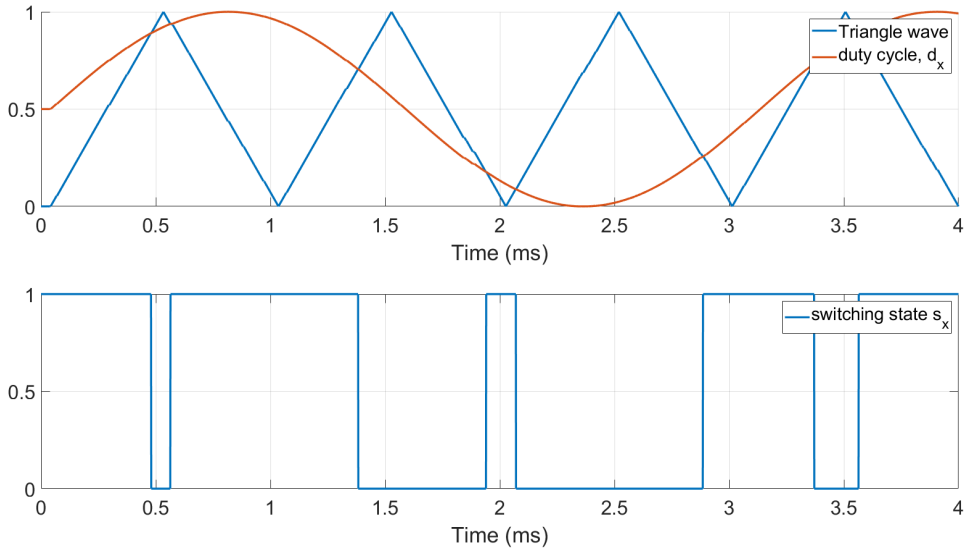

Figure 2.12: Illustration of the triangle wave comparison.

2.5.4 Inverter losses and blanking time

The drive system entails power losses and thus heat being dissipated. The MOSFET switching is of certain interest in this context. Starting with the power losses in the inverter, $P_{l,inv}$, it can typically be modeled by two components, the conduction losses, P_{con} and switching losses P_{sw}, thus,

$$P_{l,inv} = P_{con} + P_{sw} \tag{2.57}$$

The averaged conduction losses correspond to a typical ohmic loss and can be defined by the resistance when the MOSFET is in the region of fully conducting, R_{DSon}, and the averaged operating source- drain current I_{Drms}, according to,

$$P_{con} = R_{DSon}I_{Drms}^2 \tag{2.58}$$

When modeling the switching losses the switching process is approximated to be linear, this also corresponds to a worst-case calculation, it is well suited for engineering calculations and an inverter application. The process is well explained in literature, for instance in [18], and here briefly reviewed. As the gate- source voltage, U_{GS}, reaches the threshold voltage the drain- source voltage U_{DS} starts to drop and the drain current rises to its final value, I_{Don}, this current is defined by the load in the application and the rising transient occurs under a time instance, t_{ri}. After the reverse recovery of the diode, and the time t_{rr}, the voltage over the MOSFET eventually drops from the supply voltage, $U_{DS} = U_{DD}$, to $U_{DS} = R_{DSon}I_{Don}$. During this phase, occurring during the time t_{fu}, U_{GS} is clamped at a defined plateau value. This for accounting for the gate-drain capacitance. The voltage fall time, t_{fu} is of certain importance when implementing the MOSFET. One applied visualization of this complete switch cycle is illustrated in figure 2.13.

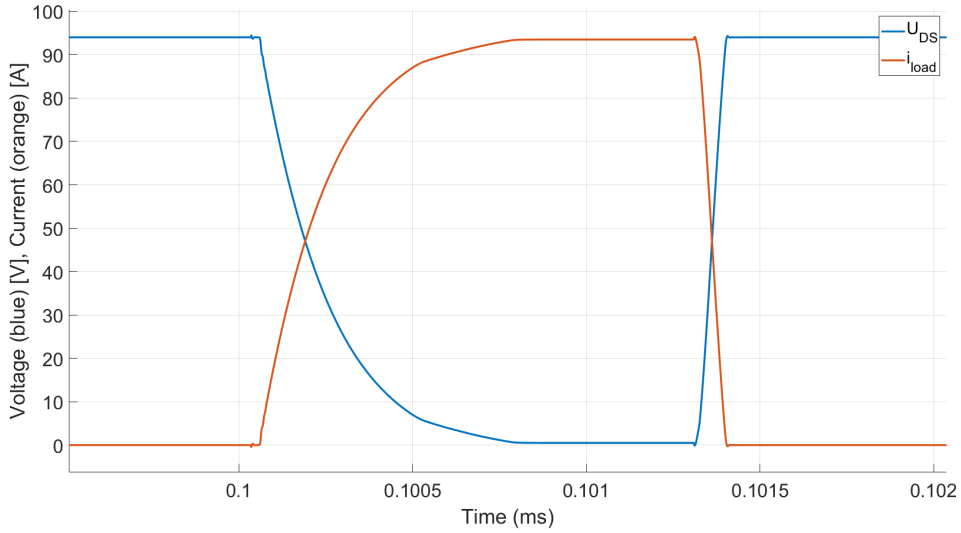

Figure 2.13: The voltage over the MOSFET and the current through the load, plotted over the period of one falling voltage and one rising voltage.

The aforementioned reverse recovery of the diode accounts for the time instance where the minority carriers in the diode are to be dissipated and the charge Q_{rr} needs to be released, this charge is dissipated by the MOSFET and hence yields a loss of power, annotated as E_{onMrr}. The fact that the current through the MOSFET rises before the drain- source voltage drops entails a stored energy, commonly known as the switch-on energy, E_{onM}. The total energy losses during turn on, E_{on}, can then be calculated as,

$$E_{on} = \int_0^{tri+tfu} u_{DS}(t) \cdot i_D(t)dt = E_{onMi} + E_{onMrr} = U_{DD}I_{Don}\frac{tri + tfu}{2} + Q_{rr}U_{DD} \quad (2.59)$$

The MOSFET switch off, where the current is turned off and the voltage rises gives a similar energy loss, but the losses in the diode can be neglected,

$$E_{off} = \int_0^{tru+tfi} u_{DS}(t) \cdot i_D(t)dt = U_{DD}I_{Doff}\frac{tru + tfi}{2} \quad (2.60)$$

The product of the switching frequency, f_{SW}, and the switching energies gives the related loss in terms of power,

$$P_{sw} = f_{sw}(E_{on} + E_{off}) \quad (2.61)$$

In the switching process of each MOSFET, the total turn-on and turn-off times are of interest. It is used to design the gate driver in an inverter application and corresponds to the blanking time, used to avoid current shoot-through. As indicated above, the total switching time originates from the internal capacitance in the device. In an applied study it is usually more straight forward to use the time instances [19]. The total turn-on time t_{on} is defined as the sum of the current rising time t_r and the turn on delay $t_{d(on)}$. The total turn-off time t_{off} is defined as the sum of the current fall time t_f and the turn-off delay $t_{d(off)}$ [17].

3

Design Approach for the SynRM

In this Chapter the design approach of the SynRM concepts and the PMaSynRM are presented. Important design variables are presented and explained along with how they are used to describe the rotor geometry. In figure 3.1 a typical rotor geometry for a SynRM is shown and the parts of the rotor are highlighted.

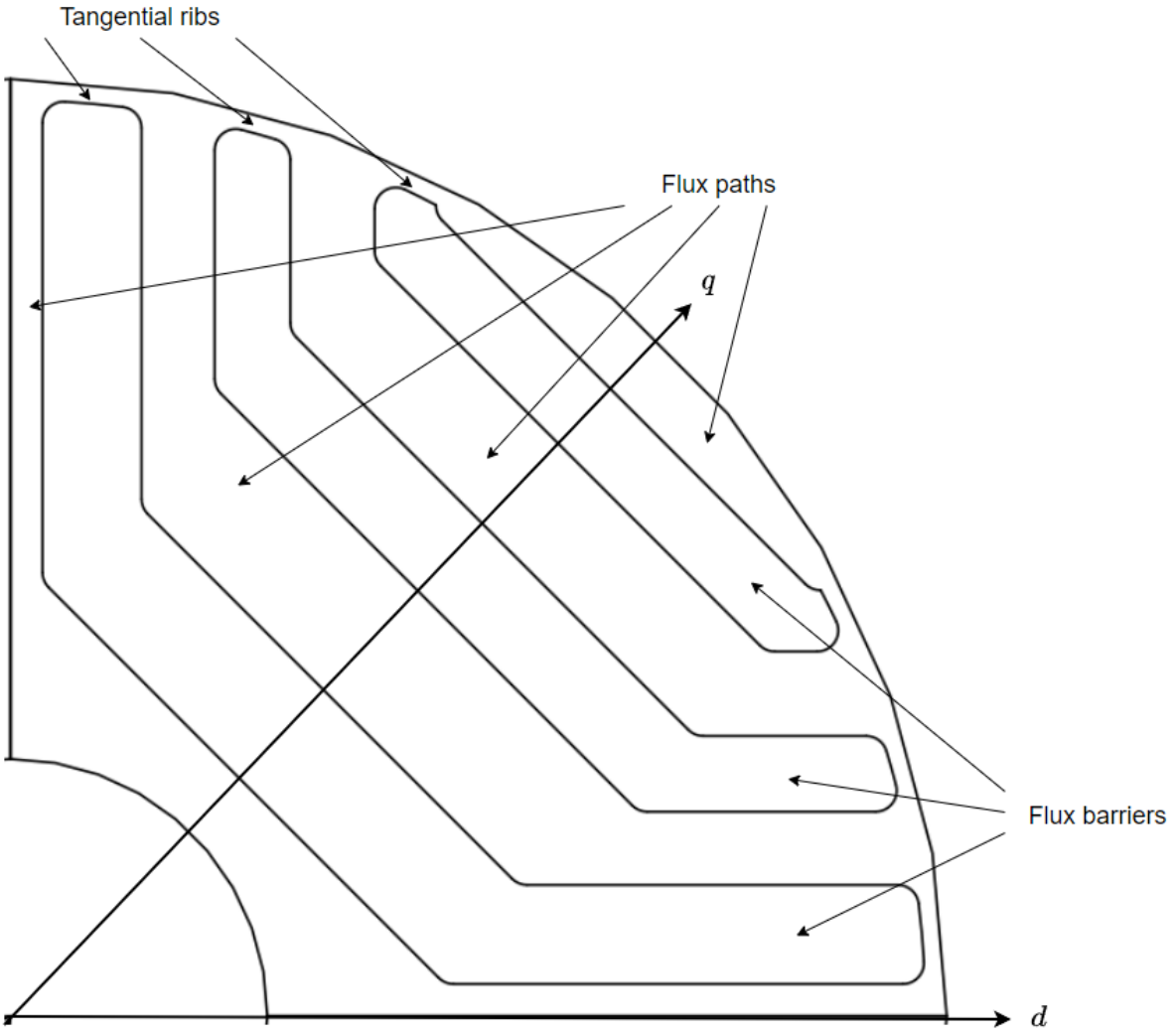

Figure 3.1: Description of different parts of the rotor

3.1 TLA and limitations

A reoccurring problem with the SynRM design in this project is that the motor that is being designed is relatively small compared to existing SynRMs. In this project, a SynRM is developed for use in handheld applications such as chainsaws while their most popular use is in replacing Induction Machines (IM) for pump applications and automotive use [20]. The small size will lead to problems due to manufacturing limitations. With manufacturing limitations, it is meant how small a profile in the rotor and stator lamination can be made. Because the idea of the SynRM is to keep the cost down it is assumed that the motor will be transversally laminated anisotropic (TLA), and not based on axially laminated anisotropic (ALA) since ALA is more complex and more expensive than TLA [20]. TLA means that the laminations are sheets with the shaft as the center axises and ALA means that the lamintions are instead in layers out from the shaft towards the edge of the motor. With TLA an assumption was made that due to production tolerances, no profile in the stator or rotor should be smaller than 0.5 mm. This means that the tangential ribs in the rotor will initially have a thickness of 0.5 mm.

3.2 Air gap length

It is important to keep the air gap length as low as possible for a SynRM. This is because more air in the magnetic-flux path leads to more reluctance which in turn leads to a lower inductance value, see (2.2) and (2.3). In [21] it is shown that L_d is affected by the size of the air gap while L_q is not. This is because there already is a lot of reluctance in the q-axis direction because of the flux barriers so the extra flux barrier that is the air gap gives a negligible affect. A smaller L_d when L_q remains constant will according to (2.15) lead to less torque production.

3.3 Insulation ratio

The insulation ratio(K_w) describes the relationship between the amount of air and the amount of iron in the direction of either the d- or q-axis. See figure 3.1. This ratio is the main design factor to produce more torque with a SynRM. Since the this ratio is directly related to the size of L_d and L_q [22]. Mathematically the insulation ratio is defined as

$$K_w = \frac{\textbf{Amount of air}}{\textbf{Amount of iron}} \tag{3.1}$$

The insulation ratio is a way to describe the relationship between the need for flux barriers and much reluctance in the direction of the q-axis while also not making the flux paths along the d-axis too thin so that the steel becomes saturated and L_d starts to decrease. Usually, the ideal insulation ratio is somewhere between 0.6-0.8 [22], [23], but it can be much lower, down to 0.2 depending on barrier shape [24]. This will be the main design aspect for any barrier concept for a SynRM.

3.4 Number of flux barriers

Two factors are of interest when choosing the number of flux barriers (h). The torque production and the torque ripple. There are no simple rules for setting the optimal number of flux barriers. The insulation ratio between the steel and air is the main factor, but it is known that the torque and power factor increases with an increased number of barriers [25]. In [22] a general rule for the number of barriers is presented based on the minimization of torque ripple. It states that

$$n_r = n_s \pm 4 \tag{3.2}$$

where n_r is the number of rotor slots per pole and n_s is the number of stator slots per pole. Rotor slots in this case mean the sum of all endpoints of flux barriers. With endpoints it is meant where the flux barriers meet the tangential ribs. So twice the value of the number of flux barriers. In general +4 is optimal to reduce the torque ripple. However, this is limited by manufacturing limitations, depending on the size of the rotor. This is discussed when the number of barriers is chosen for each design.

3.5 Rotor slot pitch angle

Torque ripple is an inherent problem in SynRMs. When the machine spins the reluctance path is not constant. The torque ripple in a SynRM comes from the changing reluctance when a rotor slot passes a stator slot opening [26], [22].

There are different methods for torque ripple reduction such as the constant rotor slot pitch or more complex methods such as asymmetric barrier design [26]. However, since it is not the focus to design only a low torque ripple machine the constant rotor slot pitch angle will be used to try to minimize the torque ripple without affecting the torque production and power factor too much. The rotor barrier endpoints will be equally distributed along the periphery of the rotor. Since this has been shown to minimize the torque ripple [22]. The flux barrier endpoints are calculated as

$$\theta_i = \frac{(2h-1)\alpha_m}{2} \tag{3.3}$$

Where θ_i is the position angle of each barrier, see figure 3.3, and α_m is the rotor slot pitch angle. To introduce another degree of freedom, the rotor displacement angle β_s is introduced [23]. β_s is controlled to minimize the torque ripple of the machine and α_m is calculated as

$$\alpha_m = \frac{\frac{\pi}{2n_p} - \beta_s}{h + 1/2} \tag{3.4}$$

where β_s is treated as a design variable for the design of the SynRM.

3.6 Approach to the rotor geometries

To design the rotor for the SynRM, two concepts were adopted for the rotor design. The first one utilizes circular flux barriers in the rotor, see figure 3.2. The second approach

instead uses straight flux barriers with arms at an angle to the tangential flux barrier, see figure 3.3.

3.6.1 Circular flux barriers

For the circular flux barriers, the size of the flux paths and flux barriers are constant along their arcs and only one insulation ratio can be properly defined along the q-axis(K_{wq}). The design parameters for the circular flux barriers can be seen in table 3.1 and in figure 3.2.

Table 3.1: Geometric design parameters for circular flux barriers

Parameter	**Description**
$W_{q,1}$	Width of flux barrier 1
$W_{q,2}$	Width of flux barrier 2
$W_{q,3}$	Width of flux barrier 3
$W_{q,4}$	Width of flux barrier 4
β_s	Rotor displacement angle

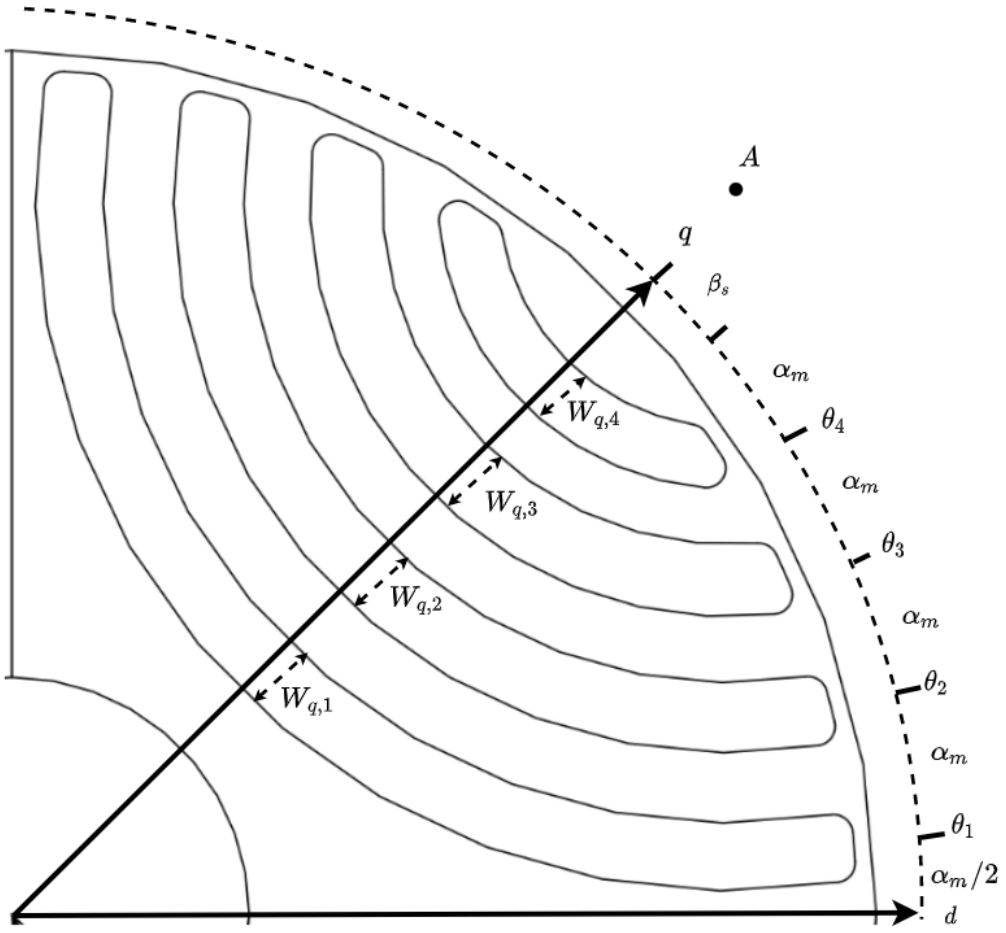

Figure 3.2: Geomtry parameters for SynRM with circular flux barriers

In the case of circular flux barriers, the relation between the insulation ratio in the q-axis and the width of the flux barriers is as follows

$$K_{wq} = \frac{W_{q,1} + W_{q,2} + W_{q,3} + W_{q,4}}{R_{rotor} - R_{shaft} - (W_{q,1} + W_{q,2} + W_{q,3} + W_{q,4})} \tag{3.5}$$

where R_{rotor} is the radius of the rotor and R_{shaft} is the radius of the shaft. The point A in figure 3.2 represents the center point of the flux barriers and it is aligned on the q-axis so that the flux paths become symmetrical. The endpoints of the rotor slots are controlled by β_s and α_m and calculated using (3.3)

3.6.2 Straight flux barriers

The second concept for the flux barriers is to use straight barriers in 3 segments. For this design, another parameter can be introduced which is the insulation ratio in the d-axis. A potential problem with the circular design approach is that it is not ideal for the flux paths to retain the same thickness. It is therefore of interest to study the straight flux barrier concept as well. The concept also leads to the possibility of more easily implementing magnets into the rotor design to create a PMaSynRM.

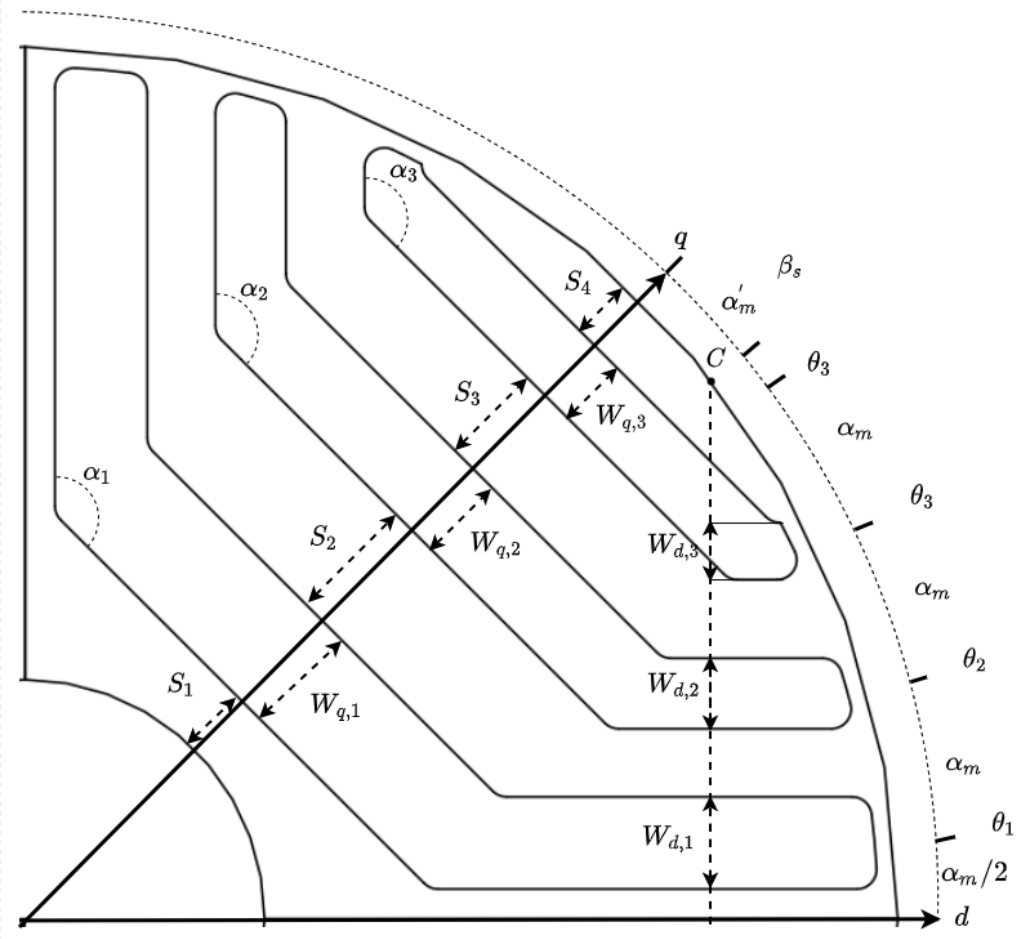

Figure 3.3: Parameters for SynRM design with Straight flux barriers

This design concept is parameterized according to figure 3.3. Immediately it is decided that the arm angles α_1 to α_3 are set 135° since this is a suitable value to achieve the highest torque possible [9]. However, a problem with this design concept is that there will be a lot of varying parameters compared to the approach with circular flux barriers. To solve this problem a simplified model is used that can be seen in more detail in [23]. The model makes several simplifications to minimize the design variables to three variables. These simplifications are as follows

- The windings in the stator is seen as ideal
- The effect of the distribution of MMF are not considered
- The effects of saturation, stator slotting effects and drop of magnetic potential in the iron are all neglected.

The rotor slot pitch angle and the rotor displacement angle β_s are used in the same way as for the first design to control the torque ripple and are calculated according to equation 3.4.

3.6.2.1 Flux barrier sizing in d-axis and q-axis

The motor magnetic force (MMF) experienced by the rotor is assumed to be sinusoidal in both d- and q-axis. When this is true a step function can be derived for the MMF in each axis direction for each flux path in the rotor [23] as in figure 3.4. With h flux barriers the average MMF in each axis experienced by the rotor segment can be calculated as

$$f_{d,i} = \frac{1}{\Delta\theta_i}\int_{\theta_{i+1}}^{\theta_i} \cos\theta d\theta \ = \frac{\sin\theta_{i+1} - \sin\theta_i}{\theta_{i+1} - \theta_i} \ i = 0, ..., h-1 \tag{3.6}$$

$$f_{q,i} = \frac{1}{\Delta\theta_i}\int_{\theta_{i+1}}^{\theta_i} \sin\theta d\theta \ = \frac{\cos\theta_i - \cos\theta_{i+1}}{\theta_{i+1} - \theta_i} \ i = 0, ..., h-1 \tag{3.7}$$

Where $f_{d,i}$ is the p.u. MMF in the d-axis, $f_{q,i}$ is the p.u MMF in the q-axis and the angles are defined as in figure 3.3. It should be noted that θ_0 is the same as $-\theta_1$ because the flux path along the d-axis is only half and shared with another pole. The important thing is that $f_{q,1} = 0$.

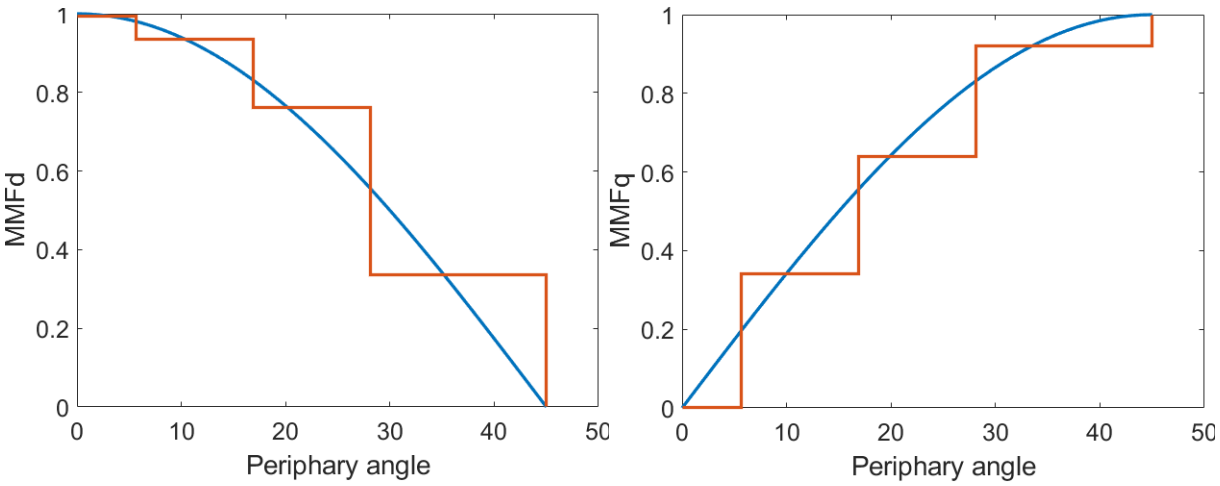

(a) d-axis MMF

(b) q-axis MMF

Figure 3.4: p.u MMF in d- and q-axis

By assuming that the permeance across each individual barrier is constant a relation can be determined between the average MMFq and the width of the barriers along the q-axis [23]. This relation is as follows

$$\frac{W_{q,i}}{W_{q,i+1}} = (\frac{\Delta f_{q,i}}{\Delta f_{q,i+1}})^2 \; i = 0, ..., h-1 \tag{3.8}$$

This relationship only holds for the assumption stated earlier and potentially other assumptions about the permeance distribution could be made [23]. There are now $h-1$ equations, but to determine the width of all the flux barriers along the q-axis an equation for the sum of all the flux barrier widths is introduced. The insulation ratio along the q-axis together with the size of the rotor can be used to determine the sum of all flux barrier widths in the q-axis. The sum is calculated as

$$\sum_{i=1}^{k} W_{i,q} = \frac{R_{rotor} - R_{shaft}}{1 + 1/K_{wq}} \tag{3.9}$$

To have almost constant flux density throughout the flux paths the thickness of the flux path have to be proportional to the average size of the MMFd in a given flux path. This results in two relations between the MMFd of the flux barrier- and flux path widths in the q-axis. The relations are as follows

$$\frac{2S_{q,1}}{S_{q,2}} = \frac{f_{d,1}}{f_{d,2}} \tag{3.10}$$

$$\frac{S_{q,i}}{S_{1,i+1}} = \frac{f_{d,1}}{f_{d,2}} \; i = 2, ..., h \tag{3.11}$$

where $S_{q,i}$ is the width of the flux path along the q-axis. The multiplication with 2 in (3.10) comes from the fact that the flux path aligned with the d-axis is shared with another pool. It can also be shown to be a product of how the angles are defined in (3.6). Another equation still needs to be defined for the sum of all the flux path widths so that each width can be calculated. The sum is calculated as

$$\sum_{i=1}^{k+1} S_{i,q} = \frac{R_{rotor} - R_{shaft}}{1 + K_{wq}} \tag{3.12}$$

With this, the placement and width of all flux barriers along the q-axis can be determined. For the flux barriers in the d-axis, it is assumed that the width is proportional to the width of the flux barriers in the q-axis

$$\frac{W_{q,i}}{W_{q,i+1}} = \frac{W_{d,i}}{W_{d,i+1}} \tag{3.13}$$

Now a reference point for the segments and width of the flux barriers in the d-axis must be defined. This is done by introducing an imaginary point C on the circumference of the rotor, see figure 3.3. This point is defined by assuming that $\beta_s = \frac{\alpha_m}{2}$ and calculating α_m for this point. In this case, the rotor slot pitch angle is

$$\alpha_m^{'} = \frac{\frac{\pi}{2p}}{h+1} \tag{3.14}$$

Further, point C is defined as $\frac{3}{4}\alpha_m^{'}$ from the q-axis. Point C is positioned along the conventional path [23] along the dotted line from C to the d-axis. The position of C is not changed with a change in β_s so the insulation ratio in the d-axis can be calculated along the imaginary line from point C to the d-axis. This gives the final relation needed to calculate the width of the flux barriers as

$$\sum_{i=1}^{k} W_{i,d} = \frac{R_{rotor}(\frac{\pi}{2p})}{1 + 1/K_{wd}} \tag{3.15}$$

where K_{wd} is the insulation ration in the d-axis direction, see figure 3.3. Now the rotor geometry is defined by only three parameters seen in table 3.2. So, in the end, this design approach will yield fewer design variables than in the case with circular flux barriers.

Table 3.2: Geometric design parameters for Straight flux barriers

Parameter	**Description**
K_{wq}	q-axis insulation ratio
K_{wd}	d-axis insulation ratio
β_s	Rotor displacement angle positions

3.7 Mechanical considerations

Because the rotor of a SynRM contains a lot of air and is not as solid as in other electrical machines, the rotor becomes mechanically weak. The main force that acts on the structure is the centripetal force (F_c) from when the machine is rotating, described as

$$F_c = mr\Omega_r^2 \tag{3.16}$$

where m is the mass and r is the radius of a given point in the rotor. Another important load case for the application of the motor in this project is a sudden stop of the rotor. Meaning that a large braking torque is applied to the shaft

$$T_b = mr^2 a_\Omega \tag{3.17}$$

where T_b is the braking torque and a_Ω is angular acceleration in rad/s^2

To counteract these mechanical loads the thickness of the tangential rib can be changed and radial ribs can be added between the flux paths along the q-axis [25],[9]. These parameters are shown in figure 3.5 where $w_{t,i}$ are the tangential ribs and $w_{r,i}$ are the radial ribs.

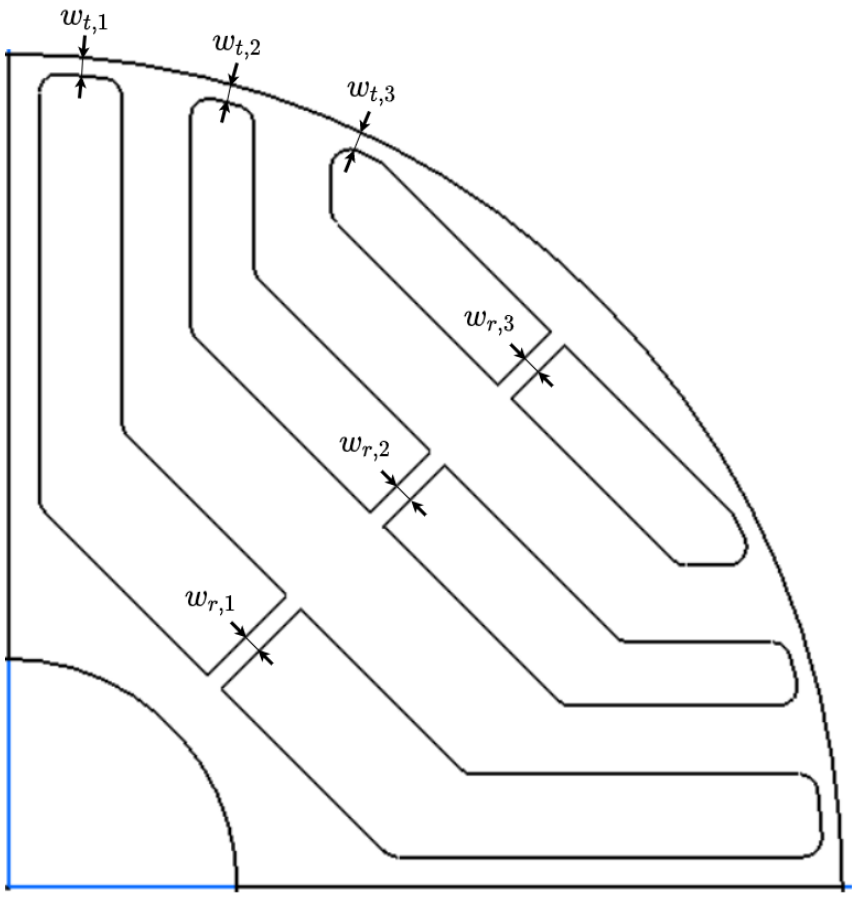

Figure 3.5: Radial and tangential ribs

The dimensioning operating point for the radial ribs is when the motor is operating at max speed. The need for the radial ribs are dependent on the size and speed of the motor. Mechanical strength is measured in stress (σ) or alternatively von Mises stress (σ_v) which is the equivalent tensile stress. This stress is a summation of all stress in a given point from all dimensions. For 2D and 3D von Mises stress can be calculated as

$$\sigma_v = \sqrt{\frac{(\sigma_{xx} - \sigma_{yy})^2 + (\sigma_{yy} - \sigma_{zz})^2 + (\sigma_{zz} - \sigma_{xx})^2 + 6(\sigma_{xy} + \sigma_{yz} + \sigma_{zx})^2}{2}} \tag{3.18}$$

where σ_{xx} is the stress in the x-axis, σ_{yy} is the stress in the y-axis, σ_{zz} is the stress in the z-axis, σ_{xy} is the stress in between the x-axis and the y-axis, σ_{yz} is the stress in between the y-axis and the z-axis and σ_{zx} is the stress in between the z-axis and the x-axis. Usually a safety factor between 2 and 3 is desirable for a SynRM rotor [13]. Meaning that the maximum von Mises stress on the rotor in any point should be 2 to 3 times less then the yield strength (σ_v) of the material [13]. Typically the yield strength for steel is between 300 and 470 MPa.

From a performance point of view, ideally, there should be no radial- or tangential ribs since these will be paths that the flux can take resulting in leakage flux and less torque production in the motor [25]. The tangential ribs will always be present since obviously the flux paths need to be connected to the rest of the rotor.

3.8 Magnet assisted

For a concept with straight flux barriers, it becomes reasonable to add magnets to the rotor. However, it is not always best to simply add magnets in all possible locations in the rotor. Placing magnets along the q-axis and the arms of the rotor will always yield the most torque [27], but placing magnets only along the q-axis can increase the torque without significantly increasing the torque ripple. Placing magnets in only the arms compared to only along the q-axis is not ideal since the torque gain will be less compared to if the magnets were only placed along the q-axis of rotor [27]. Torque ripple will also increase when magnets are placed only in the arms compared to only along the q-axis [27].

Placing magnets closer to the rotor core is also beneficial due to that the magnets get less demagnetized from the stator flux. This is important, especially for the ferrite magnets since they are more susceptible to demagnetization than neodynium magnets [27]. Demagnetization effects are however something that has not been studied in this report and was considered to be outside the scope since the main focus was not to design a PMaSynRM.

4
Case Setup

In the this chapter, the starting point for the analysis will be explained. The performance demands for the SynRM will be presented. A reference SynRM had been made before the project start, the relevant features of this motor will be presented. The outer dimensions for the drive system will also be presented, such as battery voltage.

4.1 Reference IPM motor

The reference point of the project was a PMSM that was of the type IPM motor in use for handheld applications today. From this motor, the maximum torque, base speed, max speed, and outer diameter were set as fixed design parameters for the SynRM project. The goal was that the SynRM would fit within the same diameter space and that the mechanical performance should be achieved with the SynRM as well. The p.u. values mentioned in the report will all be in relation to this machine's outer diameter, stack length, torque, and maximum speed. It was decided that it would not be realistic to match the torque ripple of the IPM motor since SynRMs have inherently more torque ripple than an IPM motor. Because of the application however, and the very low torque ripple of the IPM, it was decided that a goal was to keep the torque ripple below 10 %. In table 4.1 the performance parameters are shown for the IPM motor.

Table 4.1: Reference IPM motor Performance parameters

Parameter	**Value**
Max torque	1.0 [p.u]
Torque ripple	2.3 %
Phase voltage RMS at base speed and max torque	33.23 [V]
Phase Current RMS at max torque	46.1 [A]
PF at base speed max torque	0.835
Efficiency at base speed max torque	94.7 %
Stack length	1.0 [p.u]

4.2 Reference SynRM

Before the start of the project, a SynRM reference design had been made as a starting point for the project. This design had not been fully tested and was therefore implemented in JMAG-designer so that a fair as possible comparison could be made with the

design produced in this project. The design specifications and performance result for the reference design can be seen in tables 4.2 and 4.3.

Table 4.2: Reference SynRM design parameters

Parameter	**Value**
Stack length	1.81 [p.u]
n_p	2
Q	24
N	5
r	2
y	5
Fill factor	52.9%
Stator steel	M330-50A
Rotor steel	M270-35A
Air gap length	0.35 [mm]
I_{max}	60 [A]

Table 4.3: Reference SynRM Performance parameters

Parameter	**Value**
Max torque	0.96 [p.u]
Torque ripple	42.7 %
Phase Voltage RMS at base speed and max torque	44.2 [V]
PF at base speed max torque	0.527
Efficiency at base speed max torque	85.1 %

The maximum RMS current used for the reference SynRM was larger than that of the IPM motor since an early assumption was that due to the SynRM's problems with low power factor the current would need to be higher to achieve the same torque. The higher current with a lower power factor also means that voltage would not have to increase as much to compensate for the reactive power. The outer diameter of the stator was the same as that of the IPM motor.

4.3 Motor and drive system specifications

The drive system will be evaluated from a system perspective where the power flow is of certain interest. Mainly high power carrying components and related parameters will be assessed with the aim to verify components' dimensions and to minimize losses. In this system perspective, a battery will represent the power input and the motor shaft power will be addressed as the final delivery and the outermost component of the system boundaries.

4.3.1 Drive

The specifications that will dimension and limit the drive system are derived from the battery voltage and also an expected maximum power. The values are presented in table 4.4. Besides the actual battery voltage, the 3-phase RMS current for the motor is used as the second metric for this dimensioning. Reactive power in the system is also of interest since it affects the component selection, however, it is not regarded as a system requirement but rather a unit to analyze.

Table 4.4: System specification for the drive system

$I_{max,rms}$	60 [A]
U_{batt}	94 [V]

5
Motor Design

In this section the design process for designing the SynRM will be explained. Challenges and different design choices will be discussed and motivated. The overall analysis approach for the SynRM is described by the flowchart in figure 5.1.

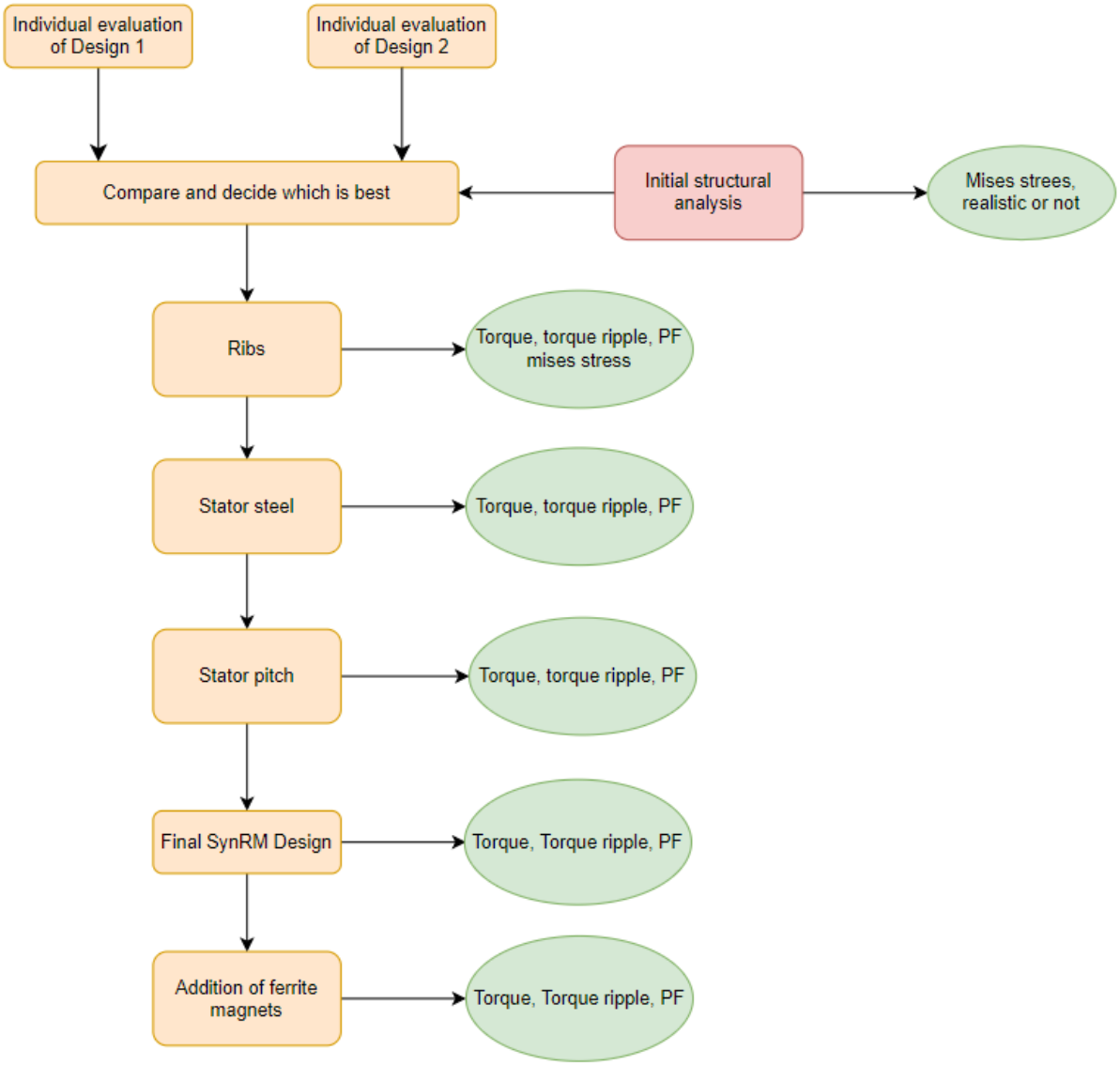

Figure 5.1: An overview of the SynRM Design process

All FEM simulations were made using JMAG-designer. The geometries were set up and parameter sweeps were performed to study the performance and in the end find the best possible design. For every individual case created by the parameter sweeps, the torque is calculated at the maximum torque angle. The d-axis of the rotor was aligned with the a-phase. All models made in JMAG-designer was a 2D model in order to speed up the design and analysis process.

5.1 Stator

The most crucial part of the SynRM design is the design of the rotor itself. This is because the rotor is the main difference between a normal IPM motor and a SynRM. For this reason, it was decided that the same stator would be used as the one presented for the reference SynRM design in the case setup. This also resulted in a rotor of similar size which lead to a more fair comparison between the designs. The only difference for the stator design was that the winding pitch (y) was changed to be full pitch with the possibility of changing the pitch later. This was done since theoretically for full pitch, the motor torque would be the highest. Since according to (2.2), (2.3) and (2.4) the dq-inductance will be higher, resulting in a higher torque. Ideally, a SynRM should have 2 or 3 pole pairs [20]. However due to problems with saturation and manufacturing limitations because of the small size of the SynRM, it was decided that the SynRM would have 2 pole pairs. Since the stator used in this project has 6 slots per pole. The number of barriers suggested according to (3.2) would be 1 to 5 barriers when no manufacturing limitations are taken into account. Another aspect that was kept constant from the reference SynRM was the same air gap thickness at 0.35 mm. Based on what was discussed in section 3.2 it was also desirable to keep the air gap thickness very low.

The stator from the SynRM reference design was also known to give a reasonable current density for its maximum current. Another aspect that was also studied for the stator was the effect of different steels on the performance of the machine. Initially, the steel was kept the same, but this steel was quite a low grade and therefore the final design was also evaluated with the same steel as in the rotor.

5.2 Rotor material

As was discussed in section 3.7, a problem with SynRMs is the mechanical stress due to there being a lot of air in the rotor and not a lot of structural support. If profiles are made thicker to help with mechanical stress. It will inevitably lead to a smaller power factor due to leakage flux or too small an insulation ratio between steel and air. Therefore the rotor steel was chosen as M270-35A since the yield strength was high at $\sigma_v = 450MPa$, see appendix A.2. The losses and magnetic conductivity of the steel are also important as was presented in section 2.3.3. M270-35A was chosen with the goal that the higher yield strength would lead to radial ribs not being needed and therefore the SynRM would not lose performance due to more leakage flux.

5.3 Stack length

Since SynRMs, in general, have a poor PF and lower power density [28]. It was decided that initially a longer stack length would be used for the analysis. The stack length was set to 58% larger than the reference IPM motor. Later the stack length was changed to achieve the same torque result as the IPM motor since the motor power density and size were also of importance. By decreasing the length of the motor, the voltage needed for a given base speed would also decrease.

5.4 Performance parameters and operating point

The operating point that the SynRM was designed for was the base speed (ω_n) with the maximum current to operate at max torque. As mentioned earlier the current angle used was the maximum torque angle. At this operating point, the torque and torque ripple was studied. It was also of interest to study the power factor and voltage requirements at this operating point. The voltage and power factor aspects were important since the motor was intended to be used in a handheld application. Less power factor means a larger motor and an increase in voltage could mean that a larger battery would need to be used which was considered undesirable for a handheld product. The base speed for this machine, ω_n, is 73.8% of ω_{max}. At this operating point, the performance parameters that have been studied are

- Average max torque
- Torque ripple %
- Efficiency
- Power Factor
- Voltage

Since all the tests were done for maximum current and speed, the winding losses only changed with change of the pitch. The main difference in efficiency came from the change in rotor design which led to different levels of iron loss.

5.5 Design 1

Design 1 was implemented according to section 3.6.1 with circular flux barriers. The design procedure for the design 1 is presented in the flow chart in figure 5.2.

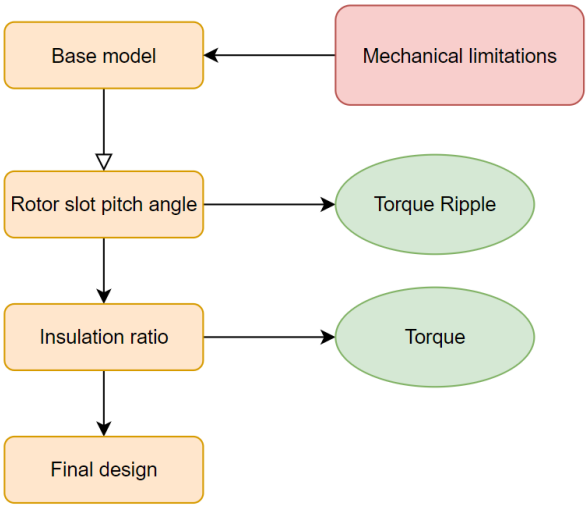

Figure 5.2: Rotor design 1 flow chart

The number of barriers selected for this case was 4 since this was the most amount of barriers that could be implemented without any manufacturing constraints in that certain profiles became too thin while still having some margin for design iterations.

For the design 1, the flux barriers were initially all set to have the same thickness. When the flux barriers have a constant thickness along the pole, the ideal insulation ratio is somewhere between 0.6-0.7 [29]. For the initial design an insulation ratio of 0.7 was used.

A good starting value for β_s is $\beta_s = \alpha_m/2$ [23]. This results in that $\alpha_m = 9°$. The initial design was implemented and analyzed in JMAG-designer. The results were then used as the baseline for design 1. With the initial design made the rotor slot pitch angle was studied by varying β_s to reduce the torque ripple. The center point A was treated as a constant parameter. The value was set so that the inner most flux barrier would be reasonably close to the shaft without the flux path along the d-axis becoming to thin at the thinnest point. The center point was 26 mm from the origin on the q-axis.

When it comes to the size of the flux barriers it was decided that an optimization tool in JMAG-designer would be used since the thickness of the barriers have to be changed individually. This was a drawback of this design since it was harder to concretely say how the barrier thickness should change in relation to each other compared to design 2. The optimization tool lets the barrier size vary within a given span and the goal was to maximize the torque while also trying to minimize the torque ripple. The algorithm used was the Multi-Objective Genetic Algorithm(MOGA). An in-depth explanation of how the algorithm works can be found in [30]. In this project, it allowed for the handling of more than one parameter, namely the torque and the torque ripple, to be taken into account while trying to find a good width for each of the flux barriers. The algorithm works in generations where for each generation it was given, a population size of $10n_{var}$ where n_{var} was the number of changing parameters. With each generation, the algorithm would improve the guess for the current population values based on the results of the previous generation. The number of generations was dependent on how quickly the algorithm

converges. In this case, it was 15 generations. Making for 600 different cases.

5.6 Design 2

Design 2 was implemented according to section 3.6.2. The individual design process for design 2 is presented in figure 5.3

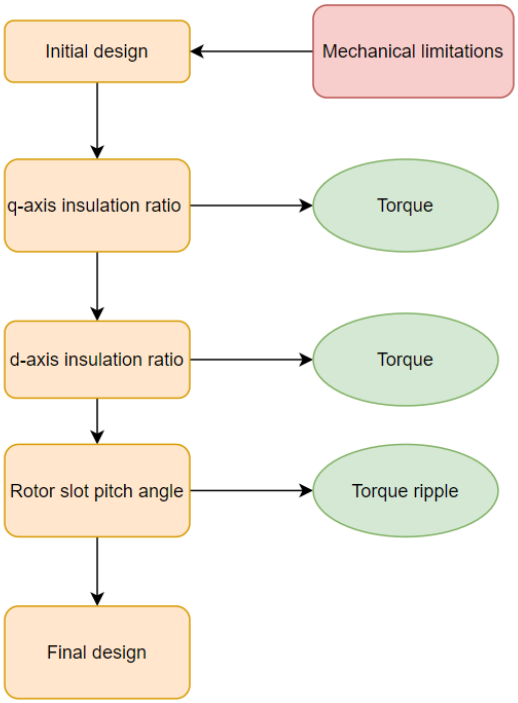

Figure 5.3: Rotor design 2 flow chart

For this case, the number of flux barriers was limited to 3 since with the presented model in section 3.6.2 it was not feasible to implement anymore than this. The outer barrier would become too small to be realistic to manufacture. Since more barriers result in higher torque it was decided that no less than 3 barriers would be studied. Same as for design 1, the initial value of β_s was set to $\beta_s = \frac{\alpha_m}{2} = 5.625°$. The displacement angle β_s affects the thickness of the individual barriers even if the insulation ratio stays the same. This is important since the flux barriers might become unreasonably thin for certain values of β_s. The initial value of the insulation ratios were set $k_{wq} = 0.7$ and $k_{wd} = 0.5$.

With this in mind, the insulation ratios were varied first starting with K_{wq} since this was the parameter that most affected the torque [23]. Secondly K_{wd} was varied. Finally, the torque ripple was reduced by studying the effects of β_s. A lower limit for the insulation ratios had to be set based on size limitations. The lower limit for $K_{wq} = 0.4$ and $k_{wd} = 0.5$. When studying the variables in JMAG-designer a setting was used that eliminates any geometries that result in geometry collision so that no unnecessary or unfeasible cases were calculated.

5.7 Structural analysis

The final design of both designs 1 and 2 were evaluated for structural integrity. This was done by importing the rotor geometry into CATIA, see figure 5.4. The imported model of the rotor was only one lamination thick since both the centripetal force and the braking torque are based on the rotor's mass. Meaning that the force stays the same at any given point along the center axis through the rotor. In CATIA to simulate the centripetal force, the lamination was set to spin at the max speed of the motor. For the second load case, a deceleration of 100000 rad/s^2 was applied to the body to simulate a rapid stop of the motor. This value was set after discussions with the supervisor for the project. The two load cases were individually studied and then the total stress was added together by applying max speed and the deceleration load at the same time. The scenario simulates that the machine was operating at ω_{max} and experienced a sudden stop. This was ultimately the dimensioning case for the rotor.

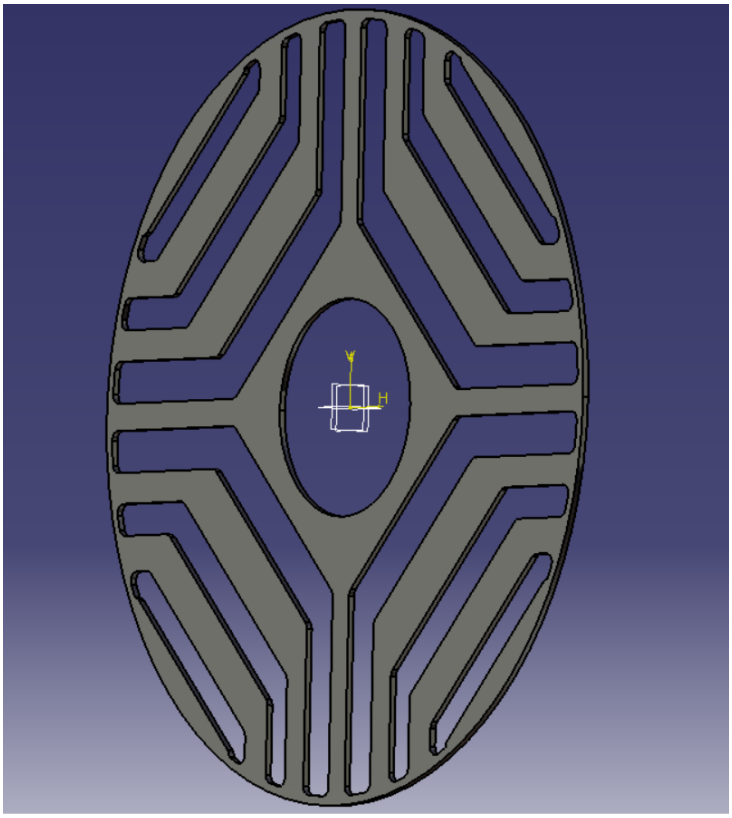

Figure 5.4: Imported lamination in CATIA

When working with the structural integrity it was decided that fillets should be placed in the corners of the flux barriers as in figure 5.5. Since sharp corners are not desirable because stress will concentrate in these points. By rounding the corners with fillets stress concentration was lowered and from the initial result of the mechanical analysis, it was decided that these would be needed. The radius of the fillets was set to 0.5 mm, but the size was not studied further since the result of the mechanical analysis showed that a larger size would not be needed. Also increasing the size of the end fillets leads to more

iron in the q-axis which in turn decreases the saliency ratio and torque production of the SynRM [25].

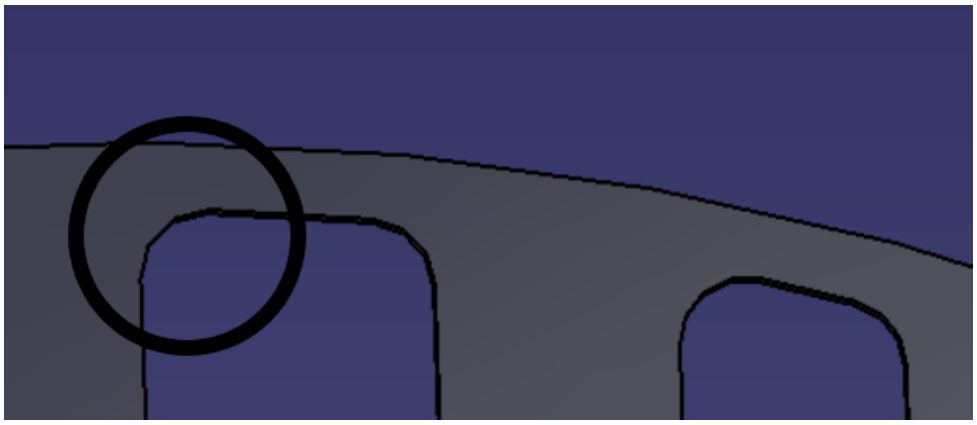

Figure 5.5: Barrier fillets

After the mechanical results and performance data had been produced it was decided that enough information had been gathered to decide which design concept was best. Except for performance and mechanical durability factors, consistent results were also considered when picking which design concept to study further.

The effects were then studied of implementation of the radial ribs. To see how much they affect the torque and power factor, while also improving the structural integrity of the rotor. Two sizes of ribs were suggested. The first was at 0.5 mm thick which was decided based on the lowest profile size allowed. Also, a rib of 1 mm was used to study the effects of increasing the size of the rib. Even though the ribs might not be needed it was still of interest to study their effects on performance since other mechanical stresses exist that are outside the scope of this project. Such as vibrations and continuously changing frequency in the rotor over time.

5.8 PMaSynRM by adding ferrite magnets

As was mentioned in section 2.3.5 it was of interest to investigate the effects that the addition of ferrite magnets has on the performance of the motor. Ferrite magnets are the only magnet type that was studied in this project since it was a lot cheaper and a lot less polluting than other PM:s as was discussed in chapter 1. With the addition of the ferrite magnets, more masses has been added to the rotor. From the manufacturer of the magnets it was known that the tensile strength of the magnets was only 35 MPa, it was therefore decided that the magnets would be implemented with radial ribs in the rotor structure to avoid damage to the magnets due to high mechanical loads on them. The ferrite material used was FB5D. The full magnet specifications can be found in appendix A.1, but the most important parameters are presented in table 5.1.

Table 5.1: FB5D parameters at 20° C

B_r	0.415 [T]
H_c	254.6 [kA/m]
BH_{max}	32.6 [kJ/m^3]

The magnets were implemented in two different ways. The first had only magnets along the q-axis as in figure 5.6a. For the second case, the magnets were placed in the arms as well. However, an assumption was made that 2 mm would be the thinnest magnet size possible for the ferrite magnets, so for this case, realistically magnets can only be placed in the first barrier arms as in figure 5.6b. Because of the fillets in the flux barriers the magnets were placed 0.5 mm from the corners so that they would fit inside the barriers while still keeping a rectangular form.

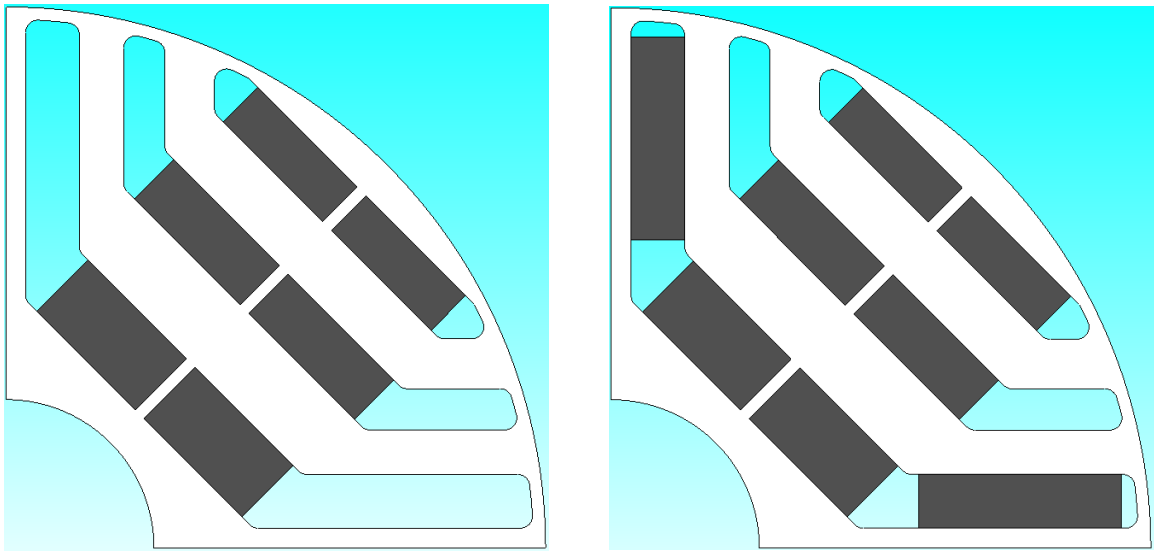

(a) Magnets in the center barriers

(b) Magnets in the arms

Figure 5.6: Magnet placement

5.9 Mapping of the motors

When the design was finished for the SynRM and PMaSynRM, the next step was to determine the parameters of the motor. The mapping of the motors was done with the help of JMAG-RT. In JMAG-RT the operating points were defined as parameter sweeps. The varied parameters were the current magnitude, current angle, and rotor speed Ω_r. In table 5.2 the operating points are described in more detail.

Table 5.2: Mapping parameters

Parameter	**min**	**max**	**Divisions**
I_{mag}	1 [A]	91 [A]	18
β_c	0 [°]	360 [°]	72
Ω_r	0.077 [RPM p.u.]	1 [RPM p.u.]	12

For the SynRM the parameters that were needed to be known were L_d and L_q. Since these vary with current as in (2.10) and (2.11) they are determined by current magnitude and the current angle. For the PMaSynRM L_d and L_q needed to be known, but also ψ_{pm}. However the flux linkage could only be calculated for d- and q-axis. By looking at (2.27) it can be shown that ψ_{PM} can be calculated as

$$\psi_{pm} = -\psi_q, \; i_q = 0 \tag{5.1}$$

since when $i_q = 0$ the flux linkage in the q-axis only consist of ψ_{pm}.

In the mapping of the motor, losses were also calculated for various speeds and currents. This was done so that the effect of losses would be part of the model implemented in Simulink.

5.10 Cost analysis of the motors

As mentioned in section 1.1, an important motivation for using a SynRM would be the lower cost due to not using neodymium magnets. The motor cost was therefore calculated and compared between the SynRM, IPM motor and the PMaSynRM. By only looking at the materials that actively lead to a power output in the motors (hence, active materials), a simple way of comparing costs could be derived. The method includes material cost and material weight. And also entail a simple model for the manufacturing costs, where a weighting factor, f_{mf}, is assumed for each subpart to resemble the total costs for producing the subpart from its material [31]. The material costs were taken from a report compiled in 2019 [31] and in consultation with the suppliers and the supervisor to get a reasonable value in price per kilogram. The weighting factor for the ferrite magnet is here assumed to be the same as the different steels and the NdFeB magnet. Two cases was created for the prices. One based on typical historical prices for the materials, and one based on what the prices were at the time of this project, spring 2022. This was done because at the time, the prices of neodymium and copper had risen significantly. The final model for the cost analysis is presented in table 5.3.

Table 5.3: Cost analysis model

Material	**Case 1 (Normal) [€/kg]**	**Case 2 (Today) [€/kg]**	f_{mf}	**Weight [kg]**	**Material Cost [€]**	**Cost [€]**
Stator						
M270-35A	1.5	1.5	1.5			
Copper	6	9.5	1.5	TBD	TBD	TBD
NO20	1.6	1.6	1.5			
Rotor						
M270-35A	1.5	1.5	1.5			
Ferrite FB5D	1.45	1.45	1.5	TBD	TBD	TBD
NdFeB N45SH	60	100	1.5			
M800-50A	1.2	1.2	1.5			
Total				TBD	TBD	TBD

The material weight of the motors was determined using JMAG-designer. This was done by measuring the cross-section area of all individual parts in JMAG-designer. The density of the material and the stack length of the motors were known so the weight could be calculated. For the winding, the end winding length also had to be considered. The total length of the windings was determined by looking at the ratio between the stator resistance with stack length 0 mm and the stack length of the actual design. At stack length 0 mm the stator resistance consist only of the end windings and since the resistance is proportional to the length of the windings the total length can be determined. When the volume of all the materials was known the weights could be calculated.

6

Drive System Design

To optimize the performance of the drive system for the SynRM, some aspects needs certain design considerations. Figure 6.1 illustrates an overview of this system. In section 6.1-6.4.6 the implementation of the drive system will be explained and solutions for modelling the system in the Simulink and Simscape environment are suggested. Litterature will here be reviewed to find already existing knowledge relevant for improving the performance of the drive system. The specific SynRM model implementation will be presented in 6.4.5. In section 6.5 attempts are made to evaluate the performance and power losses of the inverter, partly in comparison with a IPM-equivalent and a PMaSynRM-equivalent load.

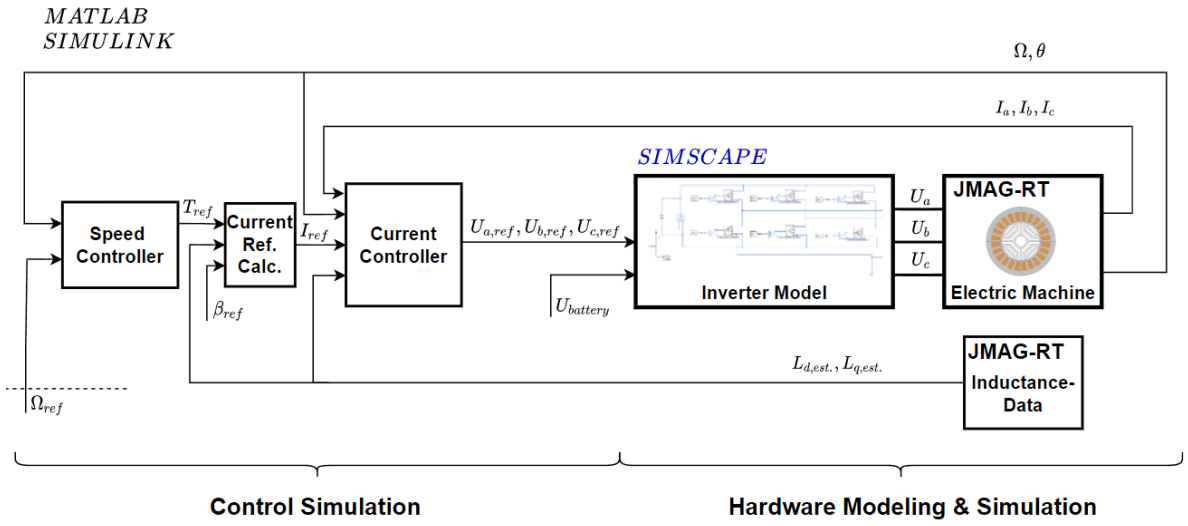

Figure 6.1: Overview of the complete drive system, similar as implemented in Simulink

6.1 Control system

In the inner control loop, a control sequence starts at the Current Ref. Calc. block. Here i_d and i_q are defined and set as the reference for the PI-regulator. The governing equation for this is (2.30), described in section 2.3.1. This can then be solved for the current magnitude,

$$I_{mag} = \sqrt{\frac{2T_e}{3n_p(L_d - L_q)cos(\beta_c)sin(\beta_c)}} \tag{6.1}$$

where trigonometric identities and the angle β_c are used to determine i_d and i_q. The optimal β_c-angle is defined beforehand, either by using an analytical MTPA-method or

by using information from the motor model from JMAG-designer. First, the MTPA option was tested. Optimal torque per ampere for the SynRM yields $\beta_{MTPA} = 45°$. But in JMAG-designer it was found that a higher β_c, gave higher torque output for a given current magnitude. This angle was finally used to control the motor at speeds up to the base speed.

At this point, some assumptions need to be clarified. For the SynRM, and by the model definitions in this work, L_d is bigger than L_q. Then looking at the torque equation, the difference $L_d - L_q$ will be positive. And thus, for a positive torque, i_d and i_q must be positive. Thereby, the current vector will have to be placed in the first quadrant, $\beta_c = [0, 90]$.

A PI-controller with the calculated i_q and i_d as references was implemented. It calculates the error by comparing the reference current with measured currents from the motor phases. The phase currents are first transferred from the 3-phase quantity to the alfa-beta plane with the Clarke transform. It is then transferred with the Park transform to move to a rotating system and to be able to treat the quantities as DC components. The electrical angle (θ) is used in the Park transform, where $\theta = n_p\Theta$ and Θ is the mechanical rotor position. The rotor position was at this point assumed to be a measured quantity.

At the output of the regulator, the voltage was limited to $U_{lim} = V_{DC}$, where U_{lim} is the absolute magnitude in dq. In a real application, U_{lim} is set to protect the inverter hardware, the controller must not under any circumstances request a voltage that can damage the inverter. In this system, it was assumed that the battery voltage is the limiting factor, and requesting higher values than this might instead create an error in calculating the duty cycle. In either case, setting a limiter at the regulator output was regarded as a good engineering practice. However, this limit could lead to an additional problem, where the integrator in the regulator accumulates an error which due to the limit can not be canceled out and the integrator gain value approaches infinity. Furthermore, the complete drive system, including the motor is current limited, and the limit in current can also be regarded as a reason for getting the integrator overcharged. To be precise, it is the regulator error in the current comparison (e) that leads to the overcharged integrator. This was avoided by an anti-windup function, the modified PI-regulator is presented in figure 6.2. The limited value and the unlimited value of the voltage at the output of the inverter are compared and if there is a difference this creates an error ($\bar{e}$), that is first multiplied with the gain $H = 1/k_{ic}$ and then subtracted to the initial integrator part.

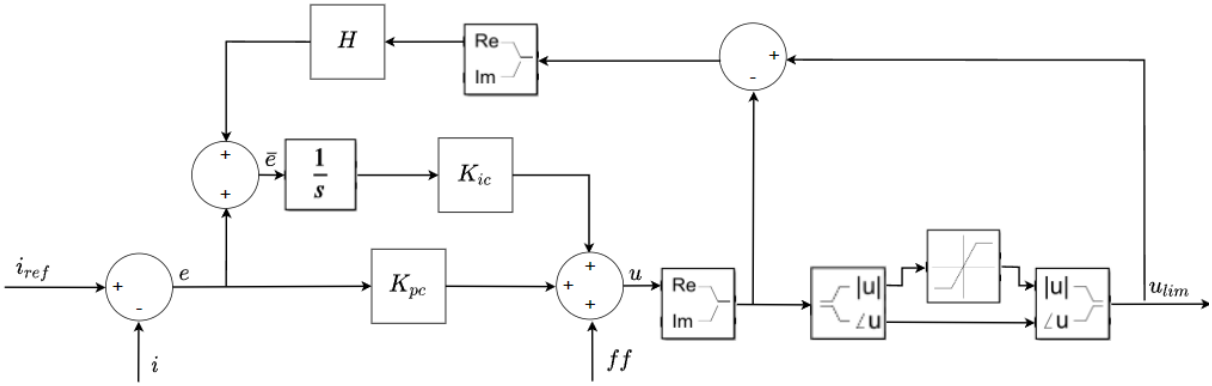

Figure 6.2: Modified PI-regulator with anti-windup of the integrator

6.2 Switch modulation

The limited reference voltage was transformed back to 3-phase quantities and now referred to as $U_{a,ref}$, $U_{b,ref}$ and $U_{c,ref}$. Each reference was then used to calculate the duty cycle, which can be seen as a scaled reference voltage. In the initial setup, (2.54) was used to calculate the duty cycle. The process of calculating the switching states then follows. In Simulink, each duty cycle signal is subtracted by the triangle wave signal, and the difference is fed to a switch block, switching to 1 if the difference is greater or equal to zero, otherwise switching to zero. This means that the PWM is high when the duty cycle is greater than the triangle wave. The implementation of the NOT-gate, explained in section 2.5.3, was found to be best realized by two relation operators, followed by a data type conversion. This stage is illustrated in figure 6.3b, and the related signal formation is illustrated in figure 6.3a.

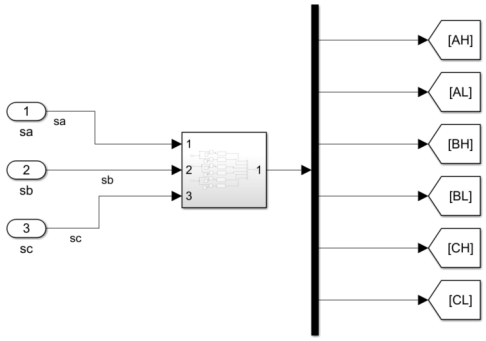

(a) Overview of the formation of the Gate driver signals

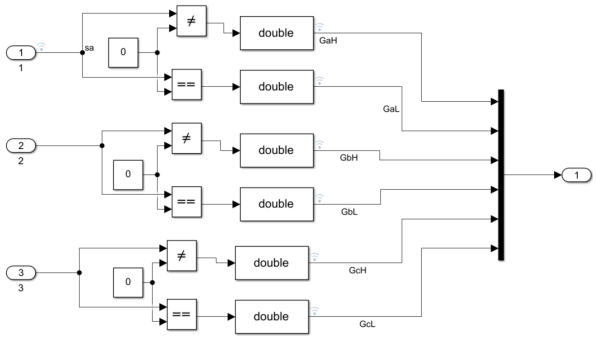

(b) Logic handling between the switching states and the Gate driver level

Figure 6.3: Switching states to Gate driver signals

6.3 Speed control

A speed controller was then added as an outer control loop and implemented as a PI-controller. As was discussed in section 2.5.1, the two main parameters that need to

be known for the motor were the inertia constant J and the friction coefficient D. An assumption was made that the inertia of the rotor could be modeled as moment of inertia of a cylindrical object

$$J = \frac{m_{rotor} R_{rotor}^2}{2} \tag{6.2}$$

where m_{rotor} is the mass of the rotor. To determine the friction coefficient accurately, measurement needs to be made on a physical motor. In this project ,the assumption was made that at ω_n, $T_{fric} = 0.027$ p.u. This resulted in a $D = 0.1$ mNm/rad.

When controlling the motor at speeds above ω_n operation in field weakening was used. As a starting point, a β_{FW} for ω_{max} and maximum current was sought. Equation (2.53) was used and $\beta_{FW} = 68.4°$ was found. But similar to β_{MTPA}, the actual motor design and information from JMAG-designer gave a bigger β_{FW}. The initial implementation of the Field weakening algorithm was done by simply always setting $\beta_c = \beta_{FW}$ when speed above ω_n was requested.

6.4 Hardware modelling and system improvements

To build the complete system the implementation was done step-wise and several smaller models were built separately, especially for the hardware simulation, this to be able to troubleshoot the model and to find appropriate solver settings in Simulink. Different models related to the hardware modeling are here presented.

6.4.1 Ideal inverter model

The inverter model in the drive system simulations could be simulated in Simulink using six ideal MOSFETs, thereby this model setup is called the ideal model. The ideal MOSFET models the drain-source resistance, R_{DSon}. But it does not model any dynamic behavior and it was assumed that it does not model any switching losses. This ideal inverter model was suitable for validating the modulated switching states and also to validate different switching frequencies. The ideal model is illustrated in figure 6.4.

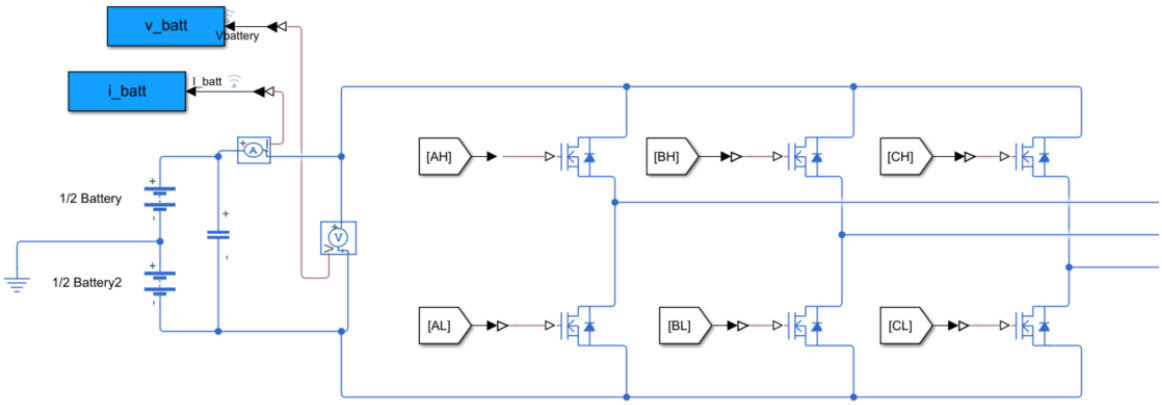

Figure 6.4: Simscape model of an ideal inverter

As a starting point, the internal battery resistance was set to a low value and the capacitor was modelled with a high value to reduce the DC ripple below 0.1 V.

6.4.2 SPICE imported MOSFETs and the non-ideal inverter model

The non-ideal inverter model is based on MOSFETs that are parameterized in the SPICE programming language and then imported to the Simscape environment. The MOSFETs model a more complete behavior compared to the ideal MOSFETs, including dynamics, and are also capable of calculating the junction temperature. The actual hardware corresponding MOSFETs that are parameterized comes from the Infineon Optimos serie. The MOSFET requires a simscape gate driver block and some overall considerations to work properly. An overview of this inverter model is presented in figure 6.5.

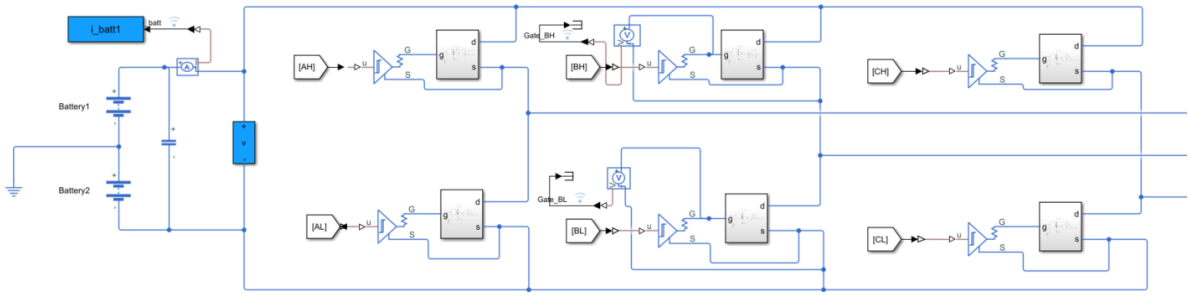

Figure 6.5: Inverter model with SPICE-imported MOSFETs

The gate driver block simulates a total turn-on time by two instances, a propagation delay and a rise time. The instances were matched by the dynamics explained in 2.5.4 and specified by the Infineon data-sheet for the Optimos IPB100N12S3-05, see appendix A.4. To test this dynamic, a single Gate driver and a MOSFET block was tested alone. The MOSFET block is illustrated in figure 6.6.

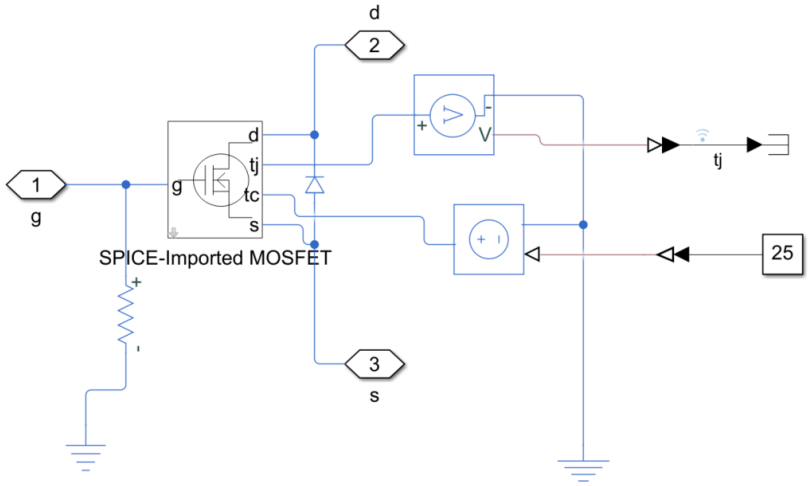

Figure 6.6: MOSFET implementation with the connected signals

The dynamics are also affected by a 10 nC capacitance, set as default in this gate driver design block. The Gate driver voltage is plotted in figure 6.7. What was aimed here was mainly the desired delay to avoid shoot-through in the inverter and an increase in U_{GS} to a value close to 5.5 V. Above this value, the MOSFET is expected to conduct with a resistance of $R_{DS} = 6.0\ m\Omega$, or lower. Which was approximated after looking into the datasheet and extracting the slope of the I_D-V_{DS} curve. A voltage spike when the voltage is initiated can also be noted. As well as some oscillations and a settling time to reach a final value.

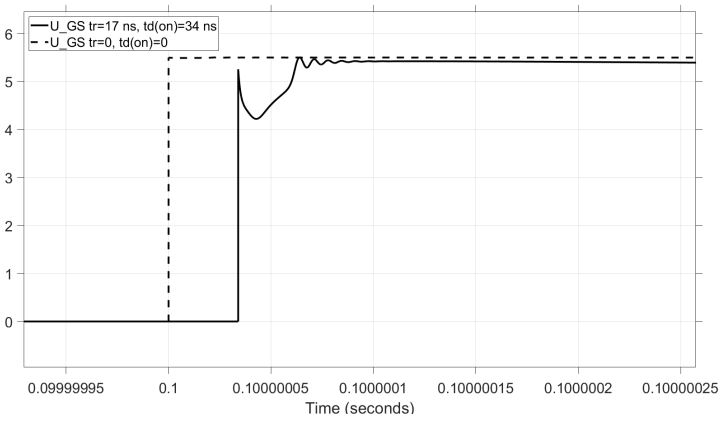

Figure 6.7: Comparision of gate driver voltage with no delay and the selected delay

The thermal dynamics are in SPICE modeled by voltages, as described in [32]. It is similarly implemented in Simscape. As can be seen in figure 6.6, the case temperature was here set to 25°C and the developed junction temperature could be sampled and stored. Since the junction temperature is dynamic, the resistance, R_{DS} will also be dynamic.

6.4.3 Zero sequence injection

For calculating the duty cycle and defining the switching state, the theory in section 2.5.3 was again recalled. It was known that this utilizes 50% of the DC-link voltage,

$$U_{x,max} = \frac{V_{dc}}{2} \tag{6.3}$$

To increase the performance of the drive system, alternative calculations of the duty cycle can be used. A general modulation idea is described by the Space Vector Pulse Width Modulation (SVPWM), where the six switching states can all be described by a common space vector, early explained by [33]. It is known that in this way of modulating, the zero vector (or zero sequence) can be included, referring to the two additional switching states that represent the instances where the line-to-line voltages are zero.

When those ideas were established, the zero sequence was used to enable an alternative duty cycle calculation, which gives similar results as the third harmonic injection. The third harmonics injection however needs additional calculations, not always suitable in a real motor drive application [34]. In this alternative then, a zero sequence shift, z_0

was added to each duty cycle and the z_0 is defined as

$$z_0 = \frac{min(d_a, d_b, d_c) + max(d_a, d_b, d_c)}{2} \tag{6.4}$$

This is known to be an efficient method to increase the performance, approximately 15% more of the DC-link voltage can be utilized, here

$$U_{x,max} = \frac{V_{dc}}{\sqrt{3}} \tag{6.5}$$

Litterature indicates that this method is well established and due to relatively low computational costs it is also suitable in microprocessor-controlled motor drives [34]. The initial duty cycle versus the duty cycle with zero sequence injection is illustrated in figure 6.8. The resulting currents at the load are plotted in figure 6.9 to illustrate the performance gain.

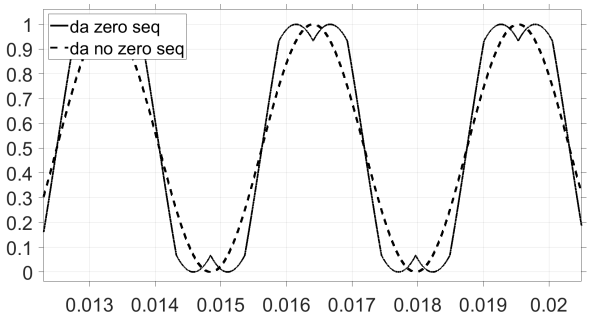

Figure 6.8: Calculated duty cycle, da, with and without zero sequence injection.

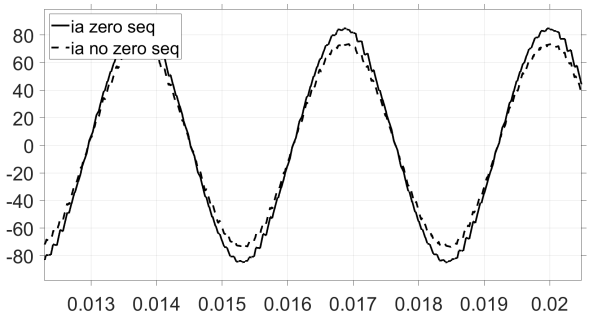

Figure 6.9: Load current with an RL-load, with the two different voltage excitations.

This emphasizes that with the same load it is possible to have a higher power output. However in a motor drive application, the desired working point should not be shifted when implementing a modified duty cycle, but what is implied is that the modified duty cycle gives the possibility to utilize a higher voltage from the battery.

For a sinusoidal space vector PWM, the modulation ratio can be kept below or equal to 1. This is also true when using zero sequence injection. To have $M \leq 1$ and thus to avoid over modulation, is known to avoid certain harmonics and to lower the Total Harmonics Distortion, THD [35], [36]. For that reason, over-modulation was in this work not used. But the THD is also affected by the switching frequency, f_{sw}. THD typically decrease linear with a increasing f_{sw} [36].

6.4.4 Switching frequency

The selection of the switching frequency does not only affect the switching losses. Lower switching frequencies and the lower order harmonics, both in the range of a couple of kHz, give an acoustical noise than can be annoying to the ear. In this range, the additional torque ripple is more considerable. At higher switching frequencies, at a couple of tens kHz, problems from electromagnetic interference arise while the audible noise and the

additional torque ripple decrease or disappear [10]. Three different frequencies, 5 kHz, 20 kHz, and 50 kHz were simulated to analyze the results in terms of THD, motor torque ripple, and switching losses.

6.4.5 JMAG imported SynRM model

Each specific motor design made in JMAG could be imported into Simulink by the generated RT-file, corresponding RT-block, and the support files, all from JMAG-RT. Early implementations of this function used Simulink signals as inputs and outports. But later versions used Simscape signals to model each phase line connected to the block. A Simscape signal represent a more complete implementation of a physical property. In the case of Simscape electrical (represented by blue lines) a signal models both current and voltage, usually driven by a current source. In this implementation, the Simscape electrical signal was useful since it also simulates a voltage drop over the inverter and the battery. It should be noted that the RT-block was implemented in Simscape Specialized Power Systems which requires signal conversion from Simscape Electrical (the lines are again black after the conversion, but should not be confused with the black simulink lines). The block used for this conversion acts as a voltage source in the Specialized Power Systems side and as a current source on the Simscape side, each referred to the electrical ground on the respective sides. Figure 6.10 illustrate the motor block and the 3 phase voltages switched by the inverter are labeled A, B, C.

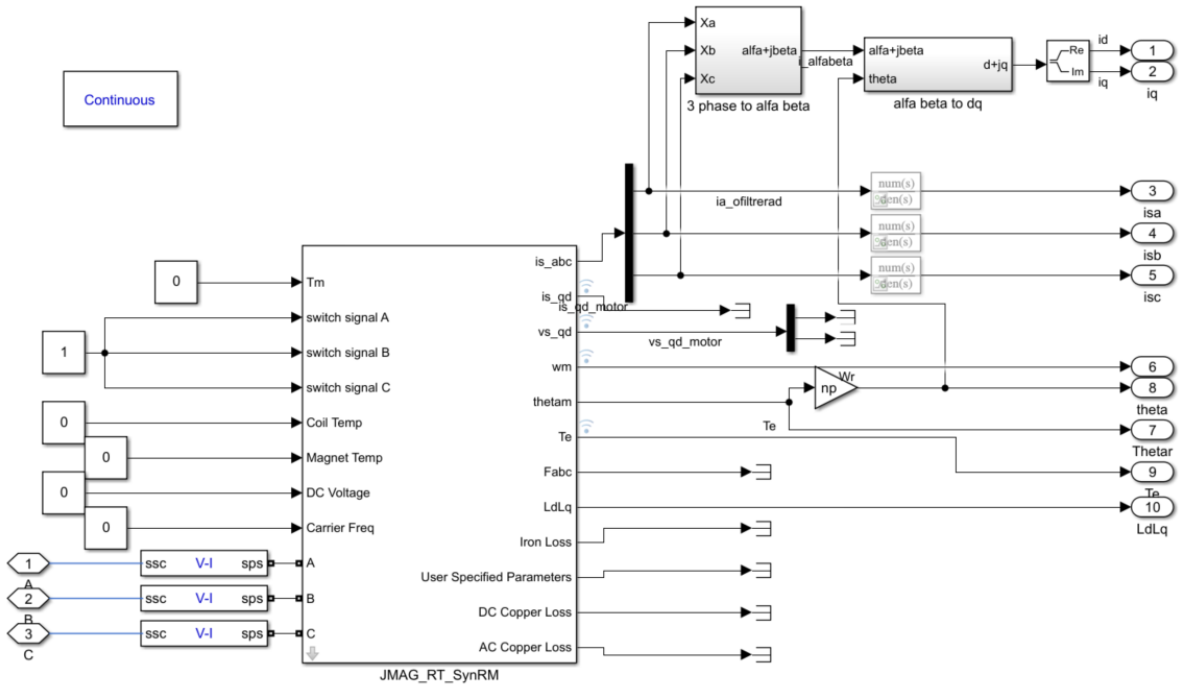

Figure 6.10: RT motor-model imported from JMAG-RT and implemented in the specific Simulink environment

6.4.6 Model and control with non-linear inductance

As was mentioned in section 2.3.1, L_d and L_q have non-linear behavior and are dependent on i_d and i_q. The torque equation for the SynRM, (2.15), indicates that the machine torque is highly dependent on changes in L_d and L_q. The control of the machine was thereby also very sensitive to those changes and using fixed values gave a sub-optimal control. Furthermore, the regulator parameters for the current controller are also dependent on inductance values. To handle this, the data determined in the mapping of the SynRM were used to create a look-up table. The data was mapped in terms of L_d and L_q, both depend on I_{mag} and β_c. The current and angle vector was used together with the corresponding data in a simulink look-up table, see figure 6.11, to update the inductance parameters before each control iteration. The control parameters are then updated depending on the values according to (2.41), (2.42) and (2.43).

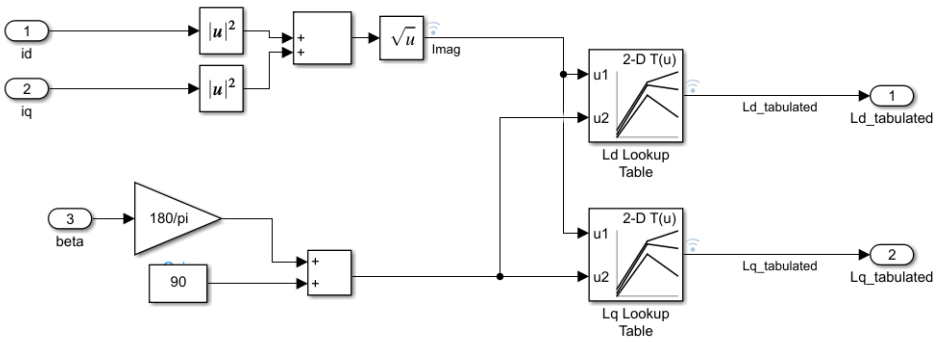

Figure 6.11: Look-up tables for L_d and L_q

It was found that the current angle needed to be shifted from the first quadrant to the second to extract the correct inductance values from the look-up table. This is because of different axes definitions in JMAG-RT.

6.5 Performance Analysis

The drive performance was analyzed from different perspectives and with different parts in focus. Figure 6.12 overviews the different simulations that were performed and which hardware is considered.

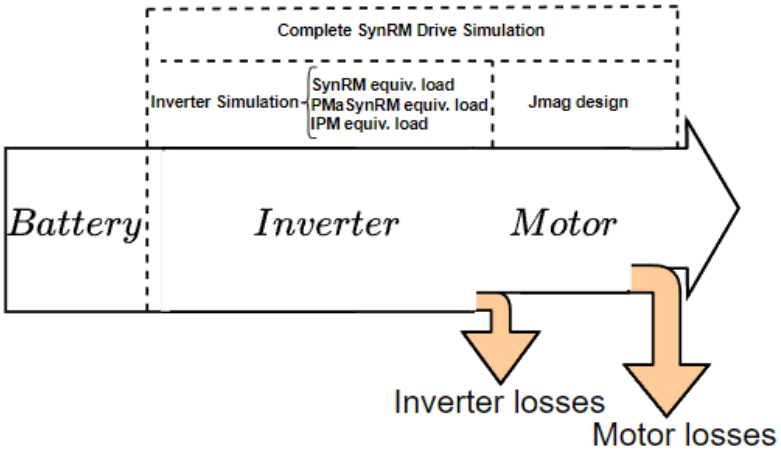

Figure 6.12: Illustration of the setup for the performance analysis

All simulations include the battery, but since the battery was simulated as close to an ideal voltage source with no losses it is not highlighted in this analysis.

6.5.1 Complete SynRM Drive Simulation

The model used for simulating the complete drive system is overviewed in figure 6.13. The power electronics and machine was implemented in simscape in accordance with section 6.4.5 and 6.4.1. The control system is simulated in simulink as described in 6.1.

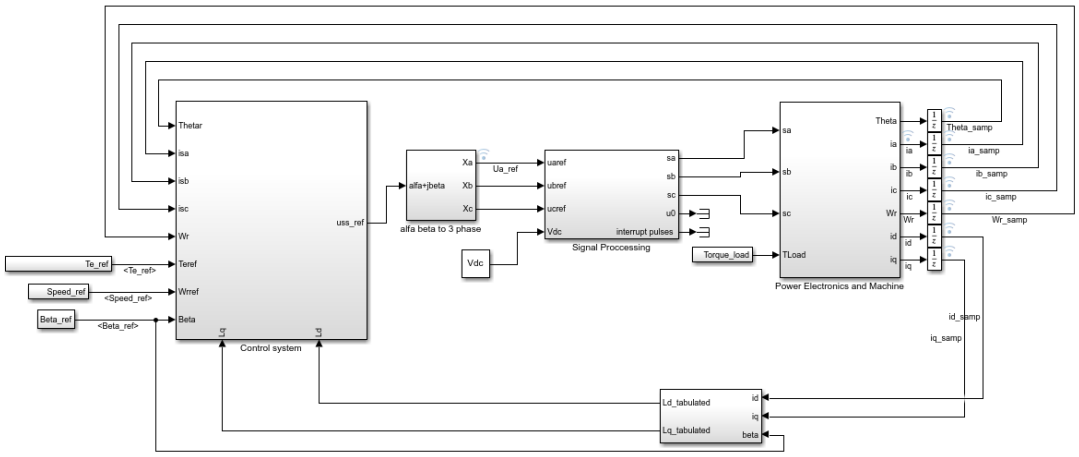

Figure 6.13: Setup for the complete SynRM drive simulation

The current controller with torque reference as input was tested with a step function. To solve the motor model the rotor speed must not spin freely, because the imported model is not defined for speeds significantly larger than the max speed. Setting the friction coefficient to 1000 times the normal values would simulate a speed-dependent brake. When the current controller was to verify the torque estimation, an RT-block that uses measured voltages represented in Simulink was used instead of the actual physical voltages implemented in Simscape. The idea was to highlight the current and torque behavior as a function of the inductance. Which is the core of the control loop. When using the speed

controller, however, a more complete representation of the system was aimed and the motor was connected with Simscape signals and the added friction brake was removed. Instead, an external mechanical load T_{ext} was added to let the motor produce the desired torque at the requested speed.

6.5.2 The equivalent RL load

To ease the simulation process a set of simulations was done with an RL-equivalent load. Here, a resistance was connected in series with an inductance, this load was then y-connected. The RL-equivalent load was implemented mainly due to a reoccurring error in the motor implementation, arising from the interface block between Simscape Electrical and Simspace Specialized Power Systems. The error was only present when the SPICE imported MOSFETs and thus the non-ideal inverter was used. In those models, the solver would end up in states (possibly at transients) that it can not solve.

The RL-equivalent load was calculated from power factors that were derived from the three motor models, the SynRM, the IPM motor, and the PMaSynRM. Then using the base speed and the torque of $T_{em} = 1$ p.u. as the operating point for each motor. Due to the different PF for the different motors, the equivalent R and L were different. The purpose was to analyze the losses dissipated as a result of the different PF.

The setup and calculation for the RL-equivalent load was calculated by using information from the motor model. The specific voltage and current for each motor was used to calculate the corresponding apparent power. The PF was then used to find the active power, P, and reactive power, Q. Finally the electrical frequency (f) was derived from the rotor speed. The phase resistance, R_{load} and the phase inductance, L_{load} then follows as

$$R_{load} = \frac{P}{I_{rms}^2} \tag{6.6}$$

$$L_{load} = \frac{\frac{Q}{I_{rms}^2}}{2\pi f} \tag{6.7}$$

6.5.3 Power losses using FFT analysis

The main idea behind finding the power loss, P_{loss}, and the efficiency in the inverter was to compare the power output directly after the battery, labeled P_{batt}, and the power output from the inverter, P_{inv}. For P_{inv}, some further consequences were noted. First, the switched voltage from the inverter was difficult to measure in the time frame, secondly, it is only or mainly the fundamental component of the voltage that is useful for the motor, thus only the fundamental component was taken into account when analyzing the useful inverter power output. For the load current after the inverter it was also the fundamental component that was regarded.

The FFT analysis was used through a GUI, labeled powergui in Simulink. Initially, a script in Matlab using related libraries was used. The results from the Matlab script had dependencies on resolution and the number of periods of the signal, but the GUI tool was

consistent and regarded as a more accurate solution. The selected motor speed yielded the frequency of the fundamental component and the magnitude for this component was used. An example of an analyzed voltage in the GUI is presented in figure 6.14. For each simulation, the apparent power can be calculated. For both the voltage and the current, the angle could be read out from the GUI. The phase angle, φ, can be calculated following section 2.3.2. This angle was then used to calculate the actual power, P_{inv}. The current from the battery was not constant, it had a high ripple. The best way to analyze this was to use the DC-component tool in the GUI. Thus, both of the measured components from the battery are regarded as DC components and the active power, P_{batt} could be calculated. Finally, the power loss $P_{l,inv,sim}$ was calculated as

$$P_{l,inv,sim} = P_{batt} - P_{inv} \tag{6.8}$$

and the simulated efficiency of the inverter, $\eta_{inv,sim}$ is here defined as

$$\eta_{inv,sim} = \frac{P_{inv}}{P_{batt}} \tag{6.9}$$

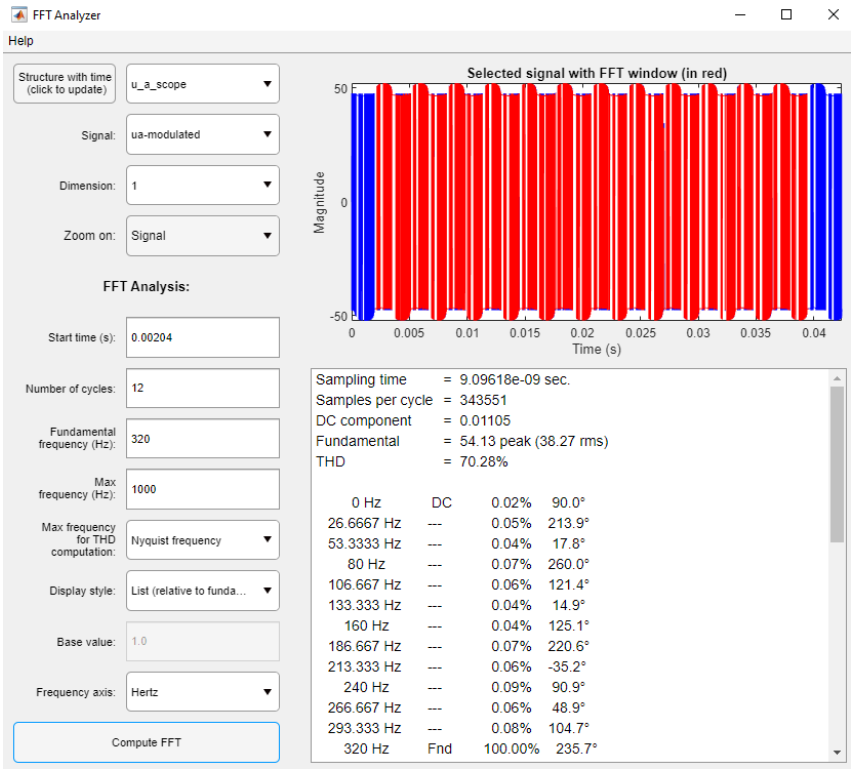

Figure 6.14: Example of an FFT-analysis in the Simulink GUI

6.5.4 Power losses from theoretical calculations

To analyze the power losses in the inverter further, the conduction and switching losses were calculated for each MOSFET with considerations taken for the inverter application [18]. To then form a model for the total inverter losses. Several assumptions were made for this model. The case for comparison was the SynRM equivalent load with the SPICE

model inverter. The inverter output current (here I_s) was assumed to be a pure sinusoidal current with amplitude presented by the simulated result. The supply voltage was simply put as the DC link voltage, $U_{DD} = U_{batt}$. The resistance in the diode is assumed to be the same as in the MOSFET and the temperature was assumed to be fixed 25° C.

For analyzing the switching losses in an inverter application, the current in each half-bridge inverter leg is simplified. This is in each half-wave of the output sine wave, $(1/(2f))$, simplified as a DC component

$$I_{DC} = \frac{1}{\pi} I_{s,peak} \tag{6.10}$$

Each switch cycle can then be explained by the theory in section 2.5.4.

6.6 Inverter component validation

To validate the inverter models and to support upcoming work a short study was suggested on selecting or validating hardware components. The hardware component that has been in focus in the drive analysis was mainly the MOSFETs.

The procedure to validate if a MOSFET is suitable for the application and the load was done according to the following screening,

1. Is the maximum voltage rating of the MOSFET below the maximum voltage of the system?
2. Is the total power losses in each MOSFET below the value of maximum power dissipation stated for the MOSFET?
3. Is the MOSFET operating within the safe operation area?
4. Find the better performance in terms of lower R_{DS} or lower rise- & fall-times.

The maximum voltage rating refers to the absolute maximum voltage rating. Transients must also be lower than the maximum MOSFET rating to not risk damaging the MOSFET. All the upper limits for operating points should be covered by the curve describing the safe operation area, found in the MOSFET datasheet, see appendix A.4. Besides the breakdown voltage, the curve also considers a segment for the maximum dissipation power, a region for temperature stability, and an upper limit for continuous current [19]. This means that the safe operation area would cover all aspects mentioned in this validation. It was however decided to also validate the power dissipation alone and to use the simulated data to give more depth to the validation. It should however be noted that at increasing voltages, the curve of maximum power dissipation intersects with the curve of thermal stability. Because of this, the maximum limits of power dissipation should be used carefully to avoid a thermal runaway. Again, the safe operating area should be used for a final conclusion. The validation was closely tied to the work in simulating the inverter, and the MOSFET models available for the simulations were the basis of this analysis.

The maximum power dissipated in one MOSFET device was assumed to be the same as the power dissipated in one phase and thus also assumed to be a third of the total inverter losses. The reason for assuming that the loss is dissipated by only one of the

MOSFETs in the inverter leg is for accounting for all possible switching states. Furthermore, to avoid errors in calculating a possible split between the power loss of the two MOSFETS, a phase maximum was used for the sake of redundancy. For selecting pulse width for the safe operation area, the nominal switch period for one MOSFET, $(1/f_{sw})$ was used. And when validating the limit of thermal stability, the peak phase current was used.

The MOSFET would need some type of cooling. In the above reasoning, the cooling performance is not considered. To make a more in-depth analysis of the power dissipation and the operating temperature, an analysis can be done using a typical thermal model and data on thermal characteristics taken from the corresponding datasheet.

7
Results

7.1 SynRM

Here the results of the SynRM analysis will be presented for both design concepts. The results for the PMaSynRM will also be presented. Some decisions based on the results are explained throughout the design process.

7.1.1 Design 1

For the first design, using JMAG Designer, the maximum torque angle was found to be around 67.5° when the d-axis was aligned with the a-phase. Meaning that the maximum torque angle was a lot larger than that of the MTPA angle at 45° indicating that the steel was quite saturated.

7.1.1.1 Base design

The baseline parameters are presented in the table 7.1 along with the PF, torque, torque ripple, efficiency, and voltage needed to maintain the base speed. All performance parameters are presented for all future cases for both designs.

Table 7.1: Initial parameters SynRM design 1

Performance Parameter	**Value**
Torque	0.998 [p.u.]
Torque ripple	13.8%
Efficiency	87.0%
PF	0.585
Phase Voltage RMS	41.44 [V]
Design variables	
β_s	4.5°
K_{wq}	0.7
$W_{q,1}$	1.65 [mm]
$W_{q,2}$	1.65 [mm]
$W_{q,3}$	1.65 [mm]
$W_{q,4}$	1.65 [mm]

7.1.1.2 Change of rotor displacement angle

The size of the barriers is kept constant while β_s is varied between 0° and 10°. The results are presented in figure 7.1.

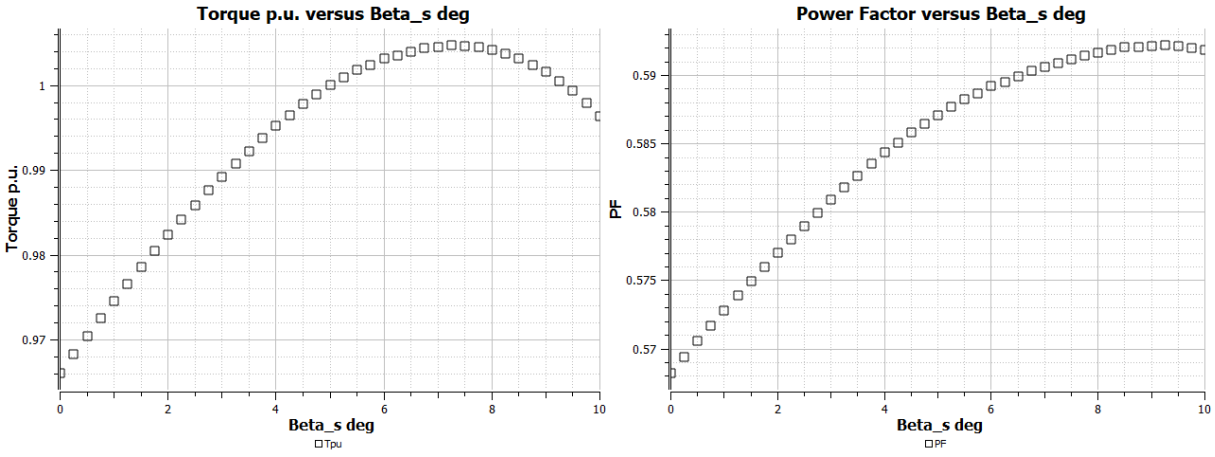

(a) Torque

(b) PF

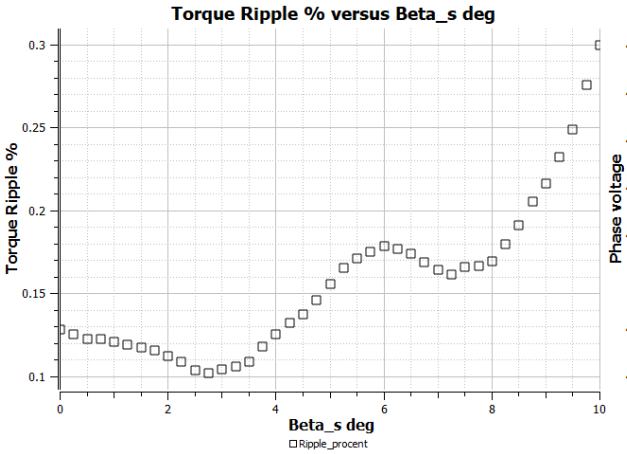

(c) Torque ripple

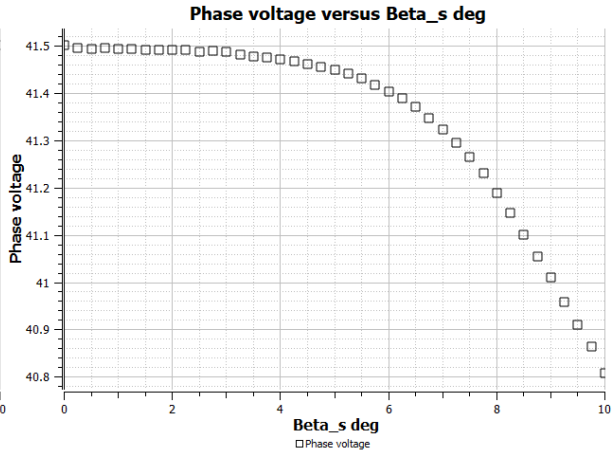

(d) Voltage

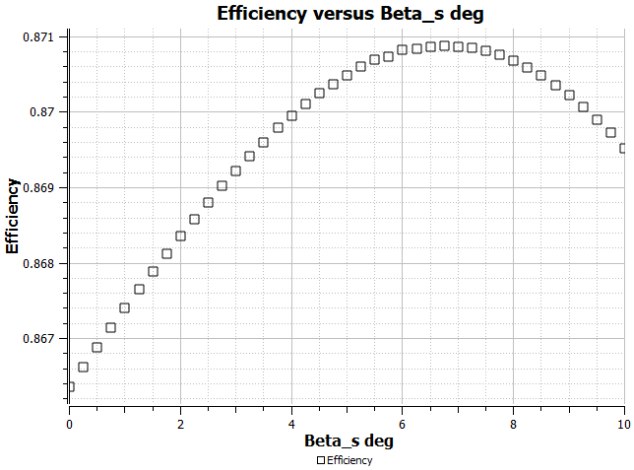

(e) Efficiency

Figure 7.1: Performance results for design 1 when changing β_s

The torque changes when adjusting β_s. β_s gives the lowest torque ripple at 2.75° and since the goal with β_s is decrease the torque ripple this was used as the parameter value for β_s.

7.1.1.3 Insulation Ratio

With β_s set, the insulation ratio along the q-axis was varied by changing the size of the barriers. In figure 7.2 the insulation ratios effect on the performance is presented.

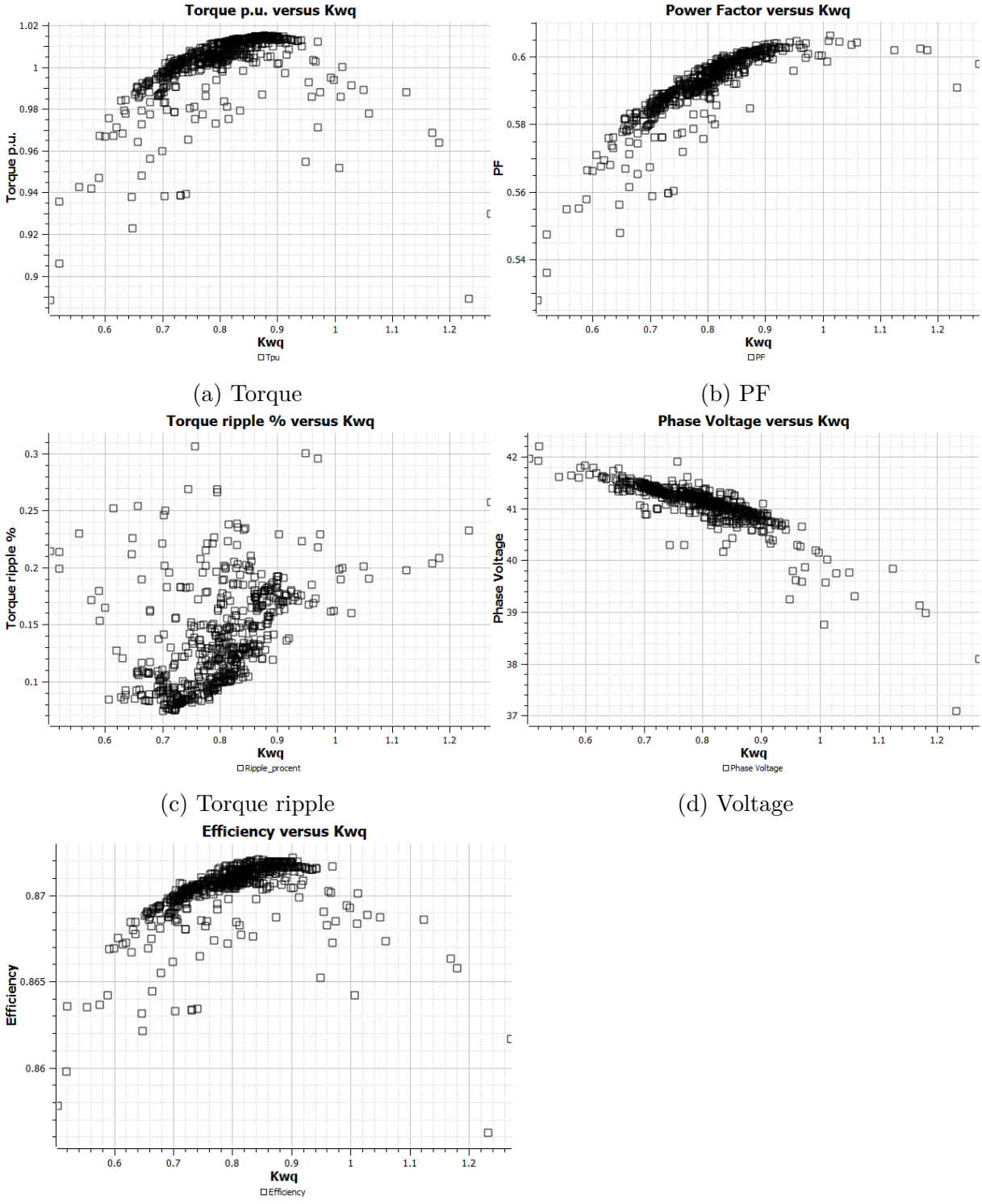

(a) Torque

(b) PF

(c) Torque ripple

(d) Voltage

(e) Efficiency

Figure 7.2: Performance results for design 1 when changing the the insulation ratio K_{wq}

In figure 7.2a it is seen that the torque is maximized for an insulation ratio between 0.7 and 0.9. The same correlation can be seen for the power factor and efficiency as well. The torque ripple is however better for slightly smaller values of insulation ratios, around 0.7. The solution converges to the case presented in table 7.2

Table 7.2: Final parameters SynRM design 1

Performance Parameter	**Value**
Torque	1.01 [p.u]
Torque ripple	8.4%
Efficiency	87.1%
PF	0.59
Phase Voltage RMS	41.21 [V]
Design variables	
β_s	2.75°
K_{wq}	0.78
$W_{q,1}$	1.65 [mm]
$W_{q,2}$	1.82 [mm]
$W_{q,3}$	2.02 [mm]
$W_{q,4}$	1.55 [mm]

7.1.2 Design 2

Here the results of the second design approach will be presented. The maximum torque angle was essentially the same as in design 1 at 67.5° when the d-axis was aligned with the a-phase. This was expected since the rotor geometries are similar and the fact that the steel was quite saturated.

7.1.2.1 Base design

The base case is presented in the table 7.3

Table 7.3: Base case SynRM design 2

Parameter	K_{wq}	K_{wd}	β_s
Value	0.6	0.7	5.625°

This is the initial parameter selection and the performance result for this case is presented in table 7.4.

Table 7.4: Initial performance parameters for design 2

Performance Parameter	**Value**
Torque	0.99 [p.u]
Torque ripple	27.4%
Efficiency	85.1%
PF	0.57
Phase Voltage RMS	41.87 [V]

7.1.2.2 Change of K_{wq}

The value of K_{wq} is varied between 0.4 to 1.0 with the other values set to the base value, see table 7.5. The result are seen in figure 7.3

Table 7.5: Varying K_{wq} for SynRM design 2

Parameter	K_{wq}	K_{wd}	β_s
Value	0.4-1.0	0.5	5.625°

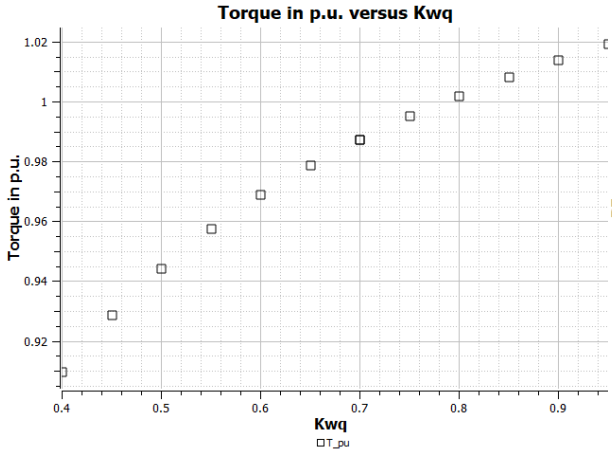

(a) Torque

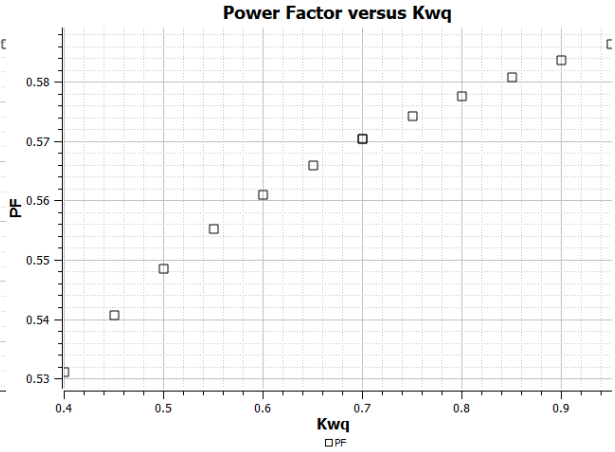

(b) PF

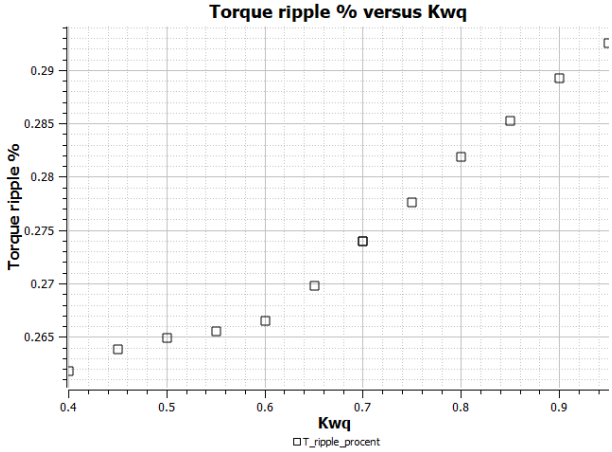

(c) Torque ripple

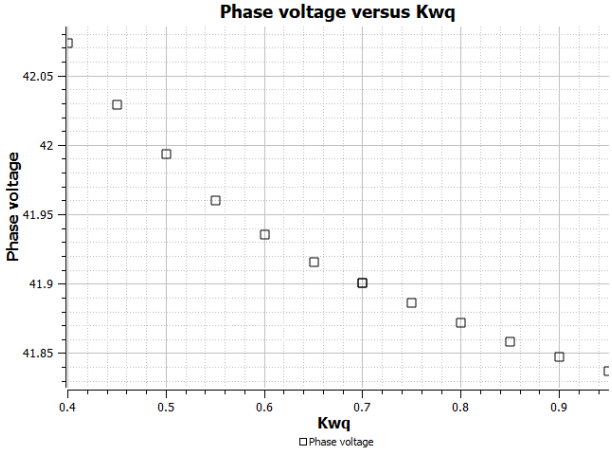

(d) Voltage

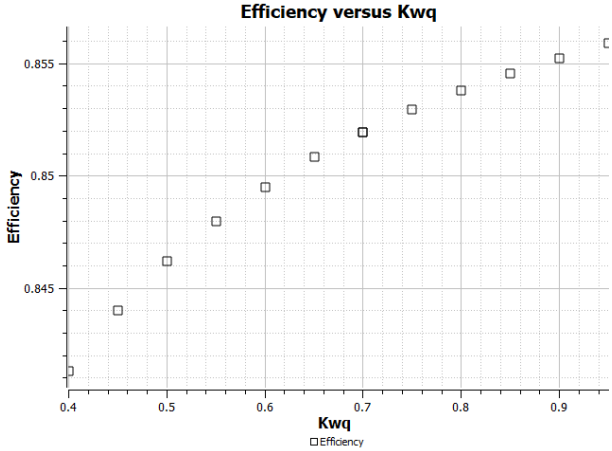

(e) Efficiency

Figure 7.3: Performance results for design 2 when changing k_{wq}

The torque increases with increasing K_{wq}. However, due to conflicting geometries when studying K_{wd}, K_{wq} was limited to 0.85.

7.1.2.3 Change of K_{wd}

With the insulation ration in the q-axis set K_{wd} was changed between 0.5 and 1, see table 7.6 and the results can be seen in figure 7.4

Table 7.6: Varying K_{wd} for SynRM design 2

Parameter	K_{wq}	K_{wd}	β_s
Value	0.85	0.5-1	5.625°

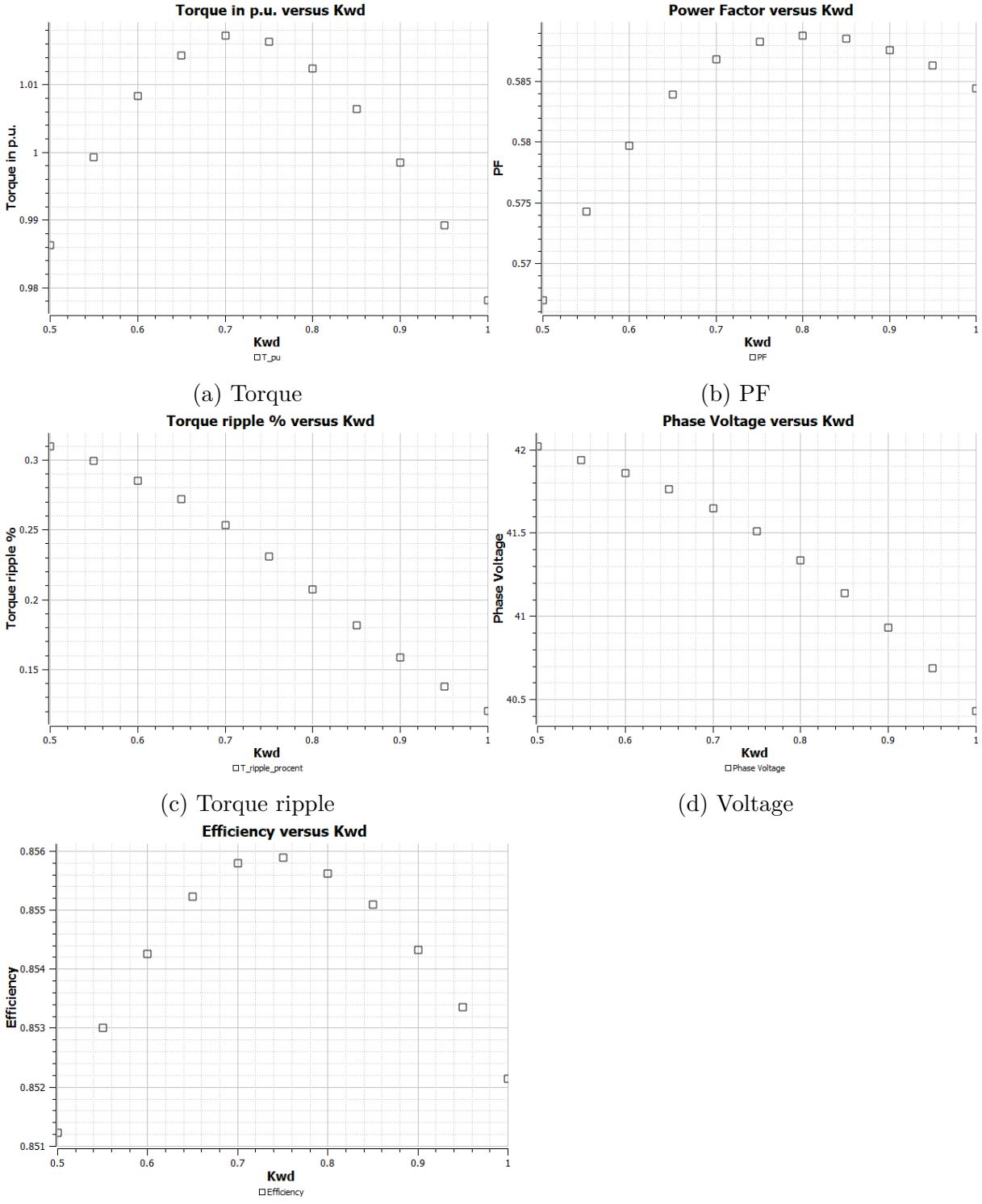

(a) Torque

(b) PF

(c) Torque ripple

(d) Voltage

(e) Efficiency

Figure 7.4: Performance results for design 2 when changing K_{wd}

The torque starts to decrease after the insulation ratio gets higher than 0.7. Therefore the insulation ratio in the d-axis is set to 0.7

7.1.2.4 Change of rotor displacement angle

The insulation ratios are set. The angle β_s is now changed in order to minimize torque ripple. see table 7.7 and the results can be seen in figure 7.5

Table 7.7: Varying K_{wd} for SynRM design 2

Parameter	K_{wq}	K_{wd}	β_s
Value	0.85	0.7	0-12°

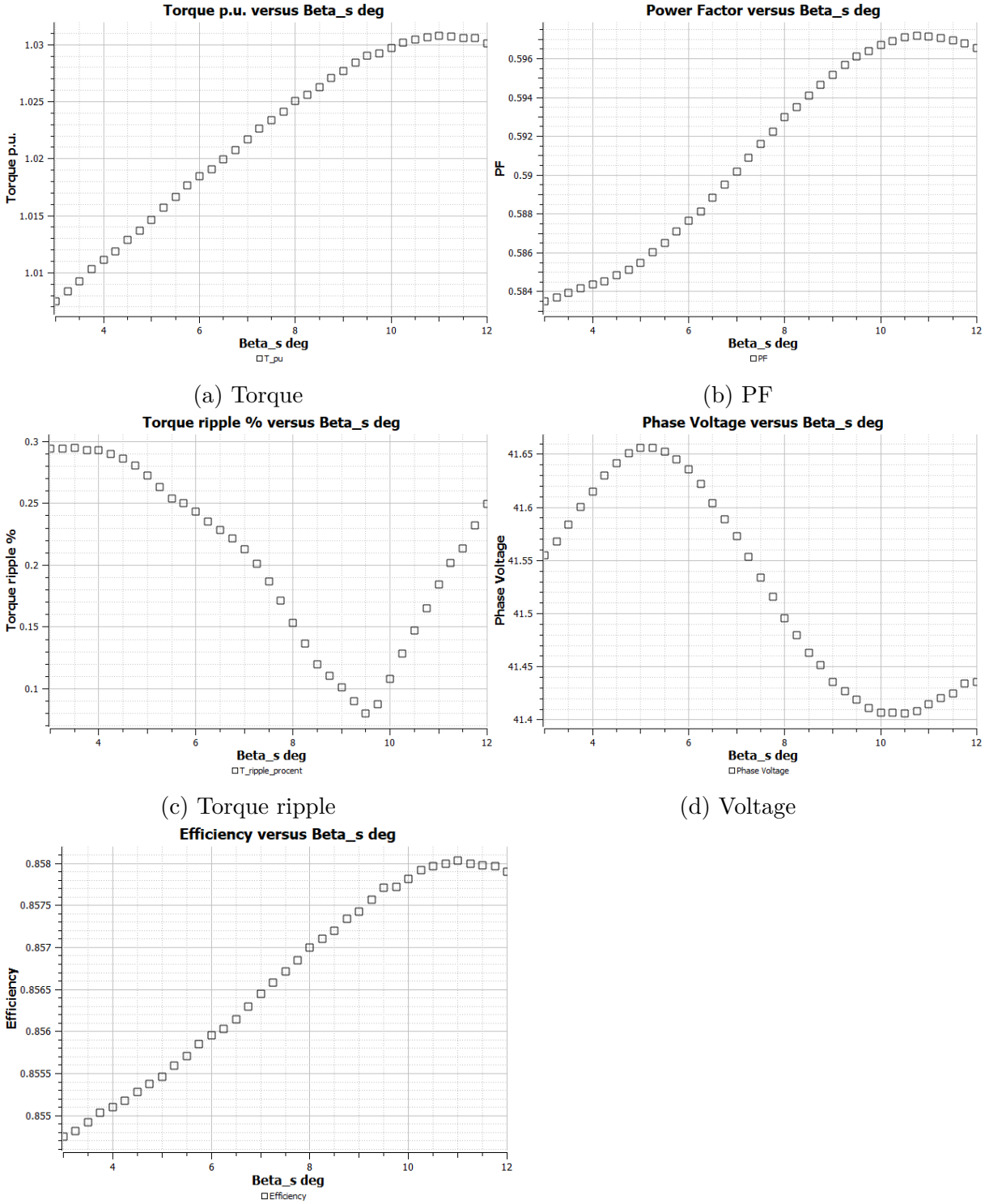

(a) Torque

(b) PF

(c) Torque ripple

(d) Voltage

(e) Efficiency

Figure 7.5: Performance results for design 2 when changing $Beta_s$

The ideal value is found at 9.5° to minimize the torque ripple. The effect on the torque was considered minimal and therefore the angle was not set to a higher value since the gain in torque was considered too low in relation to the increase in torque ripple.

7.1.2.5 Final design parameters for design 2

The final values for the insulation ratios and β_s are presented in table 7.8.

Table 7.8: Final parameters SynRM design 2

Parameter	K_{wq}	K_{wd}	β_s
Value	0.85	0.7	9.5°

A slight modification had to be made to the final rotor of design 2. In figure 7.6 the marked area was removed. This was because the profile was so thin that the distance up into the arms highlighted in the picture cannot be made within realistic manufacturing tolerances.

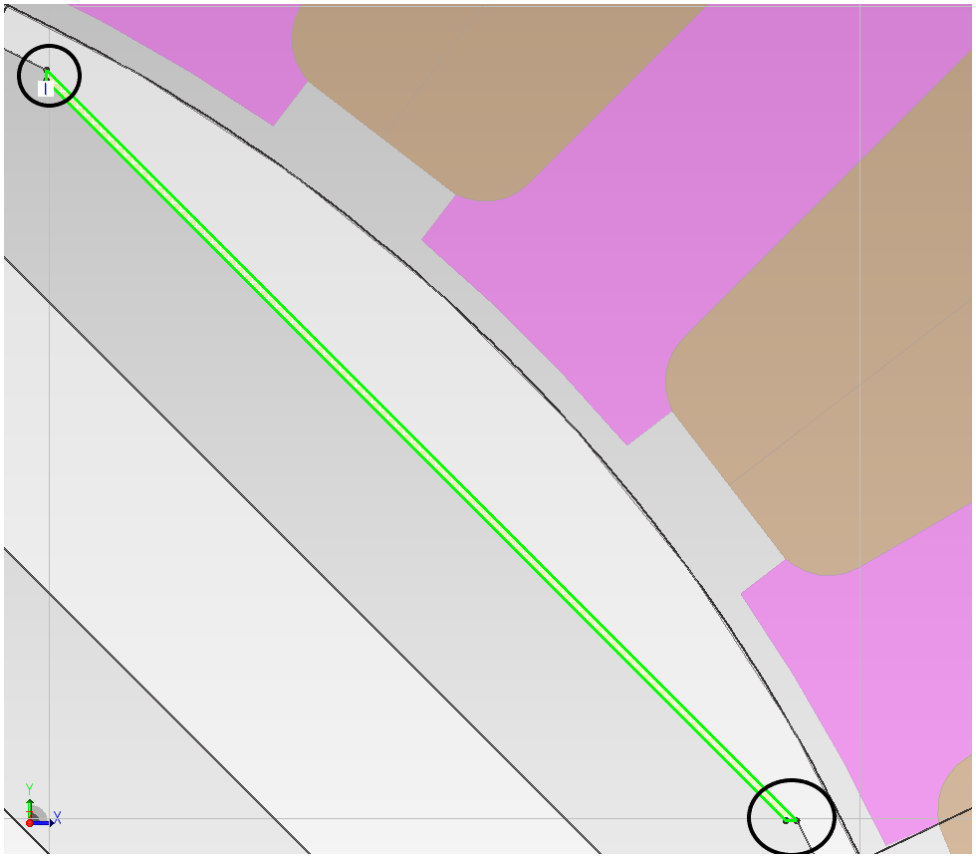

Figure 7.6: Removed area in outer most flux path in Design 2

With the profile removed the performance results are presented in table 7.9

Table 7.9: Performance parameters after parameter sweep and profile removal

Performance Parameter	Value
Torque	1.03 [p.u]
Torque ripple	8.92%
Efficiency	85.8%
PF	0.599
Phase Voltage RMS	41.34 [V]

7.1.3 Result of mechanical analysis

The experienced stress on the rotor lamination for design 1 can be seen in figure 7.7. The load cases are presented individually along with total von Mises stress experienced for the worst case scenario.

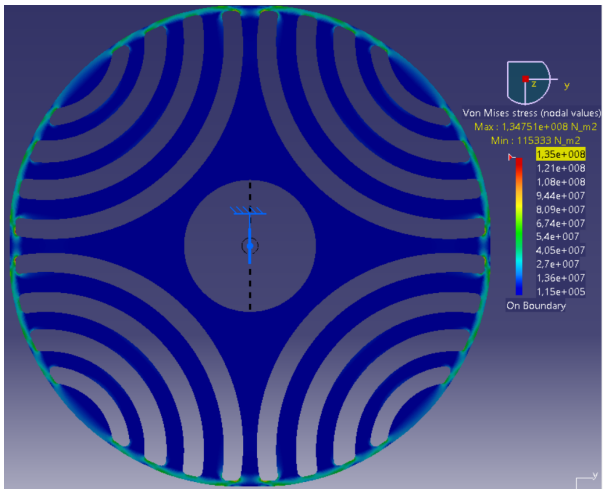

(a) von Mises stress design 1 when rotating at ω_{max}

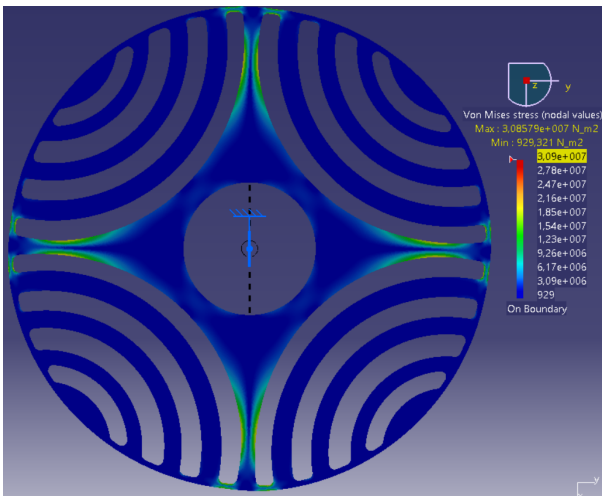

(b) von Mises stress design 1 from deceleration

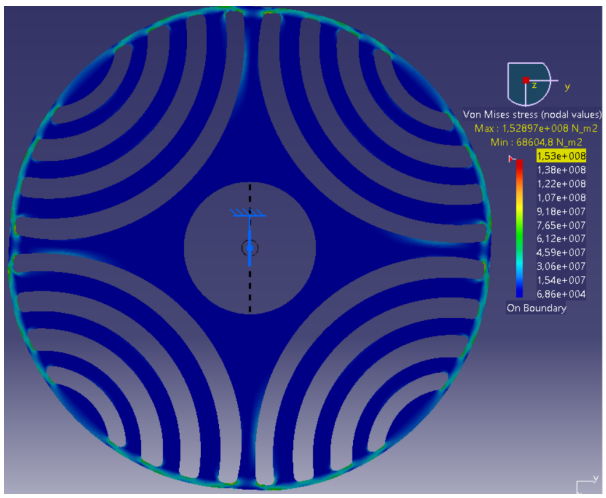

(c) Total von Mises stress design 1

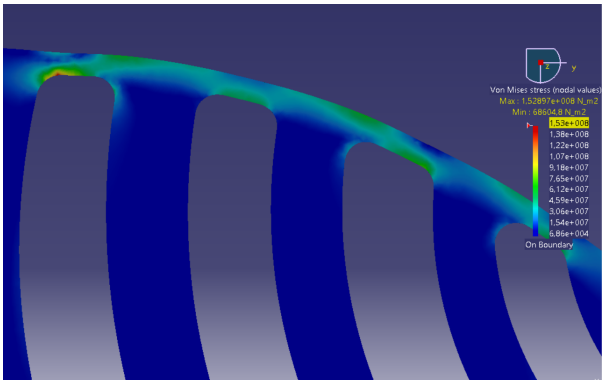

(d) Max von Mises stress design 1

Figure 7.7: Stress analysis results for design 1

For the centripetal force the maximum stress was in the tangential rib closest to the d-axis of the rotor. The stress from the deceleration instead had its maximum along the d-axis flux path at its thinnest point. The maximum stress when the cases are combined was in the tangential rib closest to the d-axis as in figure 7.7d. The maximum stress yielded a safety factor of

$$sf_1 = \frac{\sigma_y}{\sigma_v} = \frac{450\text{MPa}}{145\text{MPa}} = 2.94 \tag{7.1}$$

The experienced stress on the rotor lamination for design 2 can be seen in figure 7.8. The load cases are presented individually along with total von Mises stress experienced for the worst-case scenario.

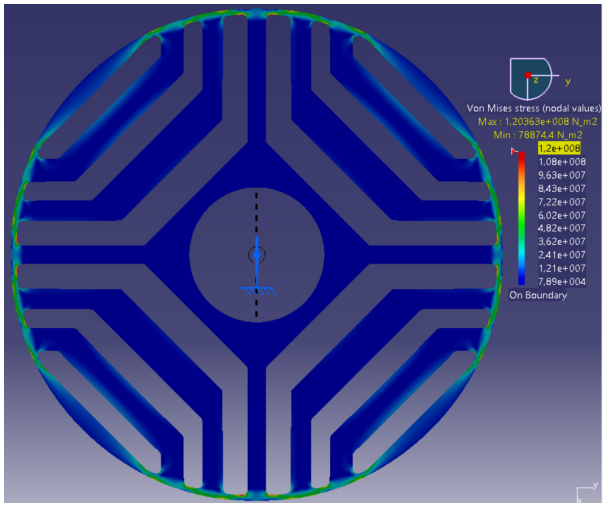

(a) von Mises stress design 2 when rotating at ω_{max}

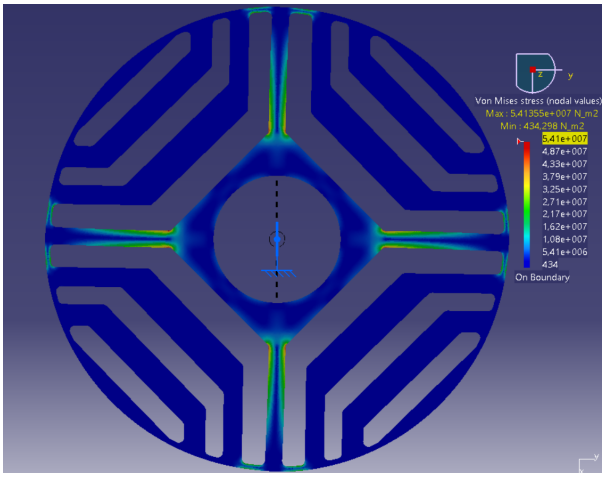

(b) von Mises stress design 2 from deceleration

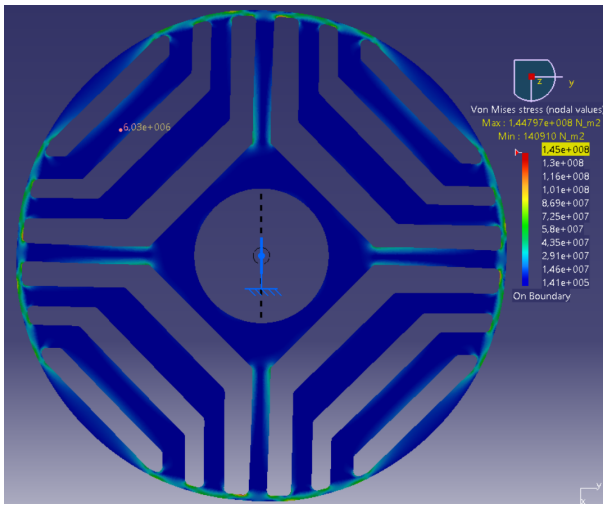

(c) Total von Mises stress design 2

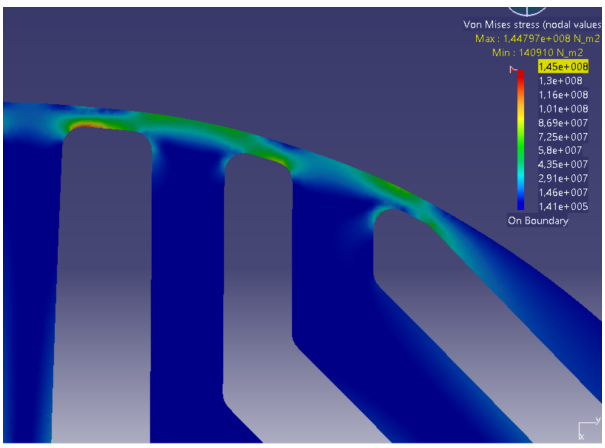

(d) Max von Mises stress design 2

Figure 7.8: Stress analysis results for design 2

The stress on the rotor has its maximum in different locations depending on the load case. The location of the maximum stress for the different load cases was very similar to that

of design 1. When decelerating, the von Mises stress concentrates along the flux path that connects the inner part of the rotor to the outer rim of the rotor. For the centripetal force, the von Mises stress was instead the highest in the tangential ribs, seen in figure 7.8a. The total von Mises stress was still small enough to give a safety factor of

$$sf_2 = \frac{\sigma_y}{\sigma_v} = \frac{450\text{MPa}}{145\text{MPa}} = 3.1 \tag{7.2}$$

The safety factor was higher than 3 which would indicate that the tangential ribs could be made smaller if not due to manufacturing limitations.

7.1.4 Choice of concept

Both designs had a significant safety factor and the performance was very similar. However, design 2 had a slightly higher torque production than design 1. The results for design 2 were also more consistent and could more easily be understood. For these two reasons it was decided that from this point design 2 would be used for the final design of the SynRM.

7.1.5 Addition of radial ribs

The performance with the radial ribs are presented in table 7.10. The mechanical stress can be seen in figure 7.9.

Table 7.10: Performance parameters with radial ribs

Performance Parameter	**Rib 0.5 mm**	**Rib 1 mm**
Torque	0.97 [p.u]	0.91 [p.u]
Torque ripple	7.5%	7.7%
Efficiency	86.6%	0.859%
PF	0.57	0.535
Phase Voltage RMS	41.54 [V]	41.68 [V]

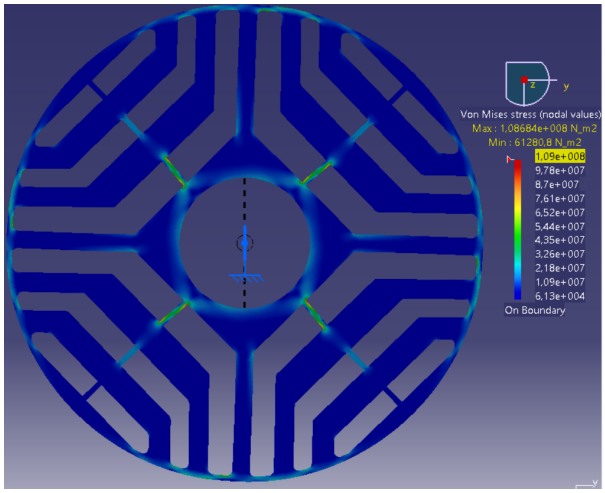

(a) Total von misses stress with 0.5 mm rib

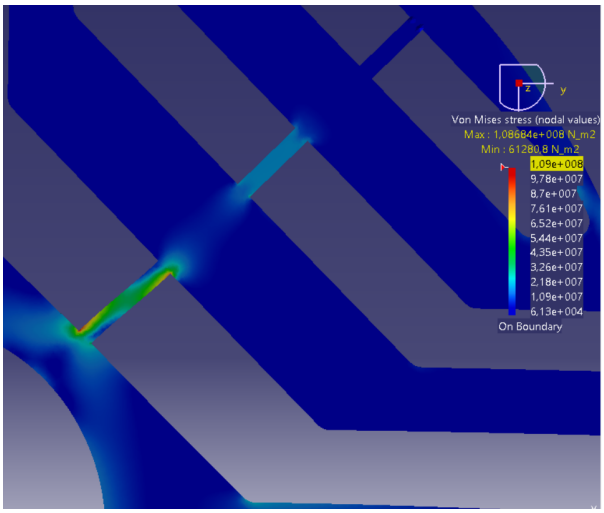

(b) Maximum von Misses stress 0.5 mm rib

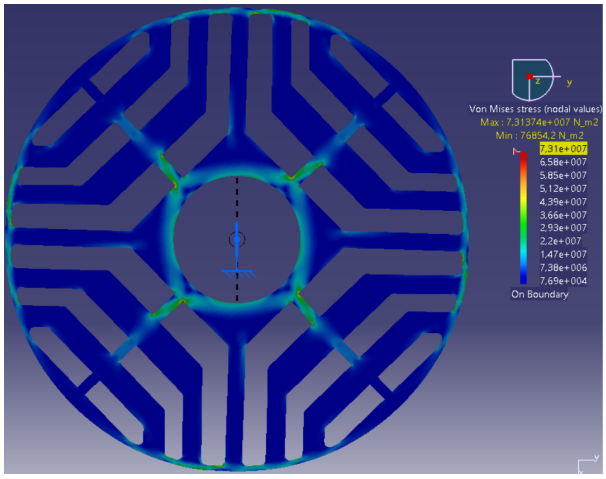

(c) Total von misses stress with 1 mm rib

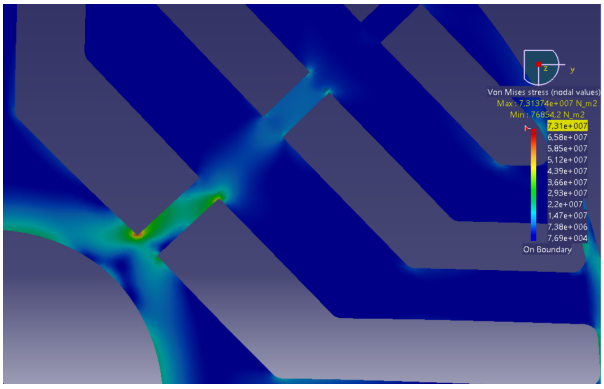

(d) Maximum von Misses stress 1 mm rib

Figure 7.9: Stress analysis results when using radial ribs

As expected the stress reduces with increased rib size, but at the cost of decreased performance of the SynRM since leakage flux can now flow through these ribs, see figure 7.10. Interestingly, the stress is now concentrated in the first radial rib. This is due to the deceleration force creating a larger force in the body closer to the shaft and since the rib is quite thin the stress becomes high. Since it was determined that the safety factor was sufficient without radial ribs. It was decided that no radial ribs would be used for the final design of the SynRM.

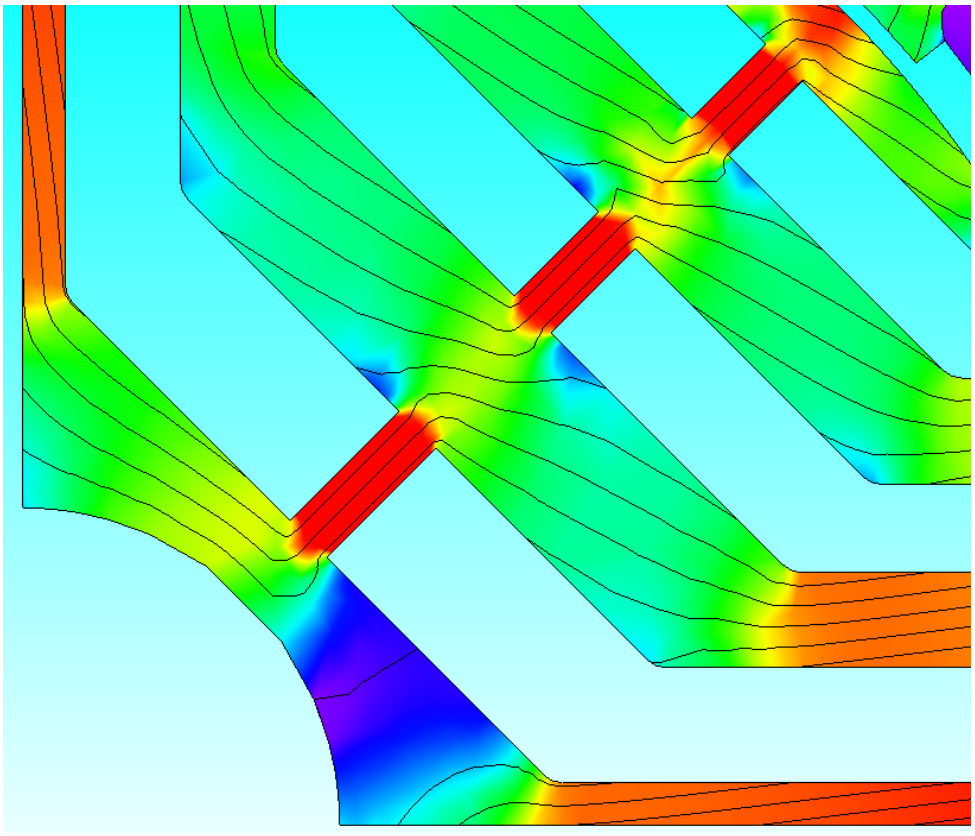

Figure 7.10: Leakage flux in the radial ribs

7.1.6 Change of stator steel

Changing the stator steel to the same as in the rotor yielded a slight performance increase. This was due to the iron losses being reduced when compared at the same operating point with M330-50A. The performance results are presented in table 7.11

Table 7.11: Results when using M270-35A steel in the stator

Performance Parameter	**Value**
Torque	1.05 [p.u]
Torque ripple	8.5%
Efficiency	87.4%
PF	0.6
Phase Voltage RMS	41.8 [V]

The reason for the increased torque production becomes clear when looking at (2.33). The lamination thickness d directly influences the size of the iron losses and since the lamination thickness was changed from 0.5 mm to 0.35 mm the losses decrease. Because of the slightly better performance of the M270-35A this steel was used from this point forward in the project in both the stator and the rotor.

7.1.7 Change of stator slot pitch angle

As was mentioned in section 5.1 the stator slot pitch was initially changed to full pitch $y = 6$, however, the effect of the pitch was studied for three cases described in the table 7.12.

Table 7.12: Effect of slot pitch

Performance Parameter	$y = 6$	$y = 5$	$y = 4$
Torque	1.05 [p.u]	1.045 [p.u]	0.935 [p.u]
Torque ripple	8.5%	9.6%	8.3%
Efficiency	87.4%	88.3%	88.1%
PF	0.6	0.617	0.63
Phase Voltage RMS	41.80 [V]	40.2 [V]	34.90 [V]

As expected the torque decreases for lower y. In the case when $y = 4$ gives a torque much lower than the others which were not desirable. However for a slot pitch of $y = 5$ the torque drop was very low, but with a larger increase in PF and decrease in voltage. It was therefore decided that $y = 5$ would be used. The β_c that gave the highest torque was slightly decreased due to the change in pitch to $\beta_c = 65°$.

7.1.8 Final SynRM design

With the final rotor design of the SynRM decided, the stack length of the motor was adjusted to match the mechanical torque produced by the reference IPM motor. It was found that to achieve 1.0 p.u torque the stack length could be decreased to only 52% longer than the IPM. It should be noted that the stack length can only be as long as a multiple of the lamination thickness. That is why the torque is slightly higher than that of the IPM. The performance result after this and the final performance result of the SynRM are presented in table 7.13. The full geometric parameters can be seen in table 7.14.

Table 7.13: Final design SynRM performance parameters

Performance Parameter	**Value**
Torque	1.0 p.u.
Torque ripple	9.6%
Efficiency	88.1%
PF	0.617
Phase Voltage RMS	38.55 [V]

Table 7.14: Geometric parameters for the final rotor geometry

Geometry Measurments	Value	Description
$W_{q,1}$	2.97 [mm]	Width of flux barrier 1 in q-direction
$W_{q,2}$	2.30 [mm]	Width of flux barrier 2 in q-direction
$W_{q,3}$	2.00 [mm]	Width of flux barrier 3 in q-direction
$W_{d,1}$	2.20 [mm]	Width of flux barrier 1 in d-direction
$W_{d,2}$	1.70 [mm]	Width of flux barrier 2 in d-direction
$w_{t,1,2,3}$	0.50 [mm]	Width of tangential ribs
$S_{q,1}$	1.66 [mm]	Width of flux path 1 in q-direction
$S_{q,2}$	3.12 [mm]	Width of flux path 2 in q-direction
$S_{q,3}$	2.53 [mm]	Width of flux path 3 in q-direction
$S_{q,4}$	1.50 [mm]	Width of flux path 4 in q-direction
θ_1	5.07°	Rotor positon angle for flux barrier 1
θ_2	15.20°	Rotor position angle for flux barrier 2
θ_3	25.36°	Rotor position for flux barrier 3
R_{shaft}	6.08 [mm]	Shaft radius
R_{rotor}	22.15 [mm]	Rotor radius
Fillet	0.50 [mm]	End barrier fillet radius

7.2 PMaSynRM

The result of the two cases for the magnet placement are shown in table 7.15.

Table 7.15: Performance parameters with the addition of ferrite magnets

Performance Parameter	Case 1	Case 2
Torque	1.28 [p.u]	1.382 [p.u]
Torque ripple	11.0%	9.5%
Efficiency	90.2%	90.9%
PF	0.74	0.795
Phase Voltage RMS	39.88 [V]	38.88 [V]

7.2.1 Final PMaSynRM design

Since the torque and power factor were significantly better for the second case this was the one used for the final design of the PMaSynRM. After the addition of ferrite magnets $\beta_c = 60°$. Because of the high torque and PF the size of the motor could be reduced to 17.7% longer than the IPM. The performance result for the length adjusted PMaSynRM

can be seen in table 7.16.

Table 7.16: Performance parameters with the addition of ferrite magnets

Performance Parameter	**Value**
Torque	1.02 [p.u]
Torque ripple	9.5%
Efficiency	90.0%
PF	0.8
Phase Voltage RMS	29.74 [V]

The most significant change of course is the reduction in voltage needed to maintain the base speed. Otherwise, the torque ripple, efficiency, and PF are essentially the same.

7.3 Performance comparison of the motors

In table 7.17 the performance comparison of the SynRM and PMaSynRM compared to the IPM motor is shown along with how the size has to be changed to achieve the same performance.

Table 7.17: Performance comparison of all motors in this project

Performance parameter	**IPM**	**Ref. SynRM**	**SynRM**	**PMaSynRM**
Torque	1.0 [p.u]	0.96 [p.u]	1.0 [p.u]	1.02 [p.u]
Torque Ripple	2.3%	42.7%	9.6%	9.5%
Efficiency	94.7%	85.1%	88.1%	90.0%
Losses	211.6 [W]	626.2 [W]	553.2 [W]	490.8 [W]
PF	0.835	0.527	0.617	0.8
Phase Voltage RMS	33.23 [V]	44.2 [V]	38.55 [V]	29.744 [V]
Stack length	1.0 [p.u]	1.81 [p.u]	1.52 [p.u]	1.18 [p.u]

It is clear that the SynRM design is an improvement compared to the reference SynRM in that the torque performance is achieved with a smaller motor and a significant decrease in torque ripple. The PMaSynRM performs even better because of its higher power factor.

7.4 Cost comparison

In table 7.18, 7.19 and 7.20 the cost for the SynRM, PMaSynRM and IPM motor respectively is presented along with there total weight.

Table 7.18: Results for the cost of the SynRM

Material	**Case 1 (Normal) [€/kg]**	**Case 2 (Today) [€/kg]**	f_{mf}	**Weight [kg]**	**Material Cost [€]**	**Cost [€]**
Stator						
M270-35A	1.5	1.5	1.5	0.54	0.81	1.22
Copper	6	9.5	1.5	0.43	2.55/4.05	3.83/6.07
NO20	1.6	1.6	1.5	0	0	0
Rotor						
M270-35A	1.5	1.5	1.5	0.2	0.3	0.45
Ferrite FB5D	1.45	1.45	1.5	0	0	0
NdFeB N45SH	60	100	1.5	0	0	0
M800-50A	1.2	1.2	1.5	0	0	0
Total				1.17	3.66/5.16	5.49/7.74

Table 7.19: Results for the cost of the PMaSynRM

Material	**Case 1 (Normal) [€/kg]**	**Case 2 (Today) [€/kg]**	f_{mf}	**Weight [kg]**	**Material Cost [€]**	**Cost [€]**
Stator						
M270-35A	1.5	1.5	1.5	0.42	0.63	1.22
Copper	6	9.5	1.5	0.38	2.28/3.61	3.42/5.42
NO20	1.6	1.6	1.5	0	0	0
Rotor						
M270-35A	1.5	1.5	1.5	0.156	0.23	0.35
Ferrite FB5D	1.45	1.45	1.5	0.06	0.09	0.13
NdFeB N45SH	60	100	1.5	0	0	0
M800-50A	1.2	1.2	1.5	0	0	0
Total				1.02	3.23/4.56	4.85/6.84

Table 7.20: Results for the cost of the IPM motor

Material	**Case 1 (Normal) [€/kg]**	**Case 2 (Today) [€/kg]**	f_{mf}	**Weight [kg]**	**Material Cost [€]**	**Cost [€]**
Stator						
M270-35A	1.5	1.5	1.5	0.42	0	0
Copper	6	9.5	1.5	0.21	1.26/2.00	1.89/2.99
NO20	1.6	1.6	1.5	0.28	0.45	0.67
Rotor						
M270-35A	1.5	1.5	1.5	0	0	0
Ferrite FB5D	1.45	1.45	1.5	0	0	0
NdFeB N45SH	60	100	1.5	0.09	5.40/9.00	8.10/13.50
M800-50A	1.2	1.2	1.5	0.13	0.16	0.23
Total				0.71	7.27/11.61	10.91/17.42

Because the PMaSynRM could be made shorter and that ferrite magnets are cheap compared to Neodynium magnets, the overall price for the PMaSynRM became lower than that of the SynRM. As expected the IPM motor is a lot more expensive. The SynRM is only 44.4 % to 50.3 % of the cost of the IPM motor and the PMaSynRM is 39.2 % to 44.3 % of the IPM motor. The weight increases for SynRM with 64.8 % and 44.5 % for the PMaSynRM compared to the IPM motor, see figure 7.11. With ferrite magnets, a lot of performance can be gained without sacrificing the cost aspect.

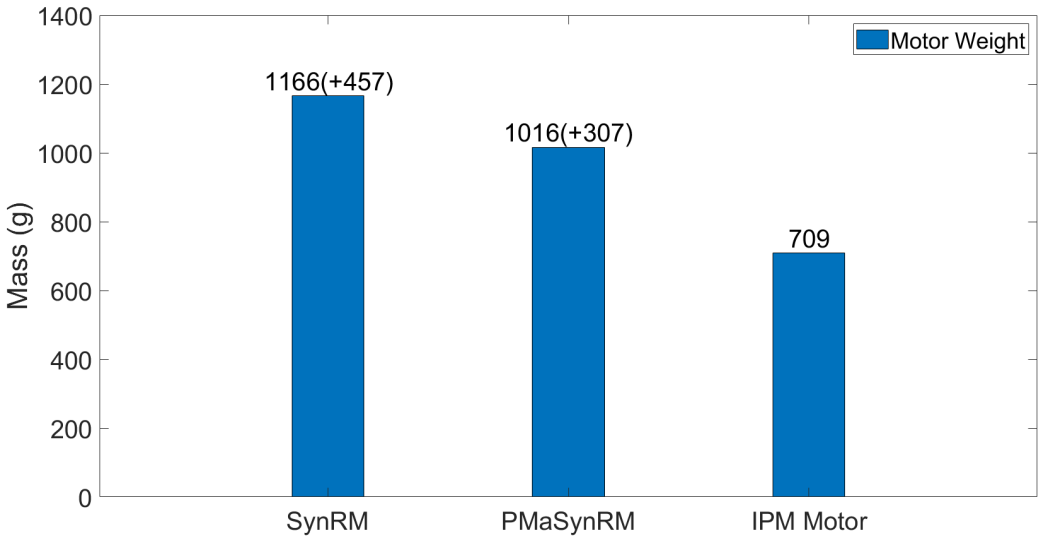

Figure 7.11: Total weight of the motors

7.5 Motor mapping

In figures 7.12a and 7.12b the torque speed curves with an efficiency map for both the SynRM and the PMaSynRM are shown respectively.

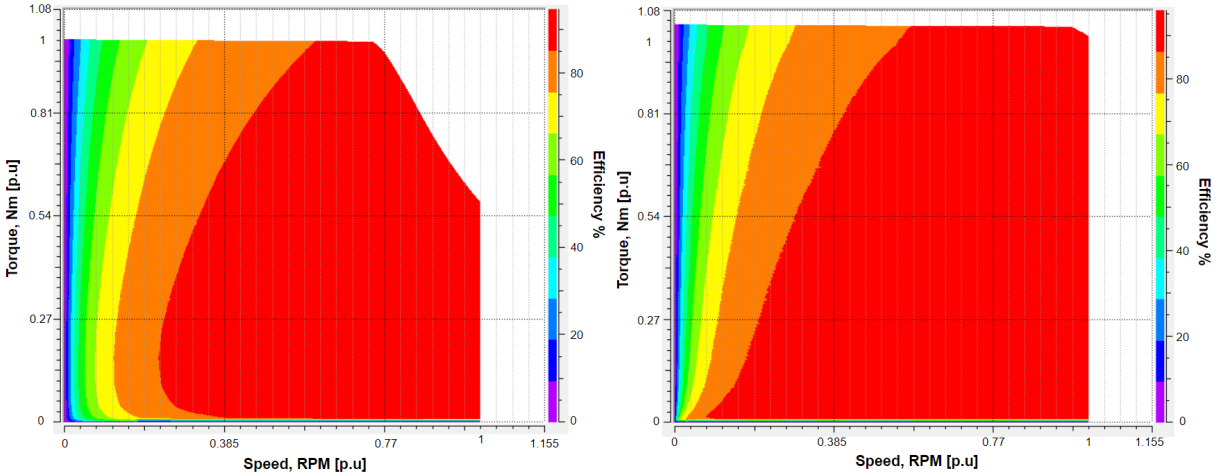

(a) Torque speed curve SynRM

(b) Torque speed curve PMaSynRM

From figure 7.12b and table 7.17 it is clear that the voltage is underutilized for the PMaSynRM. The stator is not ideal for the PMaSynRM. A redesign of the windings could lead to the need for less current and the voltage instead being utilized more. This was however not studied further in this project.

The inductance data for the SynRM are presented in figures 7.13a and 7.13b and for the PMaSynRM in figures 7.14a and 7.14b.

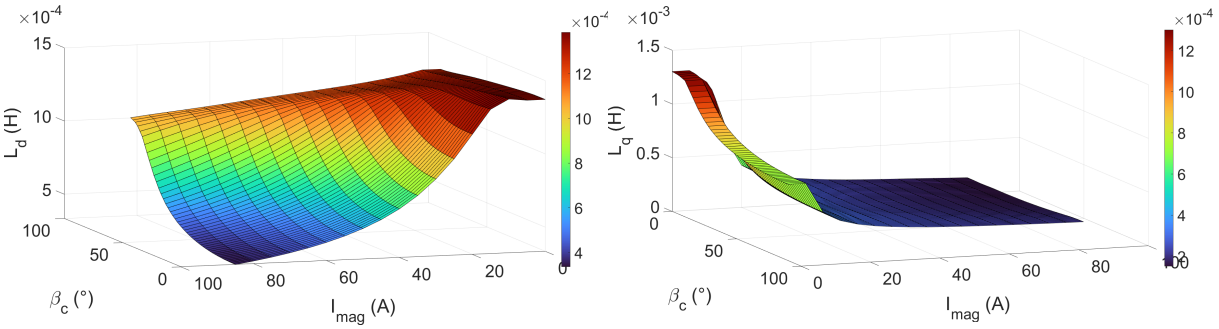

(a) $L_d(I_{mag}, \beta_c)$

(b) $L_q(I_{mag}, \beta_c)$

Figure 7.13: L_d and L_q values dependent on the current magnitude and current angle for the SynRM

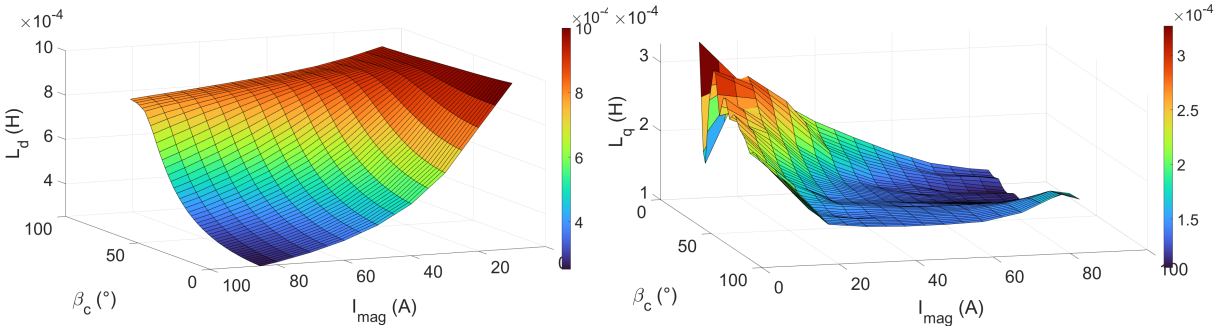

(a) $L_d(I_{mag}, \beta_c)$ (b) $L_q(I_{mag}, \beta_c)$

Figure 7.14: L_d and L_q values dependent on the current magnitude and current angle for the PMaSynRM

In table 7.21 the value for ψ_{pm} for the PMaSynRM is shown. Initially, ψ_{pm} is negative indicating that the optimal torque angle will be very different for low levels of current compared to when operating at maximum current.

Table 7.21: ψ_{pm} for the PMaSynRM

I_d **[A]**	10	20	30	40	50	60	70	80	90
ψ_{pm} **[mWb]**	-4.43	-3.56	-2.25	-0.91	0.48	1.98	4.13	7.60	7.78

7.6 SynRM drive

The SynRM drive results presents the performance of the SynRM with the designed drive system. Apart from in section 7.6.5 the switching frequency is set to $f_{sw} = 20$ kHz. The results of the inverter analysis are also presented.

7.6.1 Complete drive system simulation results

The response of the current controller for the SynRM is presented in 7.15. Figure 7.15a plots the produced torque and the requested torque. In figure 7.15b the inductances in d- and q-axis are plotted. L_d and L_q from the RT model are compared with the table-generated values.

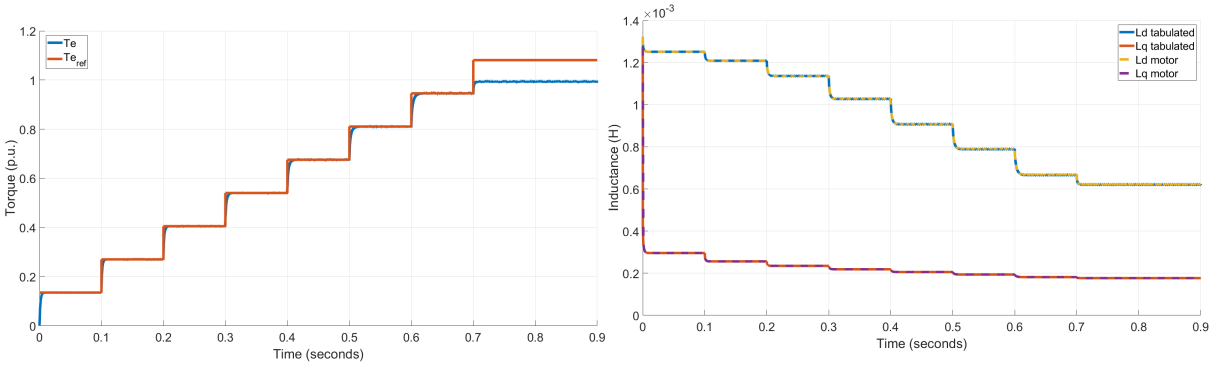

(a) Torque request vs produced torque

(b) Simulated motor inductance vs tabulated inductance in d- and q-axis

Figure 7.15: Result of the drive system with the current controller and torque request as input, where the inductance data is tabulated for updating regulator parameters.

Tabulated data for the inductance matches well with the simulation data. When the tabulated values for L_d and L_q are used for updating the regulator parameters in the current controller and for calculating the current reference from a torque request, the produced torque matches well the torque reference up to $T_e = 1$ p.u. For values above $T_e = 1$ p.u. the system is limited in current.

The complete drive system with speed control is presented in 7.16. The governing speed reference and the simulated rotor speed are plotted in 7.16a. The torque requested by the speed controller is plotted in 7.16b together with the produced torque, T_e and the external mechanical load, T_{ext}. Simulated and tabulated values of L_d and L_q are plotted in 7.16c. The performance of the current controller is illustrated in figure 7.16d where requested values are plotted together with the measured and sampled motor values, all in the dq-frame.

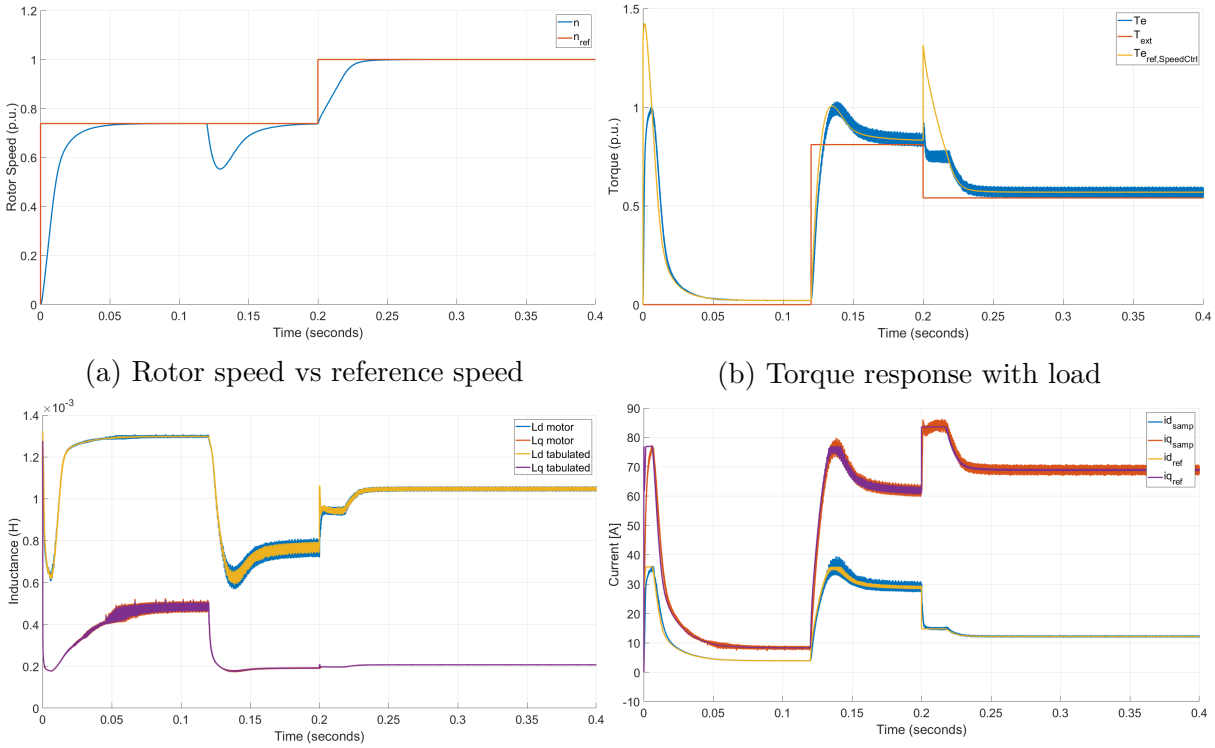

(a) Rotor speed vs reference speed

(b) Torque response with load

(c) Tabulated vs simulated inductance

(d) Motor current vs reference current

Figure 7.16: Result of the complete drive system with the ideal inverter model and speed controller.

The response of the current controller is as desired in terms of rise time. The overshoot is minimal or none and no remaining error is noticed. The outer speed controller can then perform with a corresponding behavior which is also noted. A noise is recorded on the currents which is partly regarded as inverter harmonics. This also affects the torque signals. Only a minimal noise is observed on the rotor speed, due to the slower dynamics. The speed reference is increased from ω_n to ω_{max} at 0.2 s. At this time point, the current angle is changed from $\beta_{MTPA} = 65°$ to $\beta_{FW} = 80°$.

7.6.2 Inverter performance

To evaluate the behavior of the inverter models, the currents are assessed. In figure 7.17 the phase current and the inverter DC side current for the ideal inverter are plotted. Similarly, the currents for the non-ideal inverter with SPICE imported MOSFETs at plotted in figure 7.18.

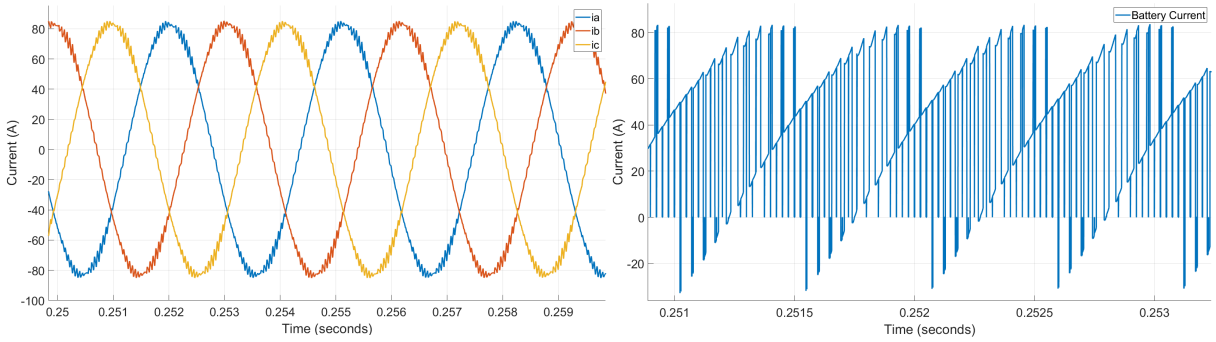

(a) 3-phase currents

(b) Inverter DC side current

Figure 7.17: Ideal inverter model steady state drive operation of the SynRM

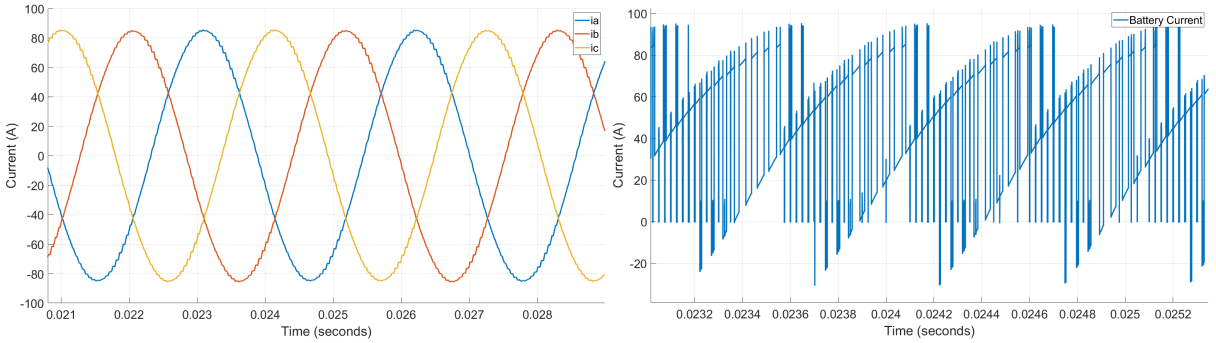

(a) 3-phase currents

(b) Inverter DC side current

Figure 7.18: Non-ideal inverter model SynRM equivalent load

In the inverter DC side current for the Non-ideal inverter, the difference in the MOSFET on resistance and the forward resistance of the body diode is noticed by the smaller spikes. The figures also indicate a higher inverter DC side current for the Non-ideal inverter with the SynRM equivalent load than the ideal model with the operation of the SynRM. The phase currents are however the same in magnitude.

7.6.3 Inverter efficiency

The power losses as a result of the load, as well as the resulting efficiency are presented in table 7.22 & 7.23. Table 7.22 presents the cases where the Ideal Inverter was used. Here the SynRM is compared with its equivalent load. Table 7.23 presents the cases when then non-ideal inverter was used, and the efficiencies are highlighted.

Table 7.22: Ideal inverter model with the SynRM load and the SynRM equivalent load

Inverter model		**Ideal model**	**Ideal model**
Load model	Unit	**SynRM Jmag design**	**SynRM equivalent load**
R_{ds} (datasheet)	Ohm	0.0043	0.0043
Switching freq. f_{sw}	kHz	20	20
Electrical freq.	p.u.	0.7370	0.7385
PF	-	0.6046	0.6170
Phase angle (real)	deg	52.8000	51.9000
THD (Phase current)	%	3.00	0.83
Battery Power, P_{batt}	kW	4.1443	4.2816
Inverter Power, P_{inv}	kW	4.1173	4.2422
Apparent Power	kVA	6.8100	6.8751
Power loss, $P_{l,inv,sim}$	W	27.0091	39.4137
Efficiency, $\eta_{inv,sim}$	%	**99.35**	**99.08**

The FFT analysis on the SynRM Jmag design, the RT-model, was performed on at steady-state part of a drive sequence. The operating point at the base speed, $n = 0.7385$ p.u. and the torque of $T_e = 1$ p.u. was aimed for. The actual operation in the test was $n = 0.7370$ p.u. and $T_e = 0.98$ p.u. The rotational speed is also reflected in the measured electrical frequency, noted as the fundamental component when performing the FFT analysis.

The power output from the battery with the SynRM JMAG design is 137 W lower than with the equivalent load. The PF is also lower. The discrepancy is partly due to that the SynRM is not operating completely at its desired operating point, where the equivalent load is calculated to be. And also due to the accuracy of the imported JMAG-RT motor. The error in efficiency when driving the equivalent load is 0.27% when compared to the actual motor design.

Table 7.23: Inverter efficiency and power losses for the different motor equivalent loads

Inverter model		**SPICE model**	**SPICE model**	**SPICE model**
Load model	Unit	**SynRM equiv.**	**IPM equiv.**	**PMaSynRM equiv.**
Switching freq. f_{sw}	kHz	20	20	20
Electrical freq.	p.u.	0.7385	0.3692	0.7385
PF (load calc.)	-	0.6170	0.8370	0.8000
Phase angle (real)	deg	52.0000	33.1000	36.9000
THD (phase current)	%	0.8900	0.5800	1.1300
Battery Power, P_{batt}	kW	4.3872	3.9414	4.2535
Inverter Power, P_{inv}	kW	4.2662	3.8728	4.1382
Apparent Power	kVA	6.9295	4.6230	5.1747
Power Loss, $P_{l,inv.sim}$	W	120.9779	68.6476	115.3352
Efficiency	%	**97.24**	**98.26**	**97.29**

The higher current and voltage due to the lower power factor results in a greater power loss in the inverter. This explains the higher power loss in the SynRM and PMaSynRM compared to that of the IPM motor. The PMaSynRM gives a similar result in efficiency as the SynRM and the increased losses of the motors compared to the IPM motor are identified to be due to the higher currents. The PMaSynRM and the SynRM are set to the same current level, the actual RMS phase currents are 59.0 A, and 59.9 A respectively. In figure 7.19 the summarized losses for the system with motor and inverter are shown. The motor operates at a torque of 1 p.u and at the base speed, the inverter is using a switching frequency of 20 kHz.

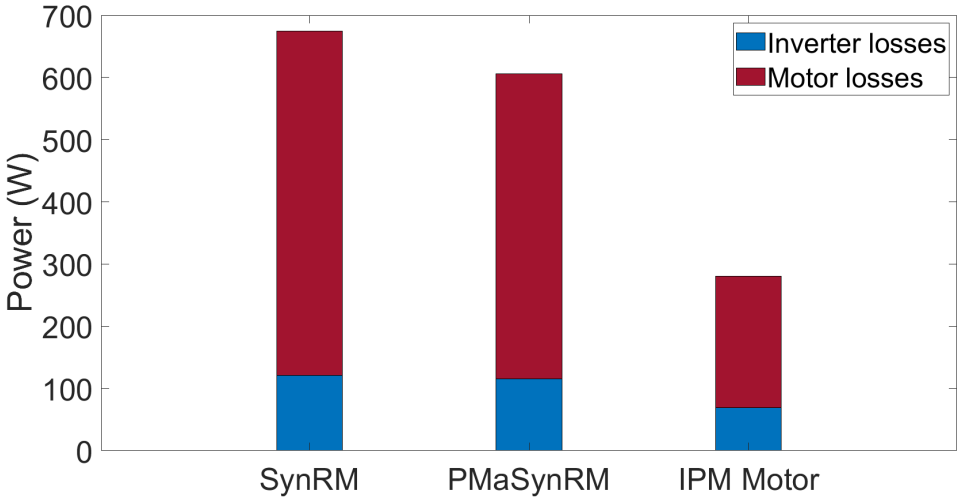

Figure 7.19: Total Power losses in the drive system for the three different motors, all operating at the base speed and a torque of 1 p.u

7.6.4 Power losses from the theoretical model

The results from the theoretical model calculated for the motor equivalent load are presented in table 7.24.

Table 7.24: Results from the theoretical model

Load model	Unit	**SynRM**	**IPM**	**PMaSynRM**
Conduction losses, P_{cond}	W	64.7	38.6	62.6
Switching losses, P_{sw}	W	20.5	16.5	19.9
Total Power losses, inverter, $P_{l,inv}$	W	85.2	55.1	82.5
Error compared to simulated	%	**29.5**	**19.8**	**28.5**

This presents a difference in the theoretical model compared to the simulated values. The error is presented as an error compared to the simulated value.

7.6.5 Harmonics and switching frequency

In table 7.25, the effect on losses and THD in the currents for different f_{sw} are presented. The same drive cycle as in 7.16 is then simulated, also with the different switching frequencies, and the current in the dq-frame and the produced torque can be seen in figure 7.20.

Table 7.25: Power Losses and THD as a result of changes in f_{sw}

Inverter model		**SPICE model**		
Load model	Unit	**SynRM equiv.**		
Switching freq.	kHz	5	20	50
THD (current)	%	3.36	0.89	0.6
Power Loss	W	78.7019	120.9779	178.7900
Efficiency	%	0.9817	0.9724	0.9605

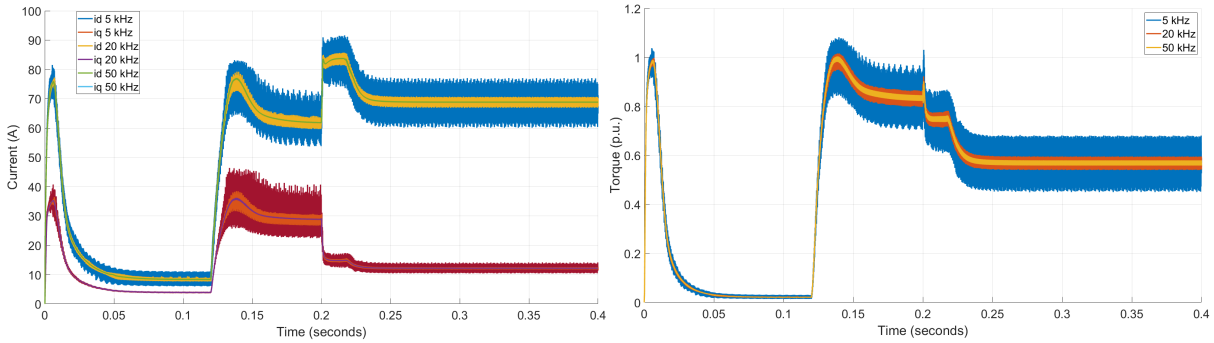

(a) d- & q-current

(b) Produced motor torque

Figure 7.20: Motor drive behaviour with ideal inverter and different f_{sw}

With a higher switching frequency, the harmonics in the current and the torque ripple become significantly lower at the cost of more losses in the inverter.

7.6.6 Component validation

The datasheet for the infineion OPTIMOS IPB100N12S3-05 MOSFET presents a maximum drain-source voltage of 120 V. The maximum voltage existing in the drive system would be lower than this. The inverter performance analysis suggests that the SynRM drive would give a power loss, $P_{l,inv,sim} = 121$ W at the operation in base speed and torque close to the maximum possible of the system. As suggested by the analysis, up to a third of this inverter loss could be dissipated by one MOSFET. This dissipated power is lower than the maximum rated by the MOSFET datasheet, stating a maximum of 300 W.

Validating the safe operating area of the MOSFET then results in that the operation will be below the maximum power limit. When using $f_{sw} = 20$ kHz, operation within the limit of thermal stability of the safe operating area can not be guaranteed for this MOSFET according to this work. With the resolution available in the datasheet and the plot for safe operating area, the operation of the MOSFET would more or less lay on the line of safe operation in terms of thermal stability and a thermal runaway can with these results not be guaranteed to be avoided.

8
Discussion

When it comes to the slot pitch and torque ripple, it might not be the same ideal β_s when changing the pitch for minimizing the torque ripple. The small loss in torque when changing y from 6 to 5 could be due to problems with saturation of the steel since the loss in performance is less than expected. The ideal barrier design is not necessarily the same when the pitch changes. Especially the ideal value for β_s since the flux paths in the rotor is the same when the pitch is changed. So the ideal relation between the stator and rotor slot openings could potentially change for a different slot pitch. In general, the stator should be studied more. Most likely the ideal stator for the presented rotor design would be different.

The first design approach for the SynRM design needs more work. The design is simple, but harder to say exactly what parameters are best. From design 1 compared to design 2, it is clear that more barriers do not necessarily increase performance since the shape of the barriers and their positioning is also of great importance.

Just adding ferrite magnets to the SynRM rotor structure might not be an ideal way of creating a PMaSynRM in terms of maximum performance. Also from a manufacturing standpoint, it is questionable if 4 different sizes of magnets is a good idea. This is because the different-sized magnets could increase complexity in the assembly and lead to more problems with magnets accidentally being placed incorrectly. Also, tolerances for ferrite magnets can be quite bad and this is an aspect that might be a problem when working with very small geometries in the rotor. Significant performance could be lost if the magnets need to be made smaller to account for tolerances. The assumption of a 2 mm minimum thickness of the ferrite magnets was based on information from different suppliers. However, this needs to be investigated further. Especially since making the magnets this thin, could make the manufacturing much harder and therefore the cost would increase more. The stator design is also not ideal for the PMaSynRM since the voltage of the battery becomes underutilized. It is also clear from the inverter loss results that even though the IPM motor and the PMaSynRM have a much closer PF, the losses are still significantly larger for the PMaSynRM due to the current being larger. The winding arrangement should be redesigned for the PMaSynRM so that more windings are used while decreasing the current level.

The process factor suggested in this project is questionable. It is not likely that the added processing cost will be the same percentage-wise for all materials. Especially if more advanced manufacturing techniques are needed for certain materials, for example when making really thin ferrite magnets. However, the process factor was kept in place

to say something about the total cost of the motor parts and not just the material itself.

The results indicate that the nominal battery voltage has to increase slightly from the reference battery voltage at 94 V to achieve the desired base speed for the SynRM. Even though using zero sequence injection would mitigate this problem, the battery voltage would still have to be increased. When the battery discharges, the voltage will drop, and to keep the same base speed, a margin is needed to compensate for the lower voltage at a low state of charge. This would imply that the battery voltage needs to be further increased. An alternative is a redesign of the stator windings and increasing the current. This could however lead to thermal limitations and increasing the current will still mean the same or more energy consummation out from the battery. However, other practical reasons, such as keeping a finite amount of cells in the battery or that the capacity is aimed to be the same, might propose that the battery design is not changed. A conclusion for the battery size should be taken from a product perspective where several aspects are considered.

The results show that in the simulation environment, it is possible to have a perfect estimation of the motor inductance. This has a direct influence on the torque estimation and the current reference calculation. However, it is unlikely that an actual implementation and a motor benching would give the same accuracy. Manufacturing tolerances of the motor, temperature changes and disturbances would most likely lead to a difference in estimated inductance values and real values. Such an error will affect the torque estimation. But the motor control would most likely be accurate in terms of rotor speed. The speed controller would compensate for errors in the inner loop of the controller. The consequences of a possible error in inductance estimation should be further investigated.

Similar to the torque estimation, the theoretical models for MTPA and field weakening have a high dependency on the inductance parameters. The theoretical field weakening model uses fixed values of L_d and L_q to illustrate the voltage ellipse and its dependency on back-emf which serves the purpose of explaining the governing theory. But it might not alone be recommended for selecting β_{FW}. Firstly it is recommended that a comparator is used for comparing the measured (or estimated) rotor speed with the base speed. Then a calculation block can be used together with the tabulated inductance values to define a β_{FW} in each control sequence.

When adding the speed controller, and more eminently, using the complete Simscape model with the physical signals, noise is introduced on the currents and also present on the inductance values as well as the produced torque. As suggested in the results, the noise must originate from the inverter. Changing the switching frequency to higher values would lower the harmonics from the inverter, but the switching losses in the inverter would also increase.

From the analysis of the switching frequencies, no single value can be recommended as the best solution, but some consequences can be seen. $f_{sw} = 5$ kHz does give a pronounced additional ripple in torque. The simulations confirm that the inverter losses will be the lowest in the comparison. But the higher THD will lead to a less sinusoidal current and

magnetic flux that are likely to increase the iron losses in the motor. $f_{sw} = 50$ kHz gives a more pure signal but might instead lead to problems in electromagnetic interference. When simulating the switching frequency of $f_{sw} = 20$ kHz it can be seen that a majority of the harmonics can be dampened, the THD is significantly lower than in the 5 kHz case and the additional torque ripple is also kept low. When selecting the switching frequency the accepted torque ripple for the end product should be considered. It is also important to regard that in this simulation the motor model itself does not model any harmonics, which is something that should be considered when validating the drive system and the switching frequency.

When it comes to the mechanical analysis it is questionable if the fillets are needed at every endpoint for every barrier. Since this leads to an increase in iron in the q-axis and any fillets that are not needed would ideally be removed to increase performance. The fillets should most likely only be implemented for the first and potentially the second barriers since the stress is lower further away from the d-axis in the rotor.

Due to the assumptions in the theoretical model, it was assumed that the errors in the theoretical model were greater than the errors for the simulation model with the SPICE MOSFETs. But, it should be mentioned that also the simulation models are only a model of reality which also give errors. With this said though, in the analysis, the simulation model with the SPICE MOSFETs was treated as the correct model in the sense that other models gave an error in comparison to this. To find a single reason or to explain the discrepancy in the theoretical model is in general difficult since the errors are difficult to isolate to one of the single assumptions that were made. However, it should be said that it was unexpected that the losses were lower compared to the simulated values since Infineon Technologies indicate that linearization of the switching process presents a worst-case scenario.

The inverter performance was to a high degree validated with an RL equivalent load. This decision was motivated for two main reasons, firstly, in the time frame for this project, it was not possible to optimize the simulation model with the SPICE MOSFETs, and also not possible to find a set of solver settings that would give reasonable results. Secondly, since the SynRM was the scope of the project, it was not reasonable to implement a motor-specific RT-file and a drive system for all three motors.

The RL-equivalent load yield discrepancy compared to if the complete RT-mapped motor models would have been used. However, when using the ideal inverter model to compare the RL-equivalent load with the RT-model of the SynRM it could be shown that the difference was minimal. The RL-equivalent load was finally considered to be accurate enough to give a fruitful analysis in comparing the motors at the specified operating point. To only compare the motors in one operating point does however not give a complete validation since the difference in performance will differ at different operating points.

8.1 Ethical, social and environmental aspects

As was discussed in section 1.4, the ability to get a good performance and to remove rare earth magnets was important for environmental and ethical reasons. The SynRM model does away with the rare earth elements, but the efficiency is lower at the studied operating point and the lower power factor also creates more losses in the inverter. It was also discussed that it is important to keep high efficiency and it is therefore of concern that the efficiency will be lower. The fact that the voltage needs to be higher for the SynRM could also increase the size of the battery. Batteries usually contain rare earth elements which have negative environmental consequences when manufactured. So if the battery needs to be made larger for the SynRM, a lot of the environmental gain from removing rare earth magnets could be lost. This is less of a problem when adding ferrite magnets since the voltage level is lower for the PMaSynRM due to the higher PF.

Even though the efficiency might be lower for the entire system, the SynRM and PMaSynRM were less expensive than the IPM motor. This is good from a social perspective since it could mean that more people can afford the products that the motors will be used in.

9
Conclusion

A SynRM was designed which was an improvement compared to the reference SynRM designed before the project. The low power factor of the SynRM compared to the IPM motor means that something has to change in the system to achieve the same mechanical performance. The motor either has to be larger, supplied with more current, or be implemented with a larger battery to achieve the same performance mechanically as the IPM motor. It was shown that a lower power factor can be partially compensated for by the addition of ferrite magnets to the rotor making it a PMaSynRM.

In the case of this SynRM design, the battery DC voltage would have to increase to achieve the desired base speed for the SynRM. The stack length would also increase with or without the addition of ferrite magnets to match the mechanical performance. However, the cost of the SynRM and PMaSynRM is significantly lower than that of the IPM motors used today. Indicating that the decreased performance could be motivated because of the cost savings.

The small size of the SynRM makes it unnecessary to have radial ribs and by not having the radial ribs the performance is increased. The radial ribs are usually important for SynRM applications, but in this project, it was shown that for small enough rotors it may not be necessary.

Existing software made it possible to implement and simulate a complete drive system with the motor and the MOSFET being parameterized from actual hardware designs. Furthermore, the motor model in such simulations could embody the same motor that was designed in this work. Results show an expected behavior of the control system and the results gave a fruitful analysis in terms of power losses for the system. However, an RL-equivalent load had to be used for finding the inverter losses.

The motor might not be suited for small handheld products since it needs to be larger than the IPM motor to produce the same mechanical performance. Since the voltage should be increased a larger battery would be needed that further increases volume and weight adding to the problem. The lower PF also creates more losses in the inverter that drives the SynRM. This since the voltage or current has to increase, which inevitably creates higher losses in the inverter. As an alternative to increasing the battery voltage, a lower performance for the end product has to be accepted.

9.1 Future work

A more thorough analysis of PMaSynRM design needs to be made to establish if the ideal design is to maximize the SynRM performance first and then implement magnets. Preferably from a manufacturing standpoint, there should not be so many different-sized magnets. Another future work for the PMaSynRM is to implement a control system so that the SynRM and PMaSynRM can be compared in the complete drive system as well.

A more extensive mechanical analysis needs to be performed. Such as looking into vibrations and how important tolerances could be for the structural integrity of the rotor. Especially a structural analysis has to be performed for the PMaSynRM. In this project, the implementation was considered reasonable from a structural perspective, but the same mechanical analysis has to be performed when the magnets have been added as well.

Another important aspect is a thermal analysis of the motors. In this project, it was deemed sufficient to use a stator that for the given max current did not produce an unreasonable current density. That does not however mean that heat will not be a problem since the motor still needs to be cooled. Both the SynRM and the PMaSynRM are already longer and use a higher current than the reference IPM motor. The larger size could mean less space for a cooling system or that more space would need to be allocated to the cooling system which is not ideal for handheld applications.

When it comes to controlling the motor more extensive inertia and friction coefficient determination have to be made. The friction coefficient is particularly important since if the motor causes a lot of friction, less torque produced by the motor can be used for work.

For more accurate results, a 3D model of the motor should be made for future studies. The 2D model is a simplification of reality that gives a good indication of the motor's performance. With a 3D model, a higher accuracy could be achieved. Also with a complete 3D model, a more complete picture of the cost of the motor could be done. Now only the active material cost has been compared, but things like the housing and the shaft can more easily be considered with a 3D model.

A parameter that should be analyzed further is the gate driver voltage. In general, the Gate driver behavior should be further investigated to minimize the MOSFET conduction resistance. It should also be investigated if the total turn on and off time can be lowered to achieve lower switching losses.

A thermal model for the inverter should be advised to find how the dissipated heat can be removed from the MOSFET case. Along with this, further analysis of the thermal stability of the MOSFETs is suggested.

The imported motor model to Simulink was as mentioned of L_d and L_q accuracy. However, this leaves a lot of dynamics out of the control loop. From JMAG-RT it is possible to implement a motor model that also considers the harmonics of the motor to see how the added dynamics affect the rest of the powertrain components. The inverter already

produces harmonics and the added harmonics of the motor is a relation that is of interest to understand and see the results of.

Bibliography

[1] A. Trench and J. P. Sykes, "Rare earth permanent magnets and their place in the future economy," *Engineering*, vol. 6, pp. 115–118, Feb. 2020.

[2] J. M. Coey, "Perspective and prospects for rare earth permanent magnets," *Engineering*, vol. 6, pp. 119–131, Feb. 2020.

[3] K. S. Stegen, "Heavy rare earths, permanent magnets, and renewable energies: An imminent crisis," *Energy Policy*, vol. 79, pp. 1–8, Apr. 2015.

[4] S.-H. Shin, H.-O. Kim, and K.-T. Rim, "Worker safety in the rare earth elements recycling process from the review of toxicity and issues," *Safety and Health at Work*, vol. 10, pp. 409–419, 2019.

[5] C. Burkhardt, F. Carencotte, M. Gasparon, O. Gutfleisch, I. Higgins, M. Karajić, A. Klossek, M. Mäkinen, B. Schäfer, R. Schindler, B. Veluri, and R. Gauß, "Rare earth magnets and motors: A european call for action. a report by the rare earth magnets and motors cluster of the european raw materials alliance," Berlin, 2021.

[6] C. C. Pavel, R. Lacal-Arántegui, A. Marmier, D. Schüler, E. Tzimas, M. Buchert, W. Jenseit, and D. Blagoeva, "Substitution strategies for reducing the use of rare earths in wind turbines," *Resources Policy*, vol. 52, pp. 349–357, Jun. 2017.

[7] D. Fodorean, S. Giurgea, A. Djerdir, and A. Miraoui, "Numerical approach for optimum electromagnetic parameters of electrical machines used in vehicle traction applications," *Energy Conversion and Management*, vol. 50, pp. 1288–1294, 2009.

[8] Eurostat, "Electricity production, consumption and market overview." Available at `https://ec.europa.eu/eurostat/statistics-explained/index.php?title=Electricity_production,_consumption_and_market_overview` (Aug. 2021).

[9] R. R. Moghaddam, *Synchronous Reluctance Machine (SynRM) in Variable Speed Drives (VSD) Applications*. PhD thesis, KTH Royal Institute of Technology, 2011.

[10] L. Harnefors, *Control of Variable-speed Drives*. Mälardalen university, 1 ed., Sept. 2002.

[11] R. R. Moghaddam, F. Magnussen, C. Sadarangani, and H. Lendenmann, "New theoretical approach to the synchronous reluctance machine behavior and performance," in *18th International Conference on Electrical Machines*, pp. 1–6, 2008.

[12] M. Ibrahim, *Design Aspects of High Performance Synchronous Reluctance Machines with and without Permanent Magnets*. Ghent University, Dec. 2017.

[13] C. Babetto, G. Bacco, and N. Bianchi, "Analytical approach to determine the power limit of high-speed synchronous reluctance machines," Institute of Electrical and Electronics Engineers Inc., Aug. 2017.

[14] S. Sriprang, B. Nahid-Mobarakeh, N. Takorabet, S. Pierfederici, P. Kumam, N. Bizon, N. Taghavi, A. Vahedi, P. Mungporn, and P. Thounthong, "Design and control of permanent magnet assisted synchronous reluctance motor with copper loss min-

imization using mtpa," *Journal of Electrical Engineering*, vol. 71, pp. 11–19, Feb. 2020.
[15] B. A. Nasir, "An accurate iron core loss model in equivalent circuit of induction machines," *Journal of Energy*, vol. 2020, pp. 1–10, Feb. 2020.
[16] S. M. Ferdous, P. Garcia, M. A. M. Oninda, and A. Hoque, "Mtpa and field weakening control of synchronous reluctance motor," pp. 598–601, Institute of Electrical and Electronics Engineers Inc., Feb. 2017.
[17] N. Mohan, T. M. Undeland, and W. P. Robbins, *Power Electronics: Converters, Applications, and Design*. 3 ed., 2002.
[18] D. Graovac, M. Pürschel, and A. Kiep, "Mosfet power losses calculation using the data-sheet parameters," 2006.
[19] A. Huang, "Infineon optimos power mosfet datasheet explanation," 2012.
[20] S. Taghavi and P. Pillay, "A comparative study of synchronous reluctance machine performance with different pole numbers for automotive applications," pp. 3812–3818, Institute of Electrical and Electronics Engineers Inc., Feb. 2014.
[21] M. J. Karnper, A. F. Volschenk, M. J. Kamper, and A. A. F. Volschenk, "Effect of rotor dimensions and cross magnetisation on fd and l, inductances of reluctance synchronous machine with cageless flux barrier rotor," 1994.
[22] A. Vagati, M. Pastorelli, G. Franceschini, and S. C. Petrache, "Design of low-torque-ripple synchronous reluctance motors," *IEEE Transactions on Industry Applications*, vol. 34, pp. 758–765, 1998.
[23] R. R. Moghaddam, "Synchronous Reluctance Machine (SynRM) Design," Master's thesis, KTH Royal Institute of Technology, 2007.
[24] T. Matsuo and T. A. Lipo, "Rotor design optimization of synchronous reluctance machine," *IEEE Transactions on Energy Conversion*, vol. 9, pp. 359–365, 1994.
[25] T. Mohanarajah, J. Rizk, M. Nagrial, and A. Hellany, "Finite element analysis and design methodology for high-efficiency synchronous reluctance motors," *Electric Power Components and Systems*, vol. 46, pp. 1478–1493, Aug. 2018.
[26] "Torque ripple improvement for synchronous reluctance motor using an asymmetric flux barrier arrangement," *IEEE Transactions on Industry Applications*, vol. 40, pp. 1076–1082, Jul. 2004.
[27] K. Khan and O. Wallmark, "Design aspects on magnet placement in permanent-magnet assisted synchronous reluctance machines."
[28] T. A. Huynh, M. F. Hsieh, K. J. Shih, and H. F. Kuo, "An investigation into the effect of pm arrangements on pma-synrm performance," *IEEE Transactions on Industry Applications*, vol. 54, pp. 5856–5868, Nov. 2018.
[29] "Simple design approach for low torque ripple and high output torque synchronous reluctance motors," *Energies*, vol. 9, 2016.
[30] C. M. Fonseca and P. J. Fleming, "Genetic algorithms for multiobjective optimization: Formulation, discussion and generalization," 1993.
[31] E. A. Grunditz, T. Thiringer, and N. Saadat, "Acceleration, drive cycle efficiency, and cost tradeoffs for scaled electric vehicle drive system," *IEEE Transactions on Industry Applications*, vol. 56, 2017.
[32] Infineon Technologies AG, "Dynamic thermal behavior of mosfets - simulation and calculation of high power pulses," 2017.

[33] H. van der Broeck, H.-C. Skudelny, and G. Stanke, "Analysis and realization of a pulsewidth modulator based on voltage space vectors," *IEEE Transactions on Industry Applications*, vol. 24, no. 1, pp. 142–150, 1988.

[34] J. Sachs, "Which type of zsm is the best? - developer help." Available at `https://microchipdeveloper.com/mct5001:which-zsm-is-best`. Accessed: 2022-04-10.

[35] Infineon Technologies AG, "Xc164 different pwm waveforms generation for 3-phase ac induction motor with xc164cs," *Application Note, V1.0*, Jul 2006.

[36] L. Tong, G. Wu, F. W. W. Shu, and E. He, "Influence of the inverter characteristics on the harmonic losses in pwm fed traction motors," *Proceedings of the International Symposium on Electrical Insulating Materials*, vol. 2, pp. 379–381, 2005.

A

Appendix

A.1 FB5D
Ferrite magnet

FB Series

Dry molding process / La-Co type

FB5D

Demagnetization curve

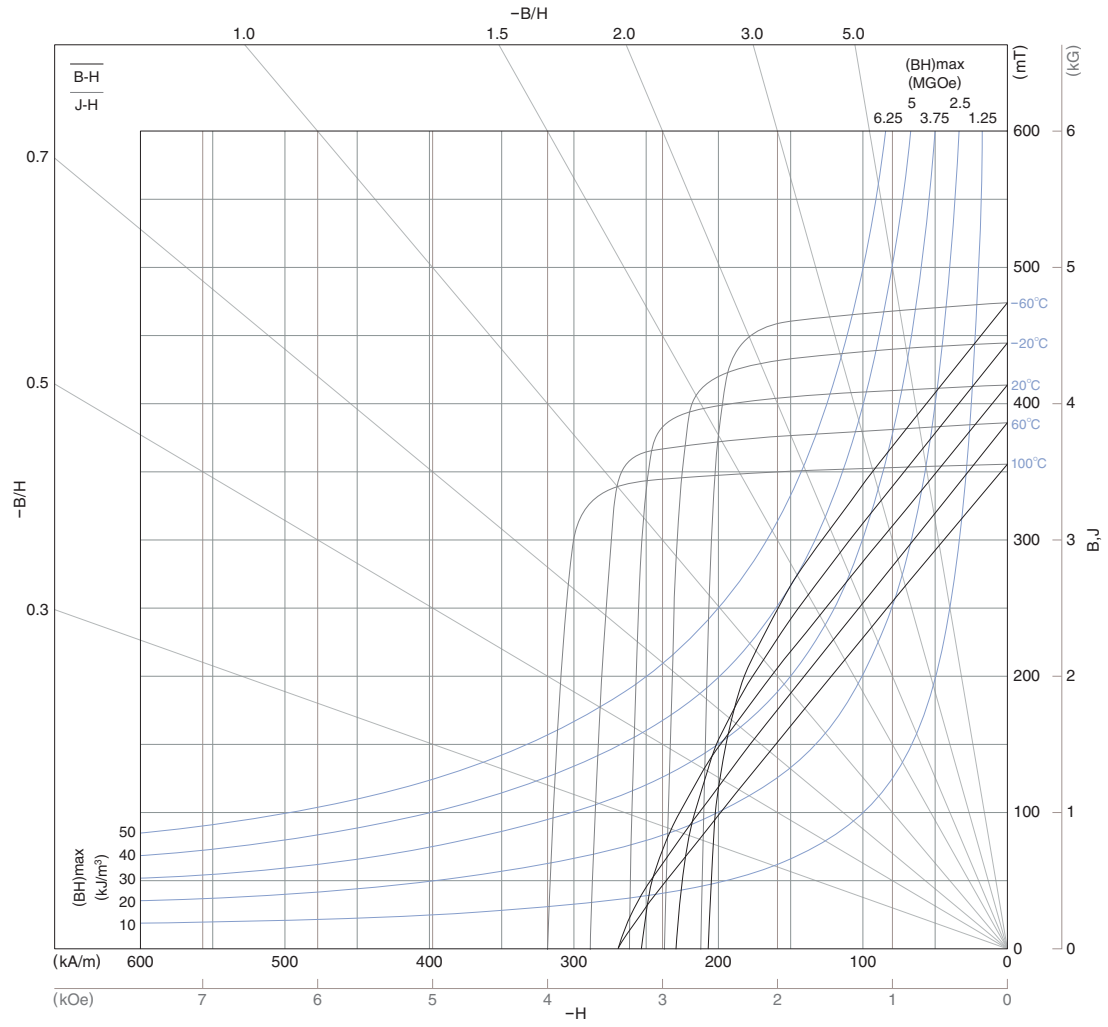

Magnetic characteristics

Material		FB5D	
Residual magnetic flux density Br	(mT)	415±10	(4.15±0.1kG)
Coercive force HcB	(kA/m)	254.6±12	(3.2±0.15kOe)
Intrinsic coercive force HcJ	(kA/m)	262.6±16	(3.3±0.2kOe)
Maximum energy product (BH)max	(kJ/m³)	32.6±1.6	(4.1±0.2MGOe)

⚠ The details can be found by referring to the appended individual delivery specifications.
All specifications are subject to change without notice.

A.2 M270-35A

Typical data for SURA® M270-35A

T	W/kg at 50 Hz	VA/kg at 50 Hz	A/m at 50 Hz	W/kg at 100 Hz	W/kg at 200 Hz	W/kg at 400 Hz	W/kg at 1000 Hz	W/kg at 2500 Hz
0,1	0,03	0,06	30,0	0,04	0,09	0,21	0,99	4,10
0,2	0,07	0,17	39,6	0,16	0,37	0,92	3,67	14,9
0,3	0,13	0,29	46,0	0,34	0,79	1,99	7,63	30,7
0,4	0,22	0,44	52,0	0,55	1,31	3,33	12,7	52,0
0,5	0,31	0,61	58,2	0,80	1,91	4,94	18,9	79,1
0,6	0,43	0,81	65,2	1,06	2,61	6,84	26,4	113
0,7	0,54	1,04	73,3	1,38	3,39	9,00	35,4	156
0,8	0,68	1,31	83,1	1,73	4,26	11,4	46,0	209
0,9	0,83	1,63	95,5	2,10	5,23	14,2	58,4	274
1,0	1,01	2,04	112	2,51	6,30	17,3	73,0	353
1,1	1,20	2,58	136	2,98	7,51	20,9	90,1	
1,2	1,42	3,38	178	3,51	8,88	24,9		
1,3	1,70	4,90	272	4,15	10,5	29,5		
1,4	2,12	9,64	596	4,97	12,5	35,4		
1,5	2,47	28,0	1700	5,92	14,9	41,8		
1,6	2,80	72,3	3880					
1,7	3,05	149	7160					
1,8	3,25	264	11600					

Loss at 1.5 T , 50 Hz, W/kg	2,47
Loss at 1.0 T , 50 Hz, W/kg	1,01
Anisotropy of loss, %	10
Magnetic polarization at 50 Hz	
H = 2500 A/m, T	1,54
H = 5000 A/m, T	1,65
H = 10000 A/m, T	1,77
Coercivity (DC), A/m	40
Relative permeability at 1.5 T	700
Resistivity, μΩcm	52
Yield strength, N/mm²	450
Tensile strength, N/mm²	565
Young's modulus, RD, N/mm²	185 000
Young's modulus, TD, N/mm²	200 000
Hardness HV5 (VPN)	215

RD represents the rolling direction
TD represents the transverse direction
Values for yield strength (0.2 % proof strength)
and tensile strength are given for the rolling direction
Values for the transverse direction are approximately 5% higher

cogent
Surahammars Bruks AB

June 2008

A.3 M330-35A

isovac®

voestalpine supplies isovac 330-50 A, an electrical steel of the highest quality. We offer you a customer-focused overall package of products, service and logistics in addition to all the advantages of our integrated metallurgical facility and Steel Service Centers.

Grade named according to conventional international standards:

Grade named according to isovac®	DIN EN 10106		IEC	JIS	GOST	ASTM	AISI	IS648	GB/T2521.1
	Material No.	Abbreviation	60404-8-4	C2552	21427.2	A677			
isovac 330-50 A	1.0809	M330-50A	M330-50A 5	50A330	-	47F190	M-27	50C330	50W330

Mechanical properties:
Tensile test according to DIN EN ISO 6892-1 and hardness according to DIN EN ISO 6507-1 (Typical values);
Test direction: Transverse

Grade named according to isovac®	Yield strength R_{eH} [MPa]	0.2 %-Yield strength $R_{p0.2}$ [MPa]	Tensile strength R_m [MPa]	Elongation A_{80} [%]	Hardness HV5 [-]
isovac 330-50 A	370	365	505	28	185

Magnetic properties:
in as-delivered condition (Typical values)
Test direction: Mean value from longitudinal and transverse measurements at 50 Hz (60 Hz), single-sheet test

Grade named according to isovac®	Specific total loss				Magnetic polarization			Relative permeability
	1.0 T P10		1.5 T P15		2500 A/m J25	5000 A/m J50	10000 A/m J100	1.5 T μ_r
	50 Hz [W/kg]	60 Hz [W/lb]	50 Hz [W/kg]	60 Hz [W/lb]	[T]	[T]	[T]	[-]
isovac 330-50 A	1.15	0.66	2.90	1.65	1.58	1.67	1.79	1300

Physical properties:
Typical values

Grade named according to isovac®	Density ρ [g/cm³]	Specific electrical resistance ρ_s [μΩcm]	Thermal conductivity λ [W/mK]
isovac 330-50 A	7.68	52.0	25

voestalpine
ONE STEP AHEAD.

isovac®

Characteristics P_s/J loss curve and characteristics J/H magnetization curve

Test direction: Mean value from longitudinal and transverse measurements at indicated frequencies, single-sheet test

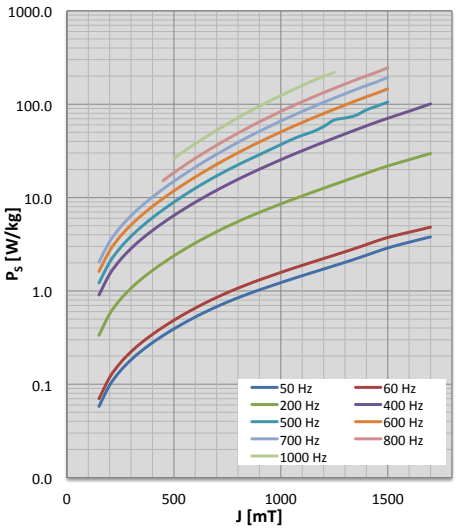

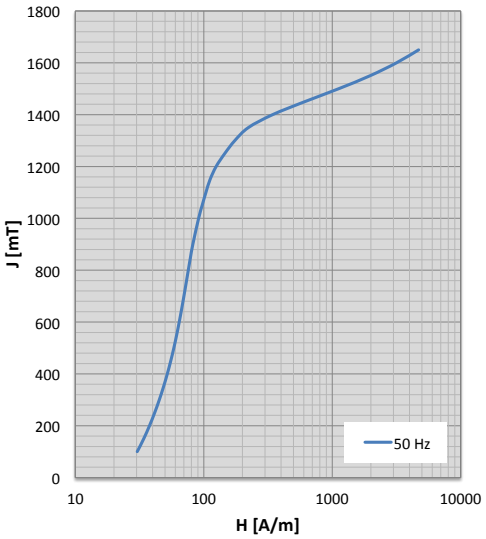

Characteristics μ_r/J permeability curve

Test direction: Mean value from longitudinal and transverse measurements at 50 Hz, single-sheet test

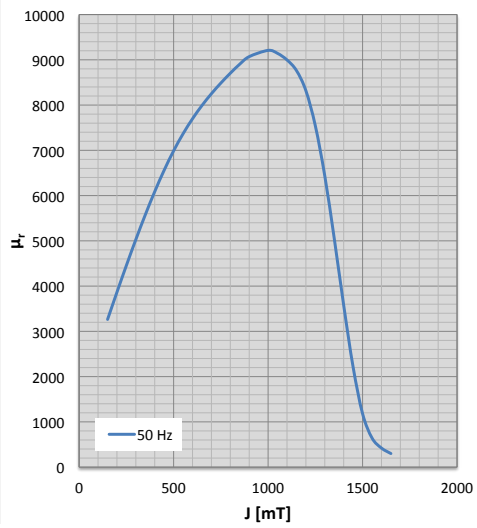

voestalpine
ONE STEP AHEAD.

isovac®

Frequency dependence of magnetic properties

Test direction: Mean value longitudinal and transverse at indicated frequencies and polarizations, single-sheet test

50 Hz				60 Hz				200 Hz			
J [mT]	H [A/m]	P_s [W/kg]	μ_r [-]	J [mT]	H [A/m]	P_s [W/kg]	μ_r [-]	J [mT]	H [A/m]	P_s [W/kg]	μ_r [-]
100	30	0.02	2650	100	31	0.02	2667	100	32	0.11	2564
150	34	0.06	3262	150	35	0.07	3219	150	37	0.34	2979
200	38	0.10	3867	200	39	0.12	3768	200	43	0.57	3389
250	41	0.14	4459	250	43	0.17	4307	250	48	0.81	3789
300	45	0.18	5031	300	47	0.22	4832	300	54	1.07	4173
350	49	0.23	5577	350	51	0.28	5339	350	59	1.35	4538
400	52	0.28	6090	400	55	0.34	5823	400	64	1.66	4877
450	55	0.33	6563	450	58	0.41	6280	450	69	2.00	5187
500	58	0.39	6991	500	61	0.48	6705	500	74	2.37	5461
550	61	0.46	7368	550	64	0.57	7093	550	79	2.79	5697
600	64	0.52	7699	600	67	0.65	7446	600	83	3.25	5895
650	67	0.60	7992	650	70	0.75	7762	650	88	3.76	6056
700	70	0.68	8252	700	73	0.85	8042	700	93	4.31	6183
750	73	0.76	8488	750	76	0.96	8285	750	97	4.90	6278
800	76	0.84	8705	800	79	1.07	8493	800	102	5.53	6343
850	79	0.93	8905	850	82	1.19	8664	850	108	6.20	6379
900	82	1.03	9071	900	85	1.31	8802	900	114	6.93	6391
1000	91	1.23	9209	1000	94	1.58	8979	1000	127	8.54	6352
1050	97	1.34	9143	1050	100	1.72	9008	1050	134	9.44	6308
1100	104	1.45	8998	1100	106	1.88	8922	1100	142	10.40	6252
1150	112	1.58	8764	1150	114	2.04	8645	1150	149	11.44	6179
1200	125	1.71	8318	1200	127	2.22	8136	1200	159	12.58	6051
1250	146	1.86	7542	1250	149	2.41	7364	1250	176	13.81	5814
1300	174	2.02	6435	1300	177	2.63	6307	1300	197	15.16	5375
1350	222	2.20	5055	1350	224	2.86	4981	1350	232	16.62	4645
1400	343	2.41	3578	1400	345	3.14	3544	1400	342	18.23	3595
1450	610	2.64	2209	1450	615	3.44	2196	1450	606	19.98	2300
1500	1122	2.88	1181	1500	1128	3.74	1175	1500	1128	21.78	1181
1550	1966	3.10	644	1550	1974	4.00	639	1550	2002	23.57	614
1600	3166	3.32	421	1600	3182	4.25	418	1600	3238	25.43	414
1650	4705	3.55	300	1650	4746	4.52	299	1650	4808	27.47	307
1700	6480	3.79	223	1700	6560	4.82	222	1700	6613	29.65	229

voestalpine
ONE STEP AHEAD.

isovac®

Frequency dependence of magnetic properties

Test direction: Mean value longitudinal and transverse at indicated frequencies and polarizations, single-sheet test

400 Hz				500 Hz				600 Hz			
J [mT]	H [A/m]	P_s [W/kg]	μ_r [-]	J [mT]	H [A/m]	P_s [W/kg]	μ_r [-]	J [mT]	H [A/m]	P_s [W/kg]	μ_r [-]
100	35	0.31	2294	100	36	0.43	2236	100	37	0.57	2149
150	42	0.91	2613	150	43	1.22	2525	150	46	1.62	2409
200	49	1.51	2926	200	51	2.04	2809	200	54	2.70	2663
250	57	2.16	3228	250	59	2.90	3080	250	62	3.85	2905
300	64	2.85	3514	300	67	3.85	3334	300	71	5.10	3130
350	71	3.60	3778	350	74	4.90	3564	350	80	6.48	3331
400	78	4.44	4014	400	83	6.08	3763	400	89	8.03	3503
450	85	5.37	4217	450	91	7.41	3927	450	98	9.79	3639
500	92	6.42	4382	500	99	8.93	4048	500	107	11.78	3734
550	99	7.59	4504	550	108	10.64	4125	550	118	14.03	3784
600	107	8.90	4587	600	117	12.57	4160	600	128	16.58	3795
650	114	10.36	4634	650	127	14.70	4161	650	139	19.45	3772
700	122	11.97	4649	700	137	17.05	4134	700	152	22.65	3724
750	131	13.74	4637	750	148	19.62	4087	750	165	26.22	3656
800	140	15.68	4601	800	159	22.41	4025	800	179	30.18	3577
850	150	17.80	4546	850	172	25.44	3955	850	194	34.54	3493
900	161	20.11	4476	900	185	28.80	3876	900	211	39.35	3404
1000	186	25.41	4305	1000	217	36.93	3687	1000	248	50.43	3222
1050	200	28.43	4212	1050	234	41.75	3580	1050	267	56.76	3131
1100	214	31.72	4115	1100	251	46.41	3494	1100	289	63.68	3039
1150	228	35.27	4014	1150	266	50.79	3434	1150	311	71.22	2948
1200	245	39.15	3912	1200	290	57.66	3298	1200	334	79.39	2860
1250	265	43.38	3808	1250	326	67.77	3058	1250	358	88.23	2776
1300	280	48.01	3694	1300	334	71.13	3095	1300	385	97.93	2686
1350	294	53.09	3512	1350	351	75.72	3140	1350	393	108.57	2667
1400	378	58.59	3033	1400	409	86.84	2739	1400	442	119.88	2521
1450	619	64.50	2122	1450	546	95.49	1988	1450	672	131.85	1903
1500	1121	70.67	1191	1500	1131	105.31	1177	1500	1121	145.94	1192
1550	1971	77.07	655								
1600	3192	84.08	419								
1650	4766	92.05	292								
1700	6591	100.74	216								

voestalpine
ONE STEP AHEAD.

isovac®

Frequency dependence of magnetic properties

Test direction: Mean value longitudinal and transverse at indicated frequencies and polarizations, single-sheet test

700 Hz				800 Hz				1000 Hz			
J [mT]	H [A/m]	P_s [W/kg]	μ_r [-]	J [mT]	H [A/m]	P_s [W/kg]	μ_r [-]	J [mT]	H [A/m]	P_s [W/kg]	μ_r [-]
100	39	0.73	2049								
150	48	2.03	2284								
200	57	3.38	2513								
250	66	4.82	2731								
300	75	6.39	2931								
350	85	8.14	3109								
400	95	10.12	3259	400	104	12.15	3087				
450	105	12.36	3374	450	114	15.19	3148	450	128	21.53	2812
500	116	14.91	3449	500	125	18.45	3191	500	142	26.28	2825
550	128	17.82	3480	550	138	22.13	3201	550	157	31.63	2812
600	140	21.13	3473	600	151	26.30	3180	600	174	37.72	2774
650	153	24.86	3436	650	166	31.03	3134	650	192	44.65	2717
700	167	29.06	3374	700	183	36.35	3068	700	212	52.53	2645
750	183	33.77	3296	750	201	42.33	2989	750	234	61.45	2564
800	199	39.01	3209	800	220	49.01	2902	800	258	71.53	2478
850	217	44.84	3119	850	241	56.44	2812	850	283	82.83	2392
900	237	51.26	3028	900	264	64.67	2723	900	311	95.35	2309
1000	280	66.02	2849	1000	313	83.65	2550	1000	371	123.97	2151
1050	303	74.43	2762	1050	339	94.49	2471	1050	402	140.14	2078
1100	327	83.62	2678	1100	366	106.30	2394	1100	436	158.22	2010
1150	353	93.67	2596	1150	395	119.14	2319	1150	471	178.42	1945
1200	380	104.59	2516	1200	425	133.05	2247	1200	507	198.86	1886
1250	408	116.40	2439	1250	456	148.05	2181	1250	542	219.19	1834
1300	438	129.22	2361	1300	490	164.22	2112	1300	585	246.96	1769
1350	457	143.37	2329	1350	517	182.06	2074				
1400	503	158.39	2215	1400	562	201.06	1983				
1450	682	173.96	1785	1450	710	220.76	1671				
1500	1115	193.58	1197	1500	1104	246.12	1187				

voestalpine
ONE STEP AHEAD.

A.4 Datasheet IPB100N12S3-05

IPB100N12S3-05

IPI100N12S3-05, IPP100N12S3-05

OptiMOS®-T Power-Transistor

AEC Qualified

RoHS

Product Summary

V_{DS}	120	V
$R_{DS(on),max}$ (SMD version)	4.8	mΩ
I_D	100	A

Features

- OptiMOS™ - power MOSFET for automotive applications
- N-channel - Enhancement mode
- Automotive AEC Q101 qualified
- MSL1 up to 260°C peak reflow
- 175°C operating temperature
- Green product (RoHS compliant)
- 100% Avalanche tested

PG-TO263-3-2 | PG-TO262-3-1 | PG-TO220-3-1

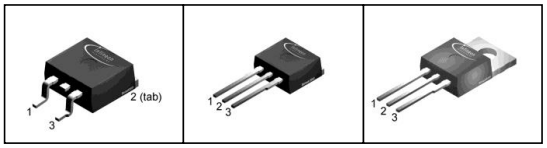

Type	Package	Marking
IPB100N12S3-05	PG-TO263-3-2	3PN1205
IPI100N12S3-05	PG-TO262-3-1	3PN1205
IPP100N12S3-05	PG-TO220-3-1	3PN1205

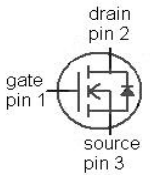

Maximum ratings, at T_j=25 °C, unless otherwise specified

Parameter	Symbol	Conditions	Value	Unit
Continuous drain current[1]	I_D	T_C=25 °C, V_{GS}=10 V	100	A
		T_C=100 °C, V_{GS}=10 V[2]	100	
Pulsed drain current[2]	$I_{D,pulse}$	T_C=25 °C	400	
Avalanche energy, single pulse[2]	E_{AS}	I_D=50A	1445	mJ
Avalanche current, single pulse	I_{AS}	-	100	A
Gate source voltage	V_{GS}	-	±20	V
Power dissipation	P_{tot}	T_C=25 °C	300	W
Operating and storage temperature	T_j, T_{stg}	-	-55 ... +175	°C

Parameter	Symbol	Conditions	Values			Unit
			min.	typ.	max.	
Thermal characteristics[2]						
Thermal resistance, junction - case	R_{thJC}	-	-	-	0.5	K/W
Thermal resistance, junction - ambient, leaded	R_{thJA}	-	-	-	62	
SMD version, device on PCB	R_{thJA}	minimal footprint	-	-	62	
		6 cm^2 cooling area[3]	-	-	40	
Electrical characteristics, at T_j=25 °C, unless otherwise specified						
Static characteristics						
Drain-source breakdown voltage	$V_{(BR)DSS}$	V_{GS}=0 V, I_D= 1 mA	120	-	-	V
Gate threshold voltage	$V_{GS(th)}$	V_{DS}=V_{GS}, I_D=240µA	2.0	3.0	4.0	
Zero gate voltage drain current	I_{DSS}	V_{DS}=120 V, V_{GS}=0 V, T_j=25 °C	-	0.01	1	µA
		V_{DS}=120 V, V_{GS}=0 V, T_j=125 °C[2]	-	1	100	
Gate-source leakage current	I_{GSS}	V_{GS}=20V, V_{DS}=0V	-	-	100	nA
Drain-source on-state resistance	$R_{DS(on)}$	V_{GS}=10V, I_D=100A	-	4.3	5.1	mΩ
		V_{GS}=10V, I_D=100A, SMD version	-	4.0	4.8	

Parameter	Symbol	Conditions	Values			Unit
			min.	typ.	max.	
Dynamic characteristics[2]						
Input capacitance	C_{iss}	V_{GS}=0V, V_{DS}=25V, f=1MHz	-	8900	11570	pF
Output capacitance	C_{oss}		-	2520	3276	
Reverse transfer capacitance	C_{rss}		-	220	330	
Turn-on delay time	$t_{d(on)}$	V_{DD}=20V, V_{GS}=10V, I_D=80A, R_G=3.5Ω	-	34	-	ns
Rise time	t_r		-	17	-	
Turn-off delay time	$t_{d(off)}$		-	60	-	
Fall time	t_f		-	20	-	
Gate Charge Characteristics[2]						
Gate to source charge	Q_{gs}	V_{DD}=96V, I_D=100A, V_{GS}=0 to 10V	-	46	61	nC
Gate to drain charge	Q_{gd}		-	34	51	
Gate charge total	Q_g		-	139	185	
Gate plateau voltage	$V_{plateau}$		-	5.5	-	V
Reverse Diode						
Diode continous forward current[2]	I_S	T_C=25°C	-	-	100	A
Diode pulse current[2]	$I_{S,pulse}$		-	-	400	
Diode forward voltage	V_{SD}	V_{GS}=0V, I_F=100A, T_j=25°C	0.6	1	1.2	V
Reverse recovery time[2]	t_{rr}	V_R=60V, I_F=50A, di_F/dt=100A/µs	-	108	-	ns
Reverse recovery charge[2]	Q_{rr}		-	380	-	nC

[1] Current is limited by bondwire; with an R_{thJC} = 0.5K/W the chip is able to carry 165A at 25°C. For detailed information see Application Note ANPS071E

[2] Defined by design. Not subject to production test.

[3] Device on 40 mm x 40 mm x 1.5 mm epoxy PCB FR4 with 6 cm^2 (one layer, 70 µm thick) copper area for drain connection. PCB is vertical in still air.

1 Power dissipation

$P_{tot} = f(T_C)$; $V_{GS} = 10$ V

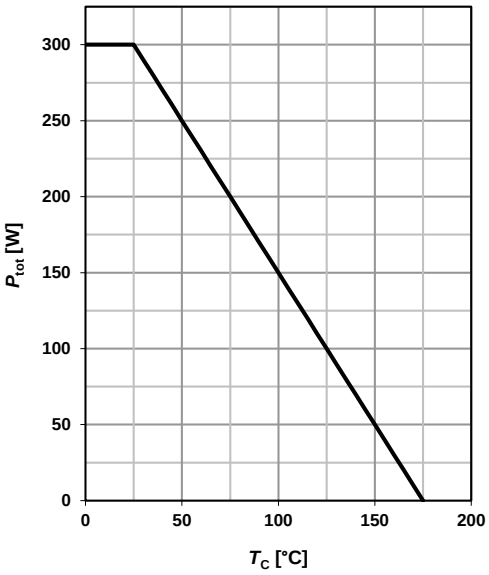

2 Drain current

$I_D = f(T_C)$; $V_{GS} = 10$ V; SMD

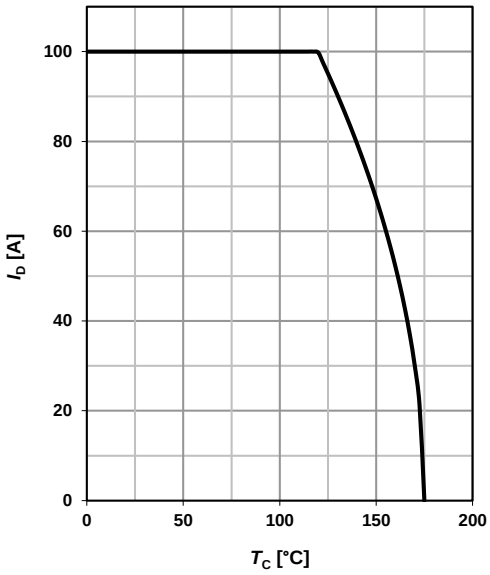

3 Safe operating area

$I_D = f(V_{DS})$; $T_C = 25$ °C; $D = 0$; SMD

parameter: t_p

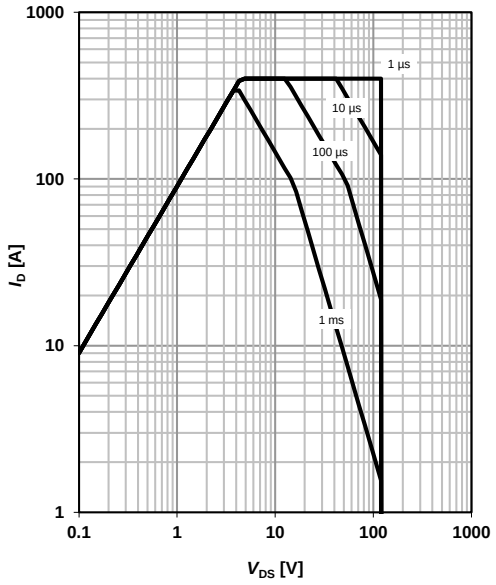

4 Max. transient thermal impedance

$Z_{thJC} = f(t_p)$

parameter: $D = t_p/T$

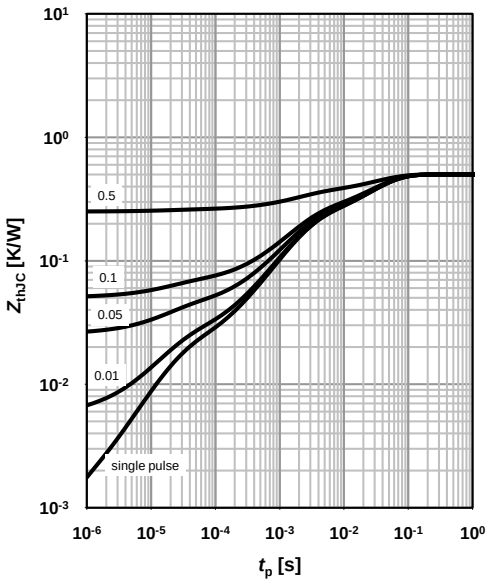

5 Typ. output characteristics

$I_D = f(V_{DS})$; $T_j = 25$ °C; SMD

parameter: V_{GS}

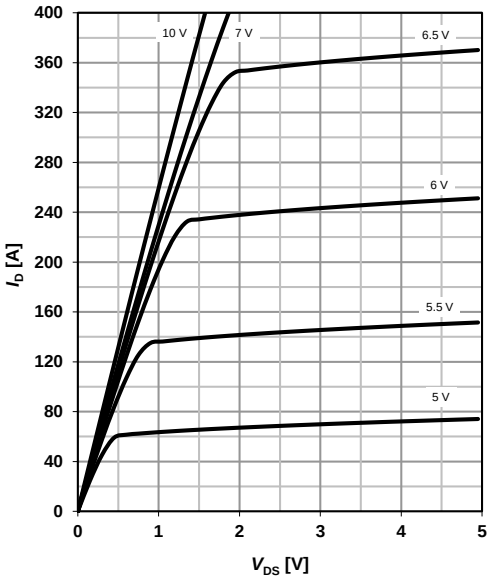

6 Typ. drain-source on-state resistance

$R_{DS(on)} = f(I_D)$; $T_j = 25$ °C; SMD

parameter: V_{GS}

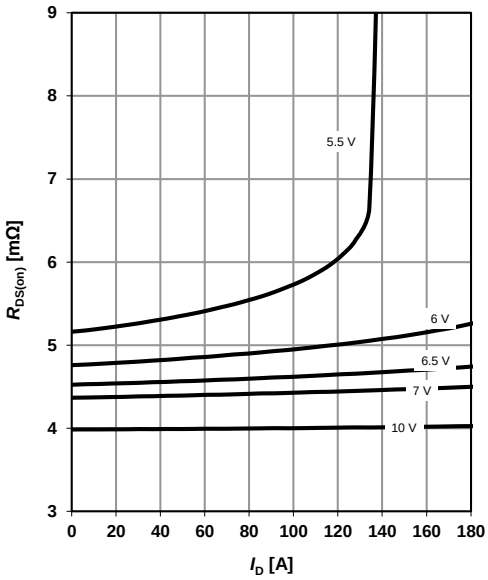

7 Typ. transfer characteristics

$I_D = f(V_{GS})$; $V_{DS} = 6$V

parameter: T_j

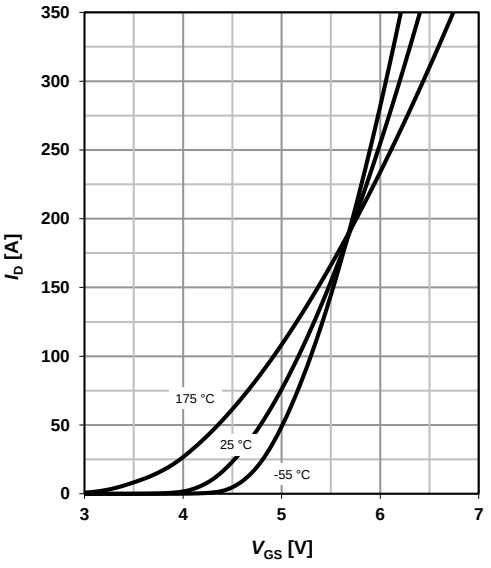

8 Typ. drain-source on-state resistance

$R_{DS(on)} = f(T_j)$; $I_D = 100$ A; $V_{GS} = 10$ V; SMD

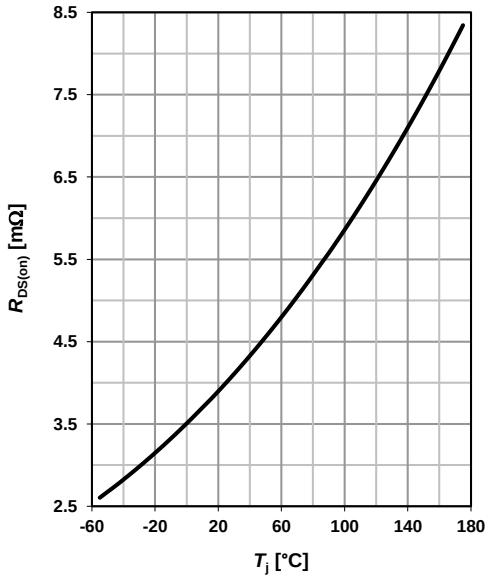

DEPARTMENT OF SOME SUBJECT OR TECHNOLOGY
CHALMERS UNIVERSITY OF TECHNOLOGY
Gothenburg, Sweden
www.chalmers.se

CHALMERS
UNIVERSITY OF TECHNOLOGY